Measurement of the Bethe-Heitler Cross Section in the TeV Regime and Search for Lorentz Invariance Violation with VERITAS

Tony Tsen-Yuan Lin

Ph.D.

Department of Physics

McGill University

Montreal, Quebec

March 2, 2020

A thesis submitted to McGill University in partial fulfillment of the requirements of the degree of Doctor of Philosophy.

ACKNOWLEDGEMENTS

I would like to thank my supervisor, Prof. Kenneth Ragan for his support, advice and feedback for this work. Thanks must also go to Prof. David Hanna, Simon Archambault, Étienne Bourbeau, Sean Griffin, David Staszak, Jonathan Tyler, Matthew Lundy, Thomas Rosin, Emma Ellingwood, Benjamin Zitzer, Stephen O'Brien, Sajan Kumar for providing stimulating discussions and help. I'd also like to thank my family, for their support and love. To Mom, Dad, Lily, I say thank you. I couldn't have done this without your support. Lastly, to Inesse, I want to thank you for your immense patience and relentless support that help me through the many anxious nights and make me believe in myself; I couldn't have come this far without you.

The computations of this work were made on the supercomputer Guillimin at McGill University, managed by Calcul Québec and Compute Canada. The operation of this supercomputer is funded by the Canada Foundation for Innovation (CFI), NanoQuébec, RMGA and the Fonds de recherche du Québec - Nature et technologies (FRQ-NT).

VERITAS is supported by grants from the U.S. Department of Energy Office of Science, the U.S. National Science Foundation and the Smithsonian Institution, and by the Natural Sciences and Engineering Research Council in Canada. I acknowledge the excellent work of the technical support staff at the Fred Lawrence Whipple Observatory and at the collaborating institutions in the construction and operation of the instrument. The VERITAS Collaboration is grateful to Trevor Weekes for his seminal contributions and leadership in the field of VHE gamma-ray astrophysics, and for his interest in the wider applications of IACTs, which made this study possible.

ABSTRACT

Violation of Lorentz invariance, commonly referred to as Lorentz Invariance Violation (LIV), near the Planck energy is a signature in many quantum gravity theories. The broken Lorentz symmetry implies a non-trivial dispersion relation for photons in vacuum and it can affect photon propagation and interaction with other particles. One of the potential effects is the modification of the pair production cross section (Bethe-Heitler cross section) of photons interacting with nuclei at high energy. As this interaction is the primary process from which extensive air showers are formed by very-high-energy gamma rays, one can directly measure the Bethe-Heitler cross section through analyzing distributions of shower maximum height of gamma-ray initiated showers. This work describes a newly developed method for reconstructing the height of shower maximum for gamma-ray initiated showers using the VERITAS telescopes and uses it to measure the Bethe-Heitler cross section up to 3 TeV. A likelihood analysis of the measurement is performed to search for a potential signal of modification of the Bethe-Heitler cross section due to LIV. Ninety-five percent CL limits are obtained on the LIV energy scale at the level of $M_{LIV,1} > 0.64 \times 10^{17} (2.4 \times 10^{17})$ GeV for a linear, and $M_{LIV,2} > 1.4 \times 10^{10} (2.8 \times 10^{10})$ GeV for a quadratic scenario, for the sub-luminal (super-luminal) scenarios, respectively.

RÉSUMÉ

La violation de l'invariance de Lorentz (VIL) autour de l'énergie de Planck est une prédiction de nombreux modèles de gravité quantique. La brisure de symétrie de Lorentz implique des relations de dispersion non triviales pour les photons dans le vide, ce qui affecte de nombreuses caractéristiques dynamiques et cinmatiques de ces derniers. Un des effets potentiels de cette brisure est la modification de la section efficace de production de paires électrons-positrons (section efficace de Bethe-Heitler) pas des photons interagissant avec des noyaux à haute énergie. Cette interaction étant le principal processus à partir duquel une gerbe atmosphérique électromagnétique est forme par des rayons gamma à très haute énergie, on peut mesurer directement la section efficace de Bethe-Heitler en analysant la distribution de la hauteur maximale des gerbes initiées par des rayons gamma. Cette thèse présente une nouvelle méthode pour reconstruire la hauteur maximale des gerbes initiées par les rayons gamma en utilisant les télescopes VERITAS. Cette méthode permettra de mesurer la section efficace de Bethe-Heitler jusqu'à 3 TeV. Une analyse de vraisemblance de la mesure est effectuée afin de rechercher un signal potentiel de modification de la section efficace de Bethe-Heitler lie à la violation de l'invariance de Lorentz. Des limites, à un niveau de confiance de95% sont obtenues sur l'échelle d'énergie du VIL à un niveau de $M_{VIL,1} > 0.64 \times 10^{17}$ (2.4×10^{17}) GeV pour un scénario linéaire et $M_{LIV,2} > 1.4 \times 10^{10}$ (2.8×10^{10}) GeV pour un scénario quadratique, pour les scénarios subluminaux et supraluminaux, respectivement.

STATEMENT OF ORIGINAL CONTRIBUTION

The author of this thesis has made several contributions to the VERITAS collaboration over the course of his PhD studies, on several scientific research topics as well as on the operation and maintenance of the instrument. The main goal of this thesis is to study the feasibility of using IACTs to measure the Bethe-Heitler cross section with gamma-ray initiated showers and hence utilizing the result to constrain the LIV effect. The cross section measurement and LIV searches outlined in this thesis were developed and performed solely by the author. The author has studied the method of correction for the height of shower maximum measurement; the necessary Monte-Carlo simulation necessary for calibrating the method is also produced by the author. The early stages of the data analysis are based on standard VERITAS analysis packages; the author made the necessary modifications to the standard analysis code to reconstruct the height of shower maximum accurately. The subsequent analysis of extracting cross sections and LIV energy scale limits is conducted through a collection of scripts that has been developed by the author. He also compiled the list of runs to be used for the analysis. Chapter 6 and 7 detail the author's contributions.

Apart from the work related to the main topic of this thesis, the author also developed a new Python-based software for the conversion of the VERITAS proprietary data format into the upcoming open data format *DL3*. The details of this data format and its benefits are detailed in Chapter 4. This work resulted in a joint paper between the VERITAS, H.E.S.S. and MAGIC collaborations [1].

Other than the work described in this thesis, the author also participated in a joint effort of the VERITAS, H.E.S.S. and MAGIC collaborations to combine multiple sources to perform time-of-flight searches. This work resulted in a presentation by one of the collaborators at the 2016 International Cosmic Ray

Conference (ICRC) in Busan, Korea and has been published in the proceedings [2]. A publication on this work is still in progress.

During his PhD, he also performed an updated analysis on the pulsed emission of the Crab Pulsar, for which a VERITAS internal memo was released for the collaboration.

The author contributed to the operation of VERITAS through many observing shifts at the VERITAS site. In 2019, the author spent three months at the VERITAS site working as part of the day crew to facilitate the day-to-day maintenance of the instrument. During this three month period, he also participated in observing shifts where he was the lead observer in charge of the nightly operation (the shift czar) and responsible for the observing schedule. Throughout his PhD studies, he was also responsible for the maintenance of the database access webpage *Loggen*, which provides a graphical interface to the database to facilitate collaboration members to search for data runs.

TABLE OF CONTENTS

LIST OF TABLES

LIST OF FIGURES

1 Introduction

Our current understanding of physics is based on two pieces: "Quantum Mechanics" and "General Relativity". While very successful in describing the physics in their respective regimes, it is difficult to integrate the two theories under the same framework. Either of the theories fails to describe systems where both quantum effects and gravity are important. This is commonly known as the Quantum Gravity (QG) problem. Experimentally, producing such a system is beyond the capability of current instruments. So, although there are significant efforts on the theoretical front, experimentally verifying or constraining quantum gravity theories remains difficult.

An alternative is to utilize high-energy particles produced from astrophysical sources to search for minute effects that could be a result of a quantum gravity theory. One such effect is the potential violation of Lorentz invariance (Lorentz Invariance Violation (LIV)). A broken Lorentz invariance can affect both the kinematics and dynamics of particle interaction and propagations. Instruments detecting gamma-rays with energies above 100 GeV (called "very-high energy", or VHE) are ideal for such searches. VHE gamma-ray astronomy is a relatively young field of astronomy that is rapidly developing since the first detection of multi-TeV gamma-rays from the Crab nebula in 1989 [3].

This thesis describes a search for LIV through its effect on the Bethe-Heitler cross section [4]. Using the VERITAS (Very Energetic Radiation Imaging Telescope Array System) telescopes, we aim to measure the interaction cross section of VHE gamma-rays with the atmosphere and derive limits on the energy scale of potential LIV effects.

1.1 Thesis Overview

We will start with a brief description of the field of VHE gamma-ray astrophysics, describing different production mechanisms in Chapter 2. The VERITAS experiment will be described in chapter three with a focus on the hardware and experimental technique. An overview of the analysis technique for VERITAS data will follow in chapter four.

In chapter five, we will then focus on tongravity phenomenology, in particular on LIV and different searches that can be performed using VHE gamma-ray telescopes. An overview of different constraints on the quantum gravity energy scale will also be given.

The analysis method that is developed to measure the Bethe-Heitler cross section will be described in chapter six. In this chapter, we will also give a detailed description of a new method to reconstruct the height of shower maximum of gamma-ray initiated air showers as it is the main component of the cross section measurement. The result from using observing data on the Crab nebula will also be presented in this chapter. Finally, a limit on the energy scale for quantum gravity will be extracted from the cross section measurements and discussed in chapter seven.

2

Very-High-Energy Gamma-Ray Astronomy

The foundation of astronomy is the detection of electromagnetic waves originating from sources beyond Earth. The electromagnetic spectrum spans a wide range, from radio waves at the low energy end to gamma-rays. Traditional astronomy, limited by detection technology, was mostly concerned with phenomena that emit electromagnetic waves at radio, or optical wavelengths. The field of gamma-ray astronomy is a relatively new field due to the constraint of atmospheric absorption. High energy photons mostly cannot be detected directly on the ground. However, the discovery of cosmic rays (charged particles of high energy coming from astrophysical sources) prompted the question of where and what can be producing these high energy particles. The nature of charged particles make them a poor choice for studying the astronomy of these sources as the inter-stellar (or inter-galactic) magnetic fields redirect these particles. Hence, the detection of gamma rays is a powerful alternative for studying the universe at TeV energy scale.

Gamma rays are electromagnetic radiation that belongs to the part of the spectrum above 0.1 MeV. The term was originally used to describe electromagnetic radiation originating from nuclear reactions; however, gamma rays cover a very large range of energies and can be produced and detected through various different

mechanisms. To better describe this energy band, it is divided into smaller sub-bands which are presented in Table 2–1.

Low Energy (LE)	100 keV to 10 MeV
Medium Energy (ME)	10 MeV to 30 MeV
High Energy (HE)	30 MeV to 100 GeV
Very High Energy (VHE)	100 GeV to 100 TeV
Ultra High Energy (UHE)	100 TeV to 100 PeV
Extremely High Energy (EHE)	Above 100 PeV

Table 2–1: Gamma-ray energy bands.

Due to the difficulty of producing VHE gamma-rays, gamma-ray emission is the signature of extreme physical conditions such as strong magnetic and electric fields or relativistic jets of charged particles. The astrophysical sources of gamma rays include various types of active galactic nuclei (AGN), pulsar wind nebula (PWN), gobular clusters, and pulsars[5].

As mentioned earlier, detection of gamma rays requires different instruments from traditional optical or radio telescopes. The advances of satellite technology starting in the 1960s opened up the window to gamma rays. Unlike their lower energy counterparts, gamma rays cannot be manipulated with mirrors or lenses through reflection or refraction. So, techniques and detector technologies imported from high-energy particle physics are applied. At energies ranging from several MeV to 100 GeV, gamma rays can be detected directly by satellite-based instruments such as the Large Area Telescope (LAT) onboard the Fermi Gamma-Ray Telescope [6]. However, the energy spectrum of gamma ray sources generally follows a power law function, which means a significant reduction in flux for increasing energies statistics due to their limited size. Special techniques are needed to explore the sky in the VHE band. One alternative is the Imaging Air Cherenkov Telescope (IACT) , pioneered by the Whipple collaboration [3]; it is the technique of detection of gamma rays by collecting Cherenkov light emitted from extensive

air showers generated by high-energy photons in the atmosphere. The direction of the primary gamma rays can be reconstructed and the technique also allows rejection of hadronic showers initiated by cosmic rays through imaging the extensive air shower. This technique makes a collection area of $\sim 10^5 \mathrm{m}^2$ possible, a significant improvement over satellite-based instruments. More than 100 VHE sources have been detected [7] since the first discovery of VHE emission from the Crab Nebula with the Whipple 10 meter telescope in 1989.

In this chapter, we will review the particle physics interactions that are involved in the production of gamma rays from astrophysical sources. Also, we will review the detection method of gamma rays at VHE energies and the currently operating telescopes that implement these techniques.

2.1 Gamma ray Production Mechanism

One question that is worth pondering is: "How can the Universe produce VHE gamma rays". The main mechanisms of gamma-ray production come from charged particles accelerated to relativistic speeds. There are two parts to this discussion; the first is how to accelerate the charged particles up to this regime, the second part is how do charged particles produce gamma rays. We will briefly discuss the mechanisms that accelerate the charged particles and then the production of gamma rays.

2.1.1 Fermi Acceleration

There are two main types of charged particle acceleration in astrophysical sources. A straightforward way is through the presence of strong electric fields (for example in the magnetosphere of pulsars). The second type is called Fermi acceleration.

Fermi acceleration is the mechanism of accelerating charged particles when they are repeatedly reflected by magnetic mirrors. Fermi acceleration comes in two types: first and second order accelerations. The second-order process was first

proposed by Enrico Fermi in 1949 [8]. He postulated that charged particles could be reflected by magnetized gas clouds in the interstellar medium stochastically and gain energy. The average energy gain per reflection is proportional to $(\frac{v}{c})^2$ where v is the gas cloud's velocity and c is the speed of light in vacuum [9].

First-order acceleration is a more efficient process. In this case, instead of stochastically reflecting off gas clouds, the charged particles are repeatedly reflected by magnetic fields around a shock front. After each crossing of the shock front, the particles gain energy proportional to $(\frac{v}{c})$ where v is the velocity of the shock front and c is the speed of light in vacuum. This acceleration mechanism results in a power-law spectrum with a power-law index close to two (the exact solution for a non-relativistic adiabatic shock in monoatomic gas) [9]. Depending on the compression factors of the shock the power-law index could deviate from 2. Shocks are prevalent in astrophysical sources such as supernova remnants or AGN; this makes first-order Fermi acceleration a very good candidate for explaining the production mechanism of ultra-relativistic particles.

While first-order Fermi acceleration is successful at describing the acceleration process, it poses a problem called the "injection problem" [10]. For the acceleration process described above to start, particles need to posses initial energy above the thermal energy to be able to cross the shock front. The processes that accelerate particles up to these initial energies remain an issue at the time of writing.

2.1.2 Gamma Ray Production from Charged Particles

Now that we have a mechanism to accelerate charged particles, the next question is how do these charged particles produce gamma rays. We can roughly classify the gamma ray production based on the type of charged particles involved. The process is leptonic if the particles are mainly electrons and positrons. If protons are the main gamma ray producing particles, it is hadronic.

Inverse Compton Scattering

The main leptonic process for the production of VHE gamma rays is Inverse Compton Scattering [11]. Physically it is the same as Compton scattering (Figure 2–1), where a photon elastically scatters with a charged particle; the descriptor "inverse" is used to emphasize the particular regime of interest in high energy photon production. A low energy photon scattering with a relativistic electron/positron (although the same process can happen for protons as well, the cross-section of this process is proportional to $\frac{1}{\mathrm{m}^2}$ [12]. So, proton inverse Compton scattering is much less important than electron Compton scattering) can be boosted to higher energy. For a low energy photon of energy E_γ scattering with an electron with Lorentz factor γ_e, the final energy of the photon typically becomes:

$$E'_\gamma \sim \gamma_e^2 E_\gamma \tag{2.1}$$

In the Thompson regime (the classical regime, when the wavelength of the photon is much larger than the electron's Compton wavelength in the centre of mass frame, i.e. $E_{\gamma,cm} << m_e c^2$), the resulting spectrum of the scattered photons follows a power-law spectrum of index $(1+\alpha)/2$ if the electron population follows a power-law spectrum with index α [5]. In the high energy regime ($E_{\gamma,cm} >> m_e c^2$), the cross section of the interaction is suppressed on the order of $\frac{1}{E_\gamma}$ as it follows the Klein-Nishina formula [12]. So, in general, the gamma-ray spectrum due to inverse Compton scattering exhibits a cut-off.

For this process to work, a low-energy photon field around the accelerated electrons is needed. Low-energy photons can come from thermal emission from stars, the Cosmic Microwave Background (CMB) or synchrotron emission from the relativistic electrons in magnetic fields. Combining these low-energy photon sources and a population of relativistic electrons accelerated through the Fermi acceleration process makes this a common process for VHE emission.

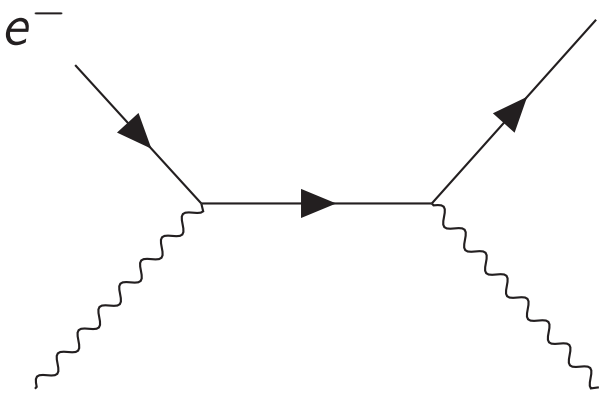

Figure 2–1: Feynman-diagram of Compton scattering.

Synchrotron Radiation

Another important process when considering gamma-ray production is synchrotron radiation. Synchrotron radiation is produced when charged particles are moving in a magnetic field. Under the influence of the magnetic field the charged particles circulate around the field lines and produce broad band emission. The energy at the peak of the spectrum is:

$$E = \frac{\hbar 3\gamma^2 e}{2m_e} B \sin\theta \tag{2.2}$$

where γ is the Lorentz factor of the electron, m_e is the rest mass of electron, B is the strength of the magnetic field and θ is the angle between the direction of the electron and the magnetic field line.

While it is possible to obtain gamma rays from synchrotron radiation directly, the energy of these gamma rays normally cannot reach the VHE range as the presence of the magnetic field prevents the electron population to reach the energy required to radiate VHE gamma rays. In the context of VHE gamma ray astronomy, the main role it plays is supplying the seed photons for the inverse Compton scattering processes. When the same electron population produces both the synchrotron radiation and VHE gamma rays, the process is referred to as the Synchrotron Self-Compton (SSC) mechanism.

Neutral Pion Decay

So far we have discussed leptonic processes for gamma-ray production. Hadronic interactions can also produce gamma rays. The main channel of hadronic gamma ray production is through neutral pion π^0 decay:

$$\pi^0 \rightarrow \gamma + \gamma \tag{2.3}$$

Pions are common products of proton-nucleus reactions. There are three types of pions π^0, π^+ and π^- and they are unstable with a short lifetime (8.52×10^{-17} s for neutral pions and 2.6×10^{-8} s for charged pions [13]). The main decay channel of the charged pions is muons plus neutrinos (99.98% of the time [13]). The main decay channel for neutral pions is the above-mentioned photon production (98.8% of the time [13]).

An interesting result of this process is that the hadronic gamma ray production is always accompanied by neutrino production. So, an observation of neutrinos from gamma ray sources by a neutrino observatory (such as Ice Cube) would be a strong indication of a hadronic emission mechanism at play.

2.2 Detection of VHE gamma rays

The atmosphere of Earth is opaque to gamma rays, so how can one detect gamma rays? There are two options. The first obvious solution is to launch detectors in space so we can detect them before entering the atmosphere. The second method is to detect the products of the interaction with the atmosphere. In this section, we will describe the particle interactions involved in the detection of gamma rays, particularly the process involved in ground based detection of VHE gamma rays.

2.2.1 Pair Production

At energies larger than 10 MeV [14], the dominant process for photons interacting with the atmosphere is pair production of electron and positron in the

presence of the Coulomb field of a nucleus (Bethe-Heitler process, see Figure 2–2). When a photon has an energy larger than ~ 1 MeV (i.e. $2 \times m_e c^2$), this process is allowed. However, the photon cannot directly decay into a positron and electron; to be able to conserve momentum, a nucleus needs to be present.

The cross section of this process was derived by Bethe and Heitler [4]:

$$\sigma = \frac{28 Z^2 \alpha^3}{9 m_e^2} \left(\log(\frac{183}{Z^{1/3}}) - \frac{1}{42} \right) \tag{2.4}$$

where Z is the atomic number of the nucleus and α is the fine structure constant. In air this yields $\sigma \approx 0.51$ b, which means a mean free path[1] of $\sim 47 \mathrm{g/cm}^2$. For a more comprehensive review of the pair-production process see Tsai [15].

This interaction plays an important role in both satellite and ground-based gamma ray detection. For instruments like the LAT onboard the Fermi Gamma-Ray Space Telescope [16] (Figure 2–3), the main component of the detector is made up of layers of silicon tracker and tungsten foils. The gamma rays interact with the tungsten foils and produce electron and positron pairs. The silicon tracker then can track the trajectory of the produced electron/positron pair. The energy and direction of the original gamma ray is then inferred from the energy and direction of the electron/positron pairs. Pair production is also an essential component of the development of particle showers in the atmosphere, which will be discussed in the next section

2.2.2 Extensive Air Showers

When a high-energy gamma ray reaches the upper atmosphere of Earth, the photon interacts with air molecules in the upper atmosphere. As we discussed

[1] To remove the dependency of mean free path on the density of the target material, we use the unit $\mathrm{g/cm}^2$ which can be thought of as $\rho \times \lambda$, where ρ is the density of the target material in the unit of $\mathrm{g/cm}^3$ and λ is the mean free path in the unit of cm.

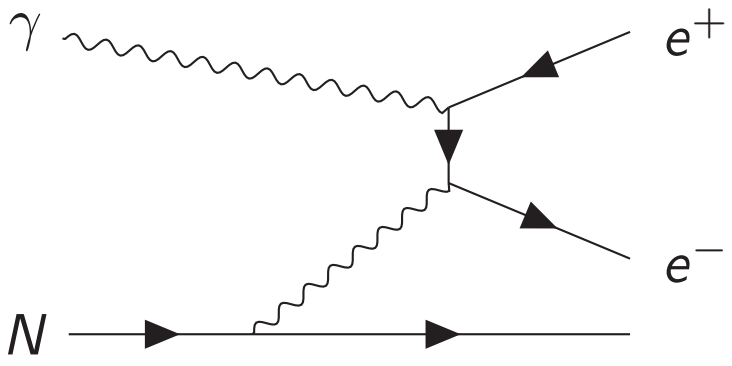

Figure 2–2: Feynman-diagram of the Bethe-Heitler process.

earlier, VHE gamma rays mainly interact with the atmosphere through pair-production. After the primary gamma ray interacts, the secondary electrons and positrons can produce gamma rays via "Bremsstrahlung" ("braking radiation" in German). Bremsstrahlung is the process where electrons/positrons accelerated in the electric field of the nucleus emit photons (Figure 2–4). In effect, electrons slow down through this process and convert their kinetic energy into photons. The secondary photons can then go through pair-production again.

This cycle repeats and the number of particles (e^+, e^-, γ) grows exponentially. A cascade of electrons and positrons is then formed (Figure 2–5). Due to the high energy of the primary gamma ray, the electron-positron pairs and subsequent bremsstrahlung gamma-rays are beamed strongly in the forward direction. The resultant particle cascade has a relatively small lateral distribution ($\sim$ 30 m) and an extended longitudinal distribution ($\sim$ 10 km).

Each generation of electron/positrons/photons has lower energy than its predecessor through dividing the energy among a larger number of particles and energy loss due to ionization. Because the energy loss of electrons through bremsstrahlung is roughly proportional to the energy of the electron (the energy of the photon produced is roughly $E/3$ [9]), there exists a point at which the energy of the electrons is reduced to the extent that ionization becomes the dominant

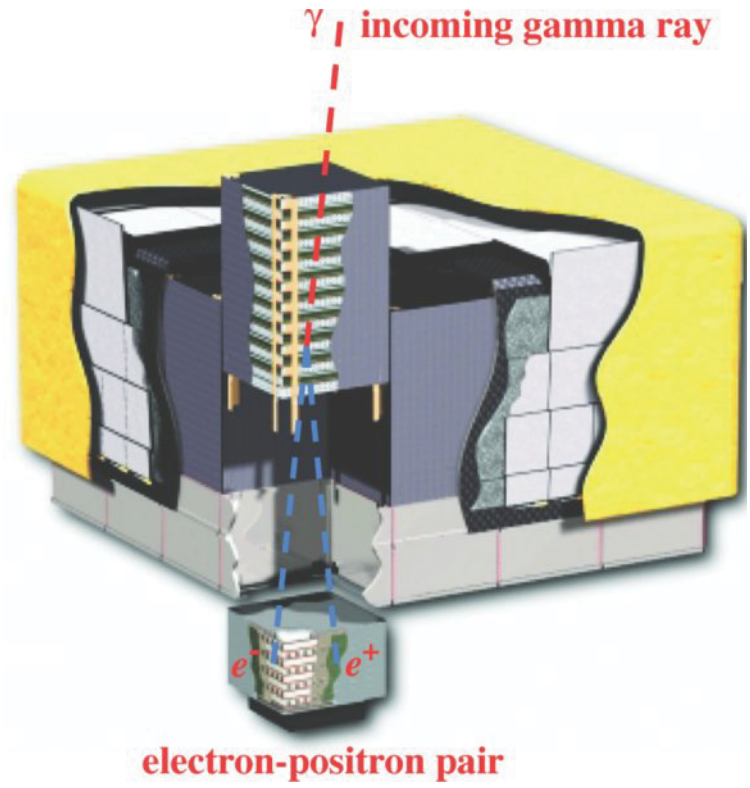

Figure 2–3: Schematic drawing of the Large Area Telescope. The telescope has a size of 1.8m × 1.8m × 0.72m. Image Credit: Figure 1 of [16].

process for energy loss, and the development of the cascade halts. The energy of the shower then dissipates into the atmosphere. This is also where the cascade has the largest number of particles (named shower maximum). For a gamma-ray primary of energy between 100 GeV and 1 TeV, the shower maximum occurs $\sim$ 10 km [13] above sea level.

Although air shower development is a complex process, Heitler [17] found that many properties of an electro-magnetic cascade can be understood through a simple model. Heitler's model has electrons, positrons and photons undergoing repeated two body splitting through either bremststrahlung or pair production after traveling a fixed distance related to the radiation length. As mentioned earlier, this process stops when the energy of particles is below a critical energy.

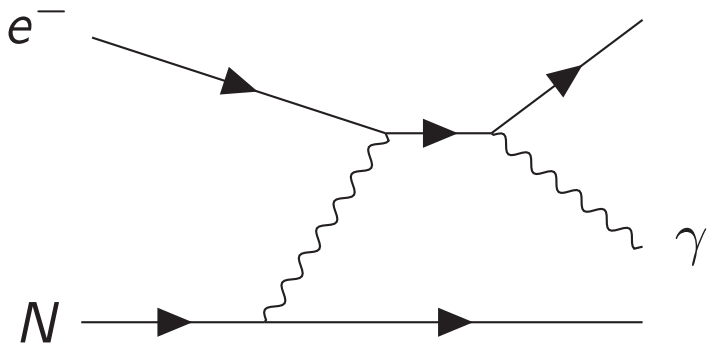

Figure 2–4: Feynman-diagram of the Bremmsstrahlung process.

Using this simple picture, one can obtain some key features of the air shower. The first feature that comes out of this simple model is that the energy of the primary particle is proportional to the number of particles at shower max. Another feature is that the length of the shower is proportional to the logarithm of the energy of the primary particle (the proportional constant here is called the elongation rate [14]).

The ground-based detection methods of gamma rays are all based on detection of the extensive air showers, either by directly detecting these charged particles (for example the Milagro and HAWC experiments; see Section 2.3.2) or detecting the Cherenkov radiation emitted by the charged particles.

2.2.3 Cherenkov Radiation

Cherenkov radiation is the electromagnetic radiation emitted by dielectric materials when charged particles are traveling through it with speeds faster than the local speed of light. The Cherenkov effect occurs when the speed of a charged particle $v > \frac{c}{n}$, where n is the refractive index of the dielectric material; it can be thought of as the electromagnetic analog of a super-sonic jet breaking the sonic barrier and generating a shock wave front. In Figure 2–6, the successive wavelets of the electric field from a moving charged particle are drawn. The wavelet travels outwards at the velocity of $\frac{c}{n}$. When $v < \frac{c}{n}$, the entire space is under the influence

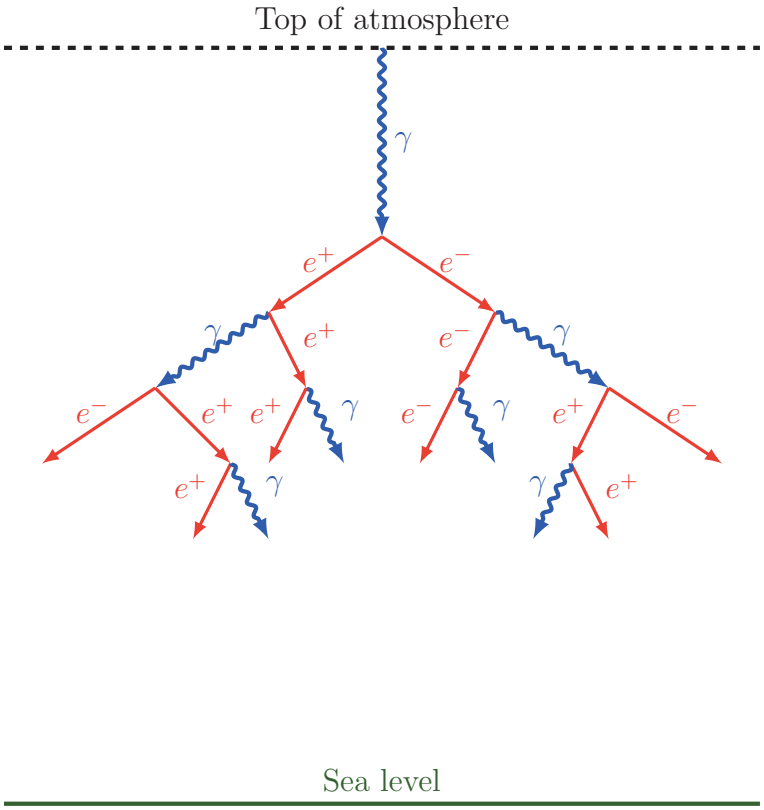

Figure 2–5: Cartoon of an extensive air shower generated from a gamma-ray primary. The angles and path length of particles are not drawn to scale.

of the electric field of the charged particle at all times. On the other hand, when $v > \frac{c}{n}$, a shock front appears. The wavelets interfere constructively at the shock front and Cherenkov photons are generated.

From this simplified image, one can see that the shock front travels at an angle $\theta_c = \cos^{-1}\frac{c}{vn} = \cos^{-1}\frac{1}{\beta n}$, where $\beta = \frac{v}{c}$. The radiation is emitted in a cone with the angle θ_c from the propagation direction of the charged particle. A more rigorous derivation by solving Maxwell's equation yields the same result and gives the number of photons (N) emitted per unit length traveled (x) and per unit wavelength (λ) as follows:

$$\frac{\partial N}{\partial x \partial \lambda} = \frac{2\pi\alpha z^2}{\lambda^2}\left(1 - \frac{1}{\beta^2 n(\lambda)^2}\right) \tag{2.5}$$

The inverse dependency on wavelength implies that the resulting radiation is mostly low-wavelength photons.

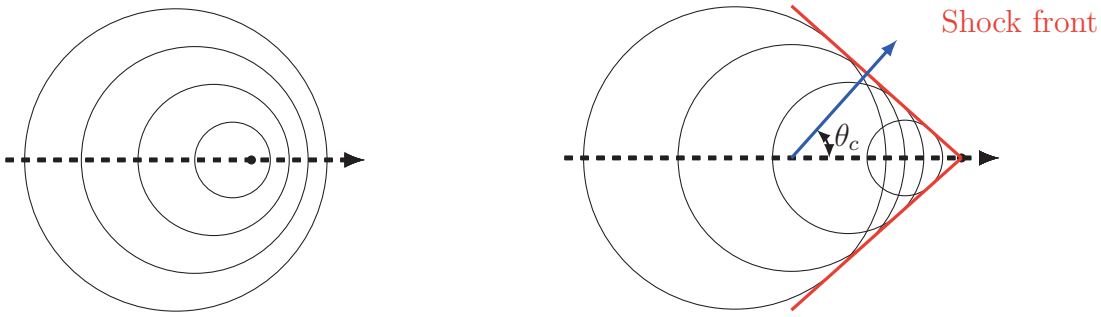

(a) $\beta < 1$ (b) $\beta > 1$

Figure 2–6: Mechanism of Cherenkov radiation. (Left) The electric field travels faster than the charged particle. (Right) A shock front appears because the charged particle is traveling faster than the electric field.

The electrons and positrons in an air shower are moving relativistically ($\beta \rightarrow 1$). This leads to Cherenkov radiation from extensive air showers. The refractive index of air is dependent on the wavelength of the emitted photons. The condition for a charged particle to emit Cherenkov radiation $v > \frac{c}{n}$ can only be satisfied if the Cherenkov photons have energies in the regime of UV or lower. Combining with atmospheric attenuation, when the photons reach the observatory, the Cherenkov radiation has a spectrum peaked in the near-UV regime at a wavelength of ~ 330 nm [18]. As Cherenkov light is generated in a cone with angle θ_c, the Cherenkov light from an air shower is concentrated in a pool on the ground with radius ~ 120 m[18] (generally referred to as the "light pool").

2.2.4 The Imaging Atmospheric Cherenkov Technique

Cherenkov-light-emitting air showers are essentially a moving "blob" of light, so when applying focusing optics and cameras to capture the Cherenkov photons reaching the ground, an image of the air shower will be recorded (Figure 2–7). Such telescopes are commonly referred to as Imaging Air Cherenkov Telescope (IACT). The morphology of the image depends on the spatial extension of the

shower and the position of the shower relative to the telescope. A gamma-ray initiated shower, with narrower lateral distribution, leaves an elongated image on the camera. The direction of the elongation can be used to reconstruct the incoming direction of the primary gamma rays.

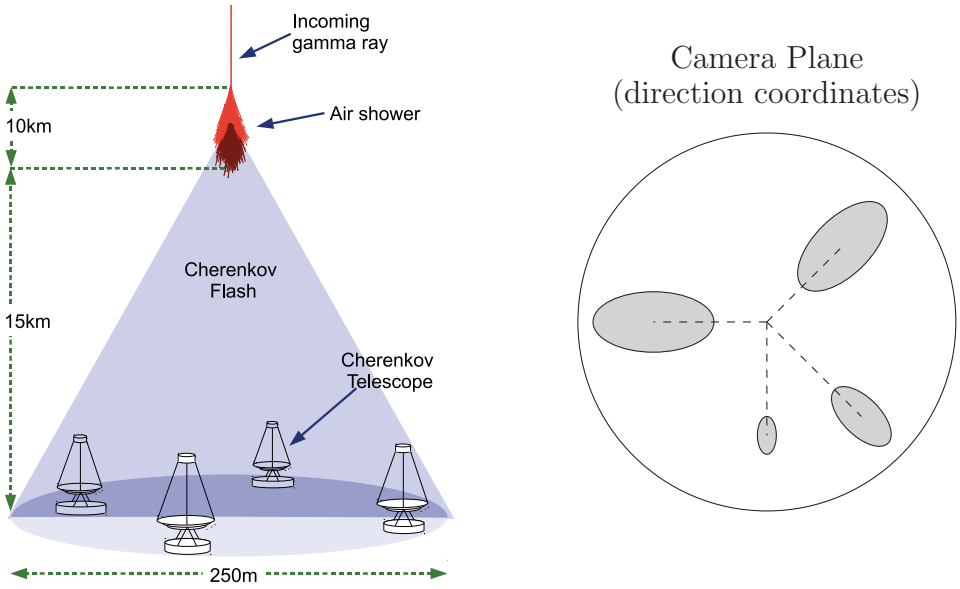

Figure 2–7: (Left) Illustration of a gamma-ray induced air shower imaged by an array of telescopes. Image Credit: [18]. (Right) Images of air showers on the camera plane resemble ellipses. The intersection of the major axes of the ellipses indicates the incoming direction of the primary gamma ray.

To increase the collection area as well as to enhance the resolution of directional reconstruction, more than one telescope operates in conjunction in modern IACT systems. Having more than one telescope allows a stereoscopic view of a shower. Combining images from several telescopes results in a better directional reconstruction of the primary gamma ray. Also, knowing the relative position of the telescopes, the axis of the air shower intersecting the ground (shower core) can be reconstructed. This information is an important parameter for reconstructing the energy of primary particles.

The bulk of air showers are not generated by gamma-rays; high-energy cosmic rays generate air showers as well and are $\sim 10^4$ times more numerous. Cosmic rays are composed mainly of protons and heavy nuclei; a cosmic-ray-initiated shower has a hadronic component that is absent in gamma-ray showers. The dominant process for the primary proton is interaction with the nucleus of an atmospheric molecule, producing high energy π mesons (π^0,π^+,π^-). A hadronic cascade is thus produced from the successive interactions of the secondary particles. The produced neutral pions rapidly decay into gamma rays and produce gamma-ray sub-showers. The charged pions continue to proceed and interact until they decay and produce muons. The involvement of hadronic processes leads to particles with much larger transverse momentum compared to gamma-ray initiated showers which leads to a larger lateral distribution. This feature provides a powerful parameter for discrimination from gamma-ray showers. The image of a gamma-ray-initiated shower is narrower on the camera plane compared to a hadronic shower (Figure 2–8).

A more detailed description of the analysis method will be presented in Chapter 4

2.3 Ground Based Gamma Ray Observatories

Since the first detection of the Crab Nebula by the Whipple observatory [19], there has been significant development in ground based gamma-ray instruments. In this section, we will describe some currently operating ground based gamma ray observatories and briefly discuss the next generation VHE gamma-ray instrument, the Cherenkov Telescope Array (CTA).

2.3.1 IACT

H.E.S.S

The High Energy Stereoscopic System (H.E.S.S) [20] telescope consists of five IACTs located in Namibia on the Khomas Highland near Gamsberg mountain.

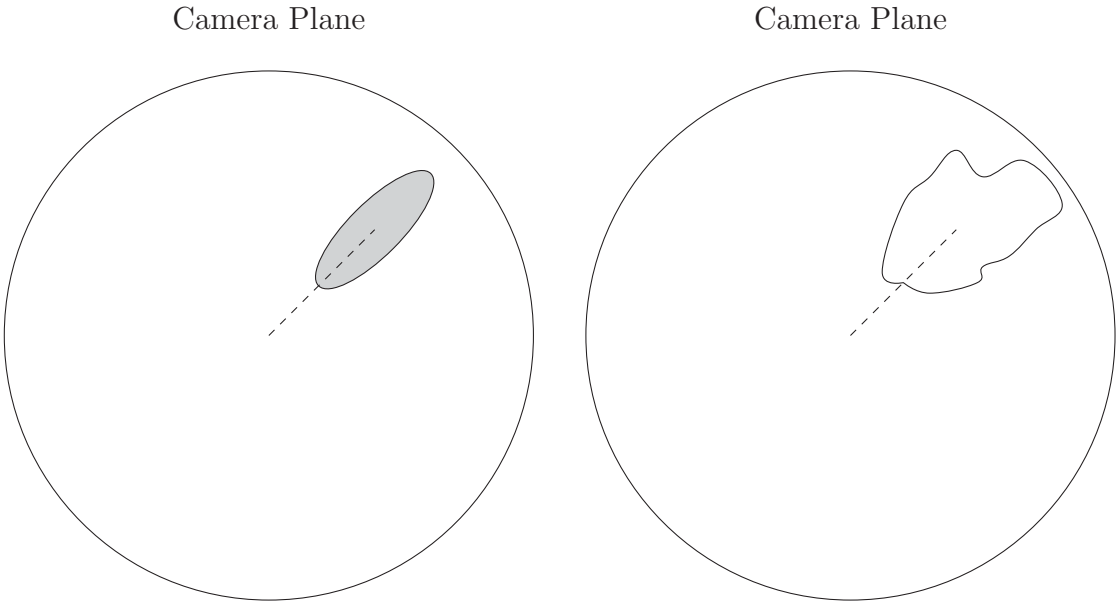

(a) Gamma-ray shower image (b) Proton shower image

Figure 2–8: Cartoon of images of a gamma-ray-initiated (left) and a proton-initiated (right) air shower.

The first four 12 m telescopes became operational in December 2003. These four telescopes have a field of view of 5° and are arranged in a square configuration. This is now called H.E.S.S. Phase I. Since July 2012, a fifth 28 m diameter telescope is in operation; it is located in the middle of the square configuration targeting a lower energy threshold than the Phase I telescopes. This is now called H.E.S.S. Phase II. Figure 2–9 shows the H.E.S.S. Phase II array.

MAGIC

The Major Atmospheric Gamma Imaging Cherenkov Telescopes (MAGIC) [21] is a system of two 17 meter diameter telescopes, located on the Canary island of La Palma, Spain, at the Toque de Los Muchachos Observatory at an altitude of 2200 m above sea level. The first MAGIC telescope saw first light in 2004 and worked in stand-alone mode untill 2009. The second telescope entered operation in 2009 and the two telescopes have operated jointly since then. In summer 2011 and 2012, the two telescopes underwent a major upgrade of the readout system

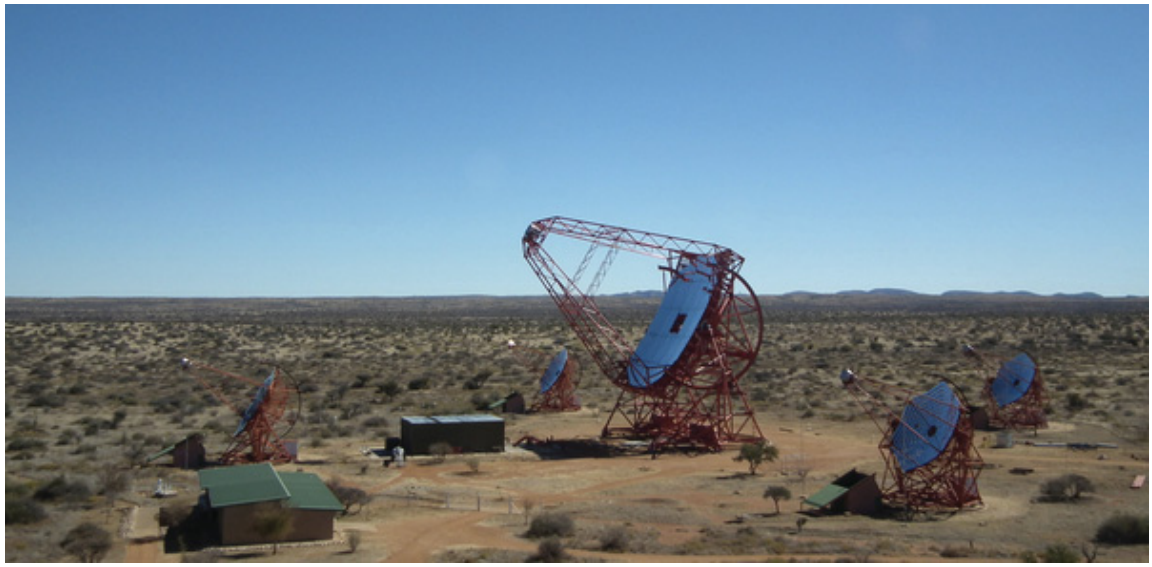

Figure 2–9: The H.E.S.S. telescopes. Image Credit: [20].

and cameras that brought significant improvement of the instrument performance [22, 23]. The MAGIC telescopes have a 3.5° field of view. Figure 2–10 shows the MAGIC telescopes.

Figure 2–10: The MAGIC telescopes. Image Credit: [21].

VERITAS

Very Energetic Radiation Imaging Telescope Array System (VERIAS) [24] is a system of four 12 m diameter IACTs; it is also the instrument of focus for this thesis. We will describe more details of VERITAS in Chapter 3.

FACT

The First G-APD[2] Cherenkov Telescope (FACT) [25] is a single telescope with a 4m diameter reflector and a field of view of 4.5°. The FACT telescope is located at the same site as the MAGIC system. The FACT telescope is a platform to test the feasibility of silicon photo-multipliers (SiPM) for use in VHE gamma-ray astronomy. It is also the first fully automated Cherenkov telescope [26]; the telescope is capable of taking data without an operator on site. Figure 2–11 shows the FACT telescope.

Figure 2–11: The FACT telescope. Image Credit: [25].

2.3.2 HAWC

The High Altitude Water Cherenkov Experiment (HAWC) is a gamma-ray observatory located on the Sierra Negra Volcano in Mexico at an altitude of

[2] Geiger-mode Avalanche Photodiodes

4100 m [27]. HAWC is the successor to the Milagro [28] gamma-ray observatory. As opposed to observing Cherenkov light from air showers using optical instruments, HAWC is made up of 300 water tanks and each tank is coupled with four PMTs (the water Cherenkov detectors). HAWC detects air showers by detecting Cherenkov light produced by charged particles within an air shower when they enter the water tanks. The HAWC experiment, compared to its IACT counterparts, has a higher energy threshold and worse angular resolution but has the advantage of a longer duty cycle (can operate in daytime) and a wide field of view. Figure 2–12 shows the HAWC detectors.

Figure 2–12: Picture of the HAWC detector. Image Credit: [29].

2.3.3 The Future: Cherenkov Telescope Array

The first decade of the 21st century saw the significant development in VHE gamma detection technology that led to the three major IACTs (VERITAS, H.E.S.S., MAGIC). The plethora of astrophysics science results produced by these instruments has generated considerable interest from both the astrophysics

community and the particle physics community to construct a next-generation instrument with higher sensitivity. The current IACTs, while successful, have limited flexibility for large improvements in sensitivity and providing data to the wider community. The Cherenkov Telescope Array (CTA) is hence proposed as the next step in the development of VHE gamma-ray instruments. The CTA collaboration is a worldwide effort incorporating many of the experts and institutions involved in the development of the three current IACTs; the designs of the telescopes are based on currently available technology (optics, electronics ... etc.). These technologies have been demonstrated to be successful through the past decade.

There are several aims of the CTA instrument. The first aim is to increase the sensitivity around 1TeV by an order of magnitude over the present IACTs. Secondly, CTA is being designed to have a uniform energy coverage from tens of GeV to 100 TeV. Lastly, it aims to increase angular resolution and hence the ability to study extended sources. CTA can achieve these goals by having a larger collection area with more telescopes installed and novel telescope designs. To view the whole sky, the proposed CTA observatory will consist of two arrays, one in the northern hemisphere and one in the south. The South array will be the main array to have better coverage of the galactic centre. The projected sensitivity compared to the other instruments mentioned in this section is shown in Figure 2–13; an order of magnitude improvement in sensitivity over the current instruments is expected.

The current design of CTA consists of three types of telescope: small size telescopes (SST, 5-8 m diameter), medium size telescopes (MST, 10-12 m diameter) and large size telescopes (LST, 20-30 m diameter). The purpose of varying telescope sizes is to cover a wide range of energies. Each size of telescope is optimal for ~ 2 decades in energy. The projected array will have 8 LST (4 south, 4 north), 30 MST (25 south, 15 north), and 70 SST (all south) [30].

Unlike the current IACTs, where data are proprietary to each collaboration, CTA will be operated as a proposal-driven open observatory. The data products and analysis tools of CTA will be open to the public akin to the Fermi/LAT data [31]. A more detailed discussion will be provided in Chapter 4.

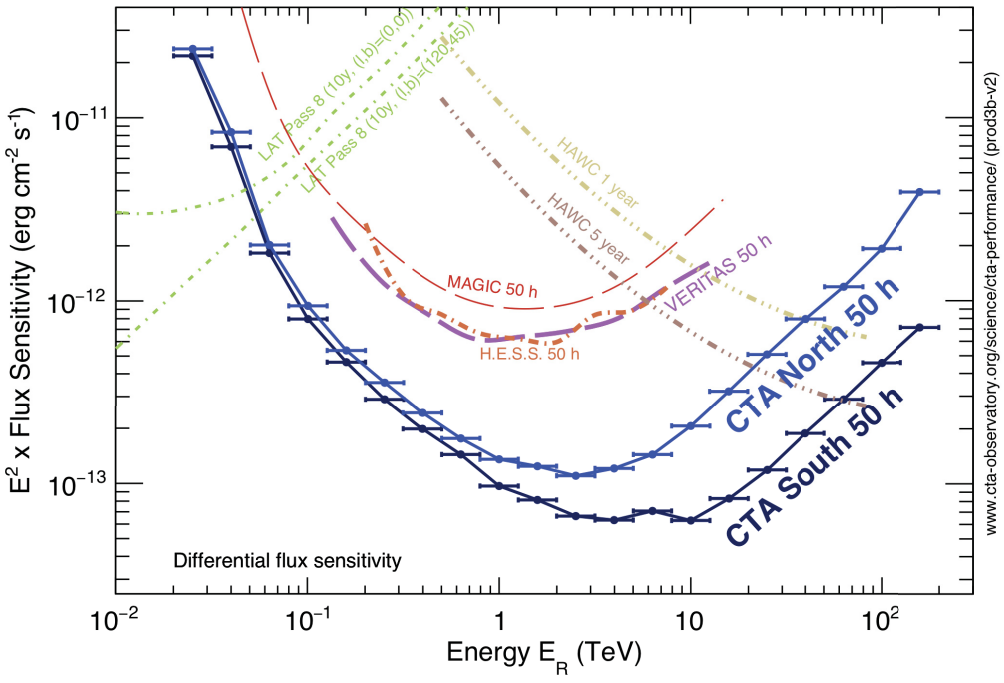

Figure 2–13: Projected sensitivity of CTA compared to current gamma-ray instruments. Image Credit: [30].

3

The VERITAS Experiment

In the last chapter we noted that VHE gamma-rays can be detected by ground-based instruments through detection of the Cherenkov light produced by charged particles in a gamma-ray initiated extensive air shower using IACTs. The Very Energetic Radiation Imaging Telescope Array System (VERITAS) is one of the three major operating IACTs. The specifics of the VERITAS instrument will be described in subsequent sections.

Figure 3–1: Photograph of the VERITAS telescopes and the control centre (Photo taken from [24]).

VERITAS consists of four telescopes of the same design. It is based at the Fred Lawrence Whipple Observatory in southern Arizona, USA, at an altitude of 1270 m. The four telescopes are arranged in a diamond shaped area with sides $\sim$ 100 m (Figure 3–2) to ensure optimal collection area yet have more than

one telescope detect the Cherenkov light from an air shower. The first telescope was constructed in February 2005, and the full array was completed in 2007. The initial configuration of the array was suboptimal due to conflicts with local authorities; the current configuration of the four telescopes was achieved in 2009 after the relocation of the telescope T1.

Figure 3–2: A satellite image of the VERITAS array. The four telescopes are marked with red rectangles; each telescope is assigned a number from one to four. Just south of T3, the old location of T1 prior to the move in 2009 is also marked. Picture credit: Map data ©2015 Google

3.1 Telescope Design

The main component of a VERITAS telescope is a 12 meter diameter spherical reflector of Davies-Cotton design [32]. The reflector is formed by mounting 345 hexagonal spherical mirror facets on a steel optical support structure (OSS) with triangular three-point suspension mounts (Figure 3–3). This allows each of the 345 mirrors to be individually adjusted for alignment. The radius of curvature of the reflector is approximately 24 meters, which corresponds to a 12 meter focal length.

An advantage of the Davies-Cotton (DC) design is that a collection of smaller mirror facets are cheaper to manufacture than a single large mirror. The spherical

mirror facets are all identical, unlike the parabolic counterpart which requires a mirror facet corresponding to the part of parabolic structure where it is located. This feature allows for easier maintenance as the mirror facets can be swapped and replaced easily. The on-axis and off-axis aberrations of the spherical mirror are also smaller than their parabolic counterparts. However, the DC design comes with a disadvantage. The wavefront of light reflected off the mirror is not isochronous when reaching the focal plane; a spread of approximately 4 ns is introduced to the Cherenkov light wave front.

Figure 3–3: Picture of a VERITAS mirror mount. Each of the three points of the mount consists of a mounting bolt, a fine-alignment screw and a gimbal. Image credit: Andrew McCann.

The mirror facets are made of front-aluminized polished glass anodized at an on-site optical coating facility. The anodization of the aluminum coating increases the durability of the mirror and also enhances the peak reflectivity [33]. At the

VERITAS basecamp, a collection of 120 spare mirror facets are maintained and used to replace groups of mirrors on each telescope on a rotating basis. Regular recoating of mirror facets is essential to maintaining reflectivity as the mirrors degrade due to exposure to dust.

The OSS is mounted on an altitude-azimuth positioner. The telescope can slew at a speed of 1°/s with a pointing accuracy of 50-100 arcseconds. The camera is mounted to the OSS with four arms and a set of counterweights is mounted to the back of the OSS to balance the structure. An electronic trailer is located next to each telescope to house the electronics for the data readout and monitoring systems. Figure 3–4 shows a picture of a VERITAS telescope with each component discussed here labeled.

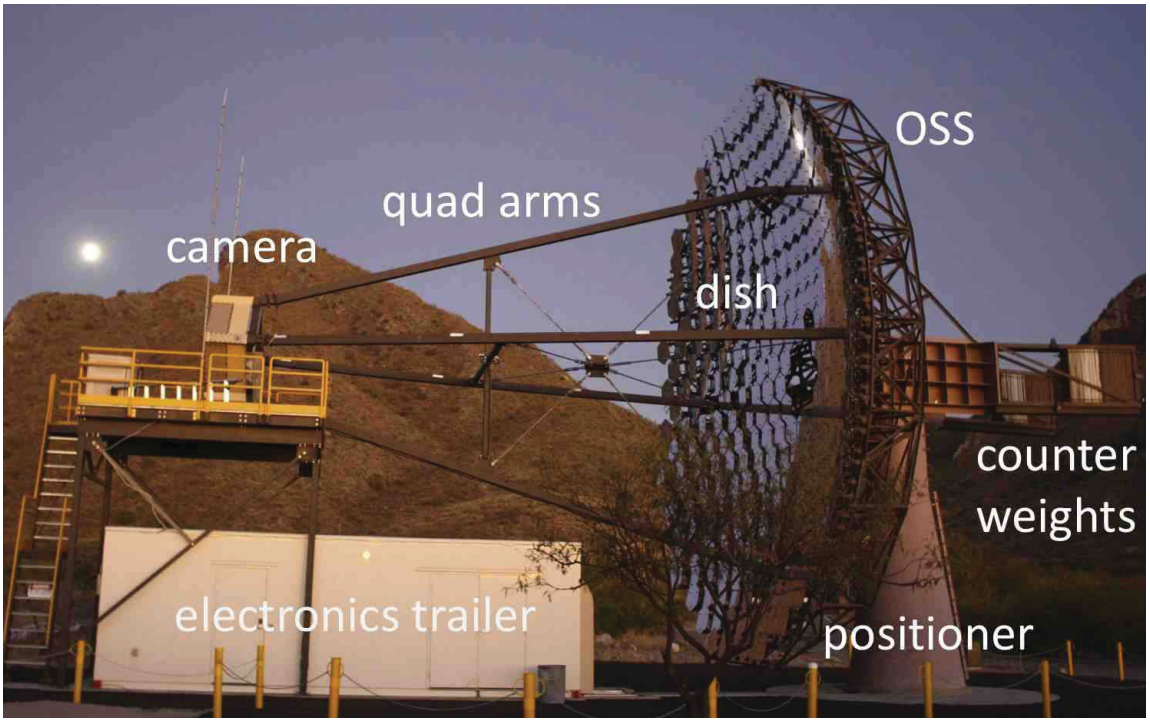

Figure 3–4: Picture of a VERITAS telescope (T1) with the components of the telescope labeled.

3.2 Camera

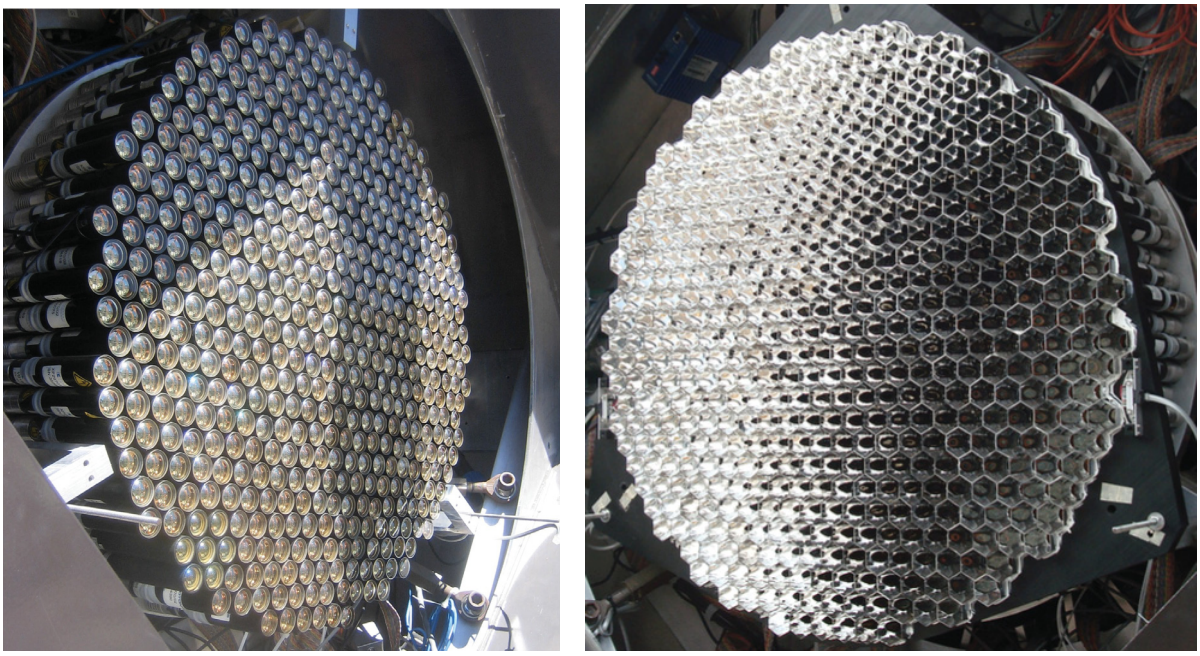

Figure 3–5: A VERITAS camera. (Left) PMT pixels. (Right) Camera with light cones installed. Image Credit: Andrew McCann [18].

The VERITAS camera (Figure 3–5) is a pixelated photon detector made up of 499 photo-multiplier-tubes (PMT) tiled in a hexagonal lattice. A PMT is a glass vacuum tube with the inner front coated with a photocathode (metal sensitive to light). When the photocathode absorbs a photon with enough energy, an electron is knocked out of the metal. This electron allows the transformation from photon into electronic signal. The signal is amplified by accelerating the electron to hit a chain of dynodes to generate more free electrons.

The VERITAS camera went through a major upgrade in 2009. The first generation of the cameras were built with Photonis XP 2970/02 PMTs. In 2009, the Hammamatsu R.10560-100-20MOD PMTs were installed to replace the old PMTs. The Hammamatsu PMTs have better peak quantum efficiency ($\sim$ 35% at 350 nm) compared to the Photonis PMTs ($\sim$ 25% at 320 nm). The upgrade makes the camera more sensitive to air showers with dimmer Cherenkov light output

thereby lowering the energy threshold of the instrument. The lowered energy threshold is useful for observation of sources with a softer energy spectrum such as VHE gamma-ray emission from pulsars and blazars with large redshift.

Every PMT installed in the VERITAS cameras has a 28.6 mm radius circular front face. This geometry leaves gaps on the focal plane. To effectively collect Cherenkov photons and prevent contamination, every PMT is coupled with a light cone in the shape of a modified Winston cone with cone angle $\sim 30^\circ$ (i.e. the angle beyond which a photon cannot reach the PMTs). The original Winston cone design [34, pg.160] has a circular cross section; however to effectively tile the camera, the light cones used at VERITAS have a modified form that has a hexagonal entry that gradually transforms into a circular exit to be coupled to a PMT. The light cone plate increases the light collection by $\sim 65\%$. Every PMT/light cone pixel covers 0.15° of the sky. In aggregate, the cameras have a 3.5° field of view (FOV). UV filters can also be installed between the light cones and the PMTs for bright moon light observations [35].

3.3 Data Acquisition

The signals from the PMTs are continuously digitized by a custom-built 8 bit flash analog-to-digital-converter (FADC) at the sampling rate of 500 MHz and stored temporarily in a 65μs buffer. To extend the dynamic range of the digitizers, the signals from the PMTs are sent to both a low and high gain amplifier. If the high gain signal exceeds the dynamic range of the digitizers, the low gain signal is digitized instead. This mechanism is called the high-low gain switch. Since not all the digitized data can be or needs to be stored, VERITAS deploys a three-level trigger system to reduce noise from background light. Digitized PMT outputs are read out and stored only when criteria for all three levels are met.

3.3.1 Triggers

L1 Trigger: Pixel

The first-level trigger (L1) is a pixel trigger. This level of trigger requires the pulse from a PMT channel to exceed a specific threshold. This trigger reduces the chance of triggering on background light from the environment (e.g. night sky background (NSB)) and electronic noise. The L1 trigger is implemented by using constant-fraction-discriminators (CFD). CFDs ensure the trigger timing to be stable and pulse-shape independent. The CFD output pulses are then sent to the level-two trigger (L2).

L2 Trigger: Telescope

The L2 trigger is a telescope level trigger; it is a topological trigger that looks for patterns in the L1 trigger. The Cherenkov light image from an air shower is expected to hit a group of pixels while the L1 triggers due to NSB are random across the camera. To suppress the NSB triggers, L2 requires that a telescope receive a L1 trigger from 3 neighbouring PMT channels within a 5 ns time window.

The L2 trigger system also has gone through a major upgrade since first light. The current L2 trigger system is implemented using field programmable gate array (FPGA) [36] and was installed in 2011 to replace the old hard-wired system. The main components of the L2 system are three Xilinx Virtex-5 FPGAs called the L1.5 boards and a Virtex-4 FPGA board that is called the L2 board. The camera is divided into three equal sectors and the CFDs from each sector are fed into the three L1.5 boards to check for coincidence of 3 neighbouring pixels. The L2 board then serves as an OR gate between the three L1.5 boards and forwards the L1.5 trigger to the L3 trigger system. The L1.5 board can apply changeable delays to individual CFD input signals before entering the coincidence check; this feature allows the new system to synchronize the signals from the CFDs to remove relative delays due to transit time differences between channels. The spread of the CFD

signal timing reduces from $\sim$ 1 ns down to $\sim$ 0.2 ns; the better timing resolution means that the coincidence window can be shortened (from 8 ns to 5 ns) to further reduce NSB triggers (or equivalently, with a lowered CFD threshold and thus energy threshold). The last level of the trigger system uses the L2 trigger from each telescope to determine whether to store the data.

L3 Trigger: Array

The final trigger (L3) is an array trigger. The L3 system (hosted in the control building) looks for a coincidence of the L2 triggers from a set number of telescopes within a 50 ns window. The threshold for the number of telescopes to trigger L3 is programmable and is normally set to two. While the L2 system is already good at suppressing the NSB induced trigger, Cherenkov light generated by muons produced in hadronic showers passing close to each telescope can produce Cherenkov light images that can easily trigger the L2. With the $\sim$ 100 m separation between telescopes, a single muon is unlikely to trigger more than one telescope. So, the L3 trigger, with the minimum requirement of 2 telescope coincidences, can strongly suppress (a factor of $\sim$ 10) the local muon triggers.

Due to different cable lengths from each telescope to the L3 system, the L2 triggers from each telescope need to be synchronized by adding delay to the L2 signal. The amount of delay for each telescope depends on the pointing position of telescope so the L3 system has programmable delay modules to account for this delay.

CFD Threshold and Bias Curve

The L1 CFD threshold is the one setting that is used to adjust the trigger system. The threshold level strongly affects the hardware energy threshold and the deadtime (by affecting the trigger rate) of the system. The threshold of the CFD is optimized so that it suppresses spurious triggers due to NSB but retains the majority of the triggered events that are due to air showers. To do so, the

response of the instrument as a function of CFD threshold needs to be understood. It is done through inspection of the bias curve, which is a plot of the trigger rate versus CFD threshold. In a typical bias curve (Figure 3–6), there are two different regimes: in the high threshold regime the trigger rate is mainly dominated by triggers caused by cosmic rays, and at low threshold there is a steeply falling component as the CFD threshold raises that is dominated by NSB triggers. For normal observations, the CFD threshold is set at 45 mV; for brighter observation conditions, this threshold needs to be raised.

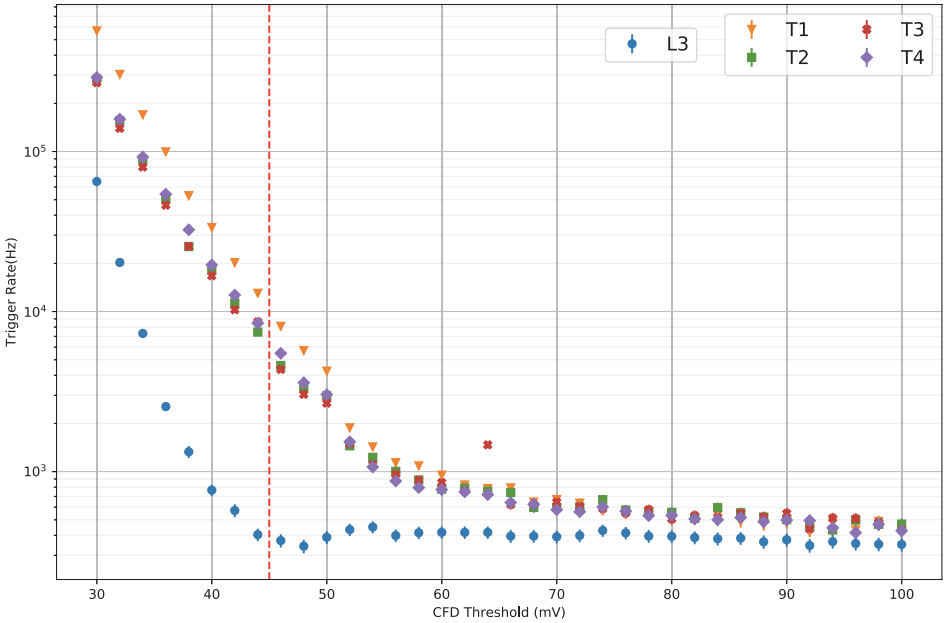

Figure 3–6: Bias curve of run 94174 taken on 2019 Oct 19. The L3 rate is drawn together with the L2 rate of the four telescopes (T1 to T4). The vertical red dashed line marks the normal CFD threshold at 45 mV.

3.3.2 Data Readout

When a L3 trigger condition is satisfied, the L3 computer in the VERITAS control building sends a signal to the computers in each telescope's electronic trailer to save data in buffer to disk. First, the Event Builder software saves

the FADC traces and some auxiliary data such as the GPS time of the event and the pixels that trigger L1 locally at each telescope computer. The data of individual telescopes are then sent to the Harvester computer in the control building to be combined into the final data product. The data is saved in a custom file format: the compressed VERITAS bank format (cvbf) file. Normally, the data of VERITAS are taken in 30 minutes segments (called a **Run**). Each run is saved as one cvbf file and uploaded to the data archive hosted at UCLA for the collaboration to perform offline analysis.

3.4 Instrument Epochs

As mentioned in the earlier sections, the VERITAS instrument underwent two major upgrades since the first-light in 2007. Since the upgrades modified the performance of the instrument, we separate the time of operation of VERITAS into three epochs.

- **V4** Epoch: From first light to the relocation of T1 in 2009 (2007 - 2009).
- **V5** Epoch: After the relocation of T1 and before the PMT upgrade (2009 - 2012).
- **V6** Epoch: After the PMT upgrade (2012 - now).

The instrument has been stable since the V6 epoch and it is also the most sensitive one.

3.5 Data Quality Monitoring

Depending on the observation conditions, the quality of data taken each night needs to be assessed. Three far infrared radiometers (FIR) are installed at the observatory to monitor the sky conditions. Two FIRs are installed on the telescope OSS (T2, T3) so they point in the same direction as the telescopes. The remaining FIR is setup to point straight up at zenith. When clouds pass through the field of view of the telescopes, the sky temperature measured by the FIR increases, so one can use it as a signature of the sky conditions within a run. Looking at the

FIR measured temperature together with the L3 trigger rate allows us to decide whether to remove part of the data in a given run due to clouds. As two examples, Figure 3–7 shows the FIR output overlaid with the L3 rate for a normal clean run and a run with cloud coverage. In the case shown in Figure 3–7, the one run with cloud coverage is still usable for analysis if the data between $\sim$ 750 s and $\sim$ 1000 s are removed.

For every run, there are associated weather scores. The observers of the night will assign a weather score (from A to D) to each run they take; this scoring system is rather subjective and is mainly based on the observers' assessment of the night's sky condition. An alternative is to mark the weather score based on the variation of FIR temperature within a run; however, this method is generally quite strict and tends to give low scores even if only a small part of the data is affected by weather. Generally, both scores are considered in conjunction.

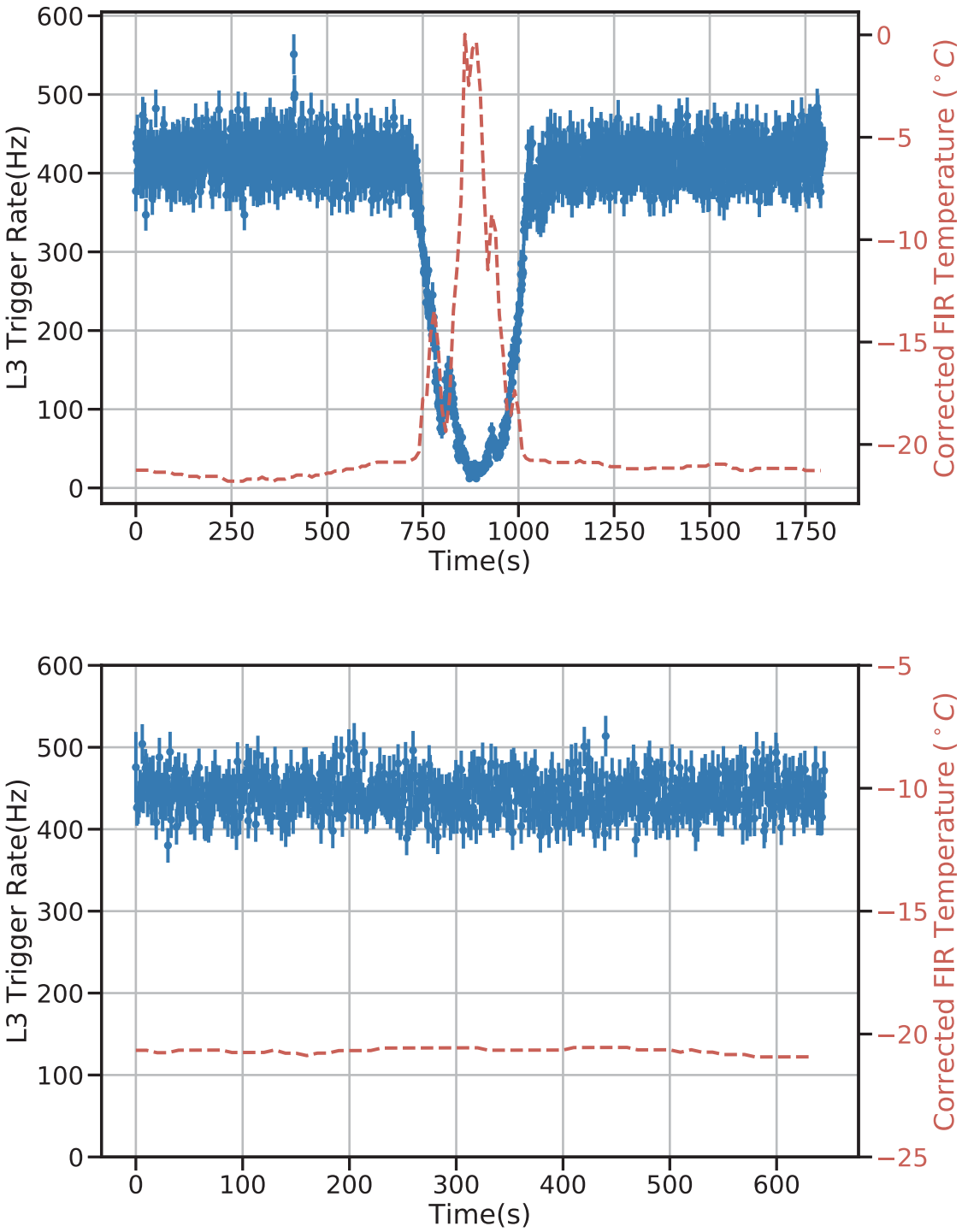

Figure 3–7: FIR temperature and L3 trigger rate of two runs, one with clouds passing through (top) and one with a clear sky (bottom). The blue points are the L3 trigger rate (dead time corrected) and the red line is the sky temperature measured by the radiometer mounted on T2 (scale on the right). A clear anti-correlation between the trigger rate and sky temperature can be seen.

4 IACT Data Analysis

4.1 Overview

The raw data of VERITAS consist of digitized PMT traces from all participating telescopes for each triggered event. There are also other auxiliary quantities such as GPS timestamps of events and binary masks identifying the channels triggering L1 and telescopes contributing to the L3 trigger. These data are pushed through an analysis pipeline to produce high level analysis results such as the strength and significance of gamma-ray signals in the data. Conceptually, we can group the steps of analysis into three levels:

1. Low Level Analysis: Calculation and application of calibrations. Extract Cherenkov signal (if any) from PMT traces and conduct single telescope image analysis.
2. Intermediate Level Analysis: Analysis done at the event level. Combining images from all triggered telescopes to reconstruct shower properties such as arrival direction, impact distance, and primary energy.
3. High Level Analysis: Use the list of events and the properties associated with each event to perform source detection and astrophysical analysis such as flux calculation, light curve calculation ... etc.

In the next three sections, the specifics and steps within each level of analysis are presented. The overview of the software that is used for VERITAS data analysis will follow. We will discuss the structure of the two analysis packages used by the VERITAS collaboration: `VEGAS` [37] and `EventDisplay` [38]; also, the software for generating simulations will be covered. This chapter will finish with a discussion on the future of data from fromCT such as VERITAS (we refer to these data as legacy data hereafter).

4.2 Low Level Analysis

4.2.1 Data Calibration

The first step of the analysis is to convert the digitized traces of the photo-multiplier tube pulses into calibrated measures of the amount of Cherenkov light received by the camera. To remove the baseline for the traces when there is no Cherenkov light measured, pedestal events are injected at a 1 Hz frequency. These events are force-triggered by the *VERITAS DAQ* and usually have no external Cherenkov light. Pedestal values are calculated by taking the FADC traces (on a per-channel basis) and averaged over the sum of a number of FADC samples (e.g. 7 samples). The standard deviations of the summed traces are also calculated and serve as a measure of the background light in the sky (night sky background, NSB). Because the amount of NSB contribution to the baseline level can vary with time and pointing direction during a run, the above calculations are applied to groups of 3-minute slices. For each event, the pedestal values are then subtracted from the traces.

Once the pedestal is subtracted from the traces we can proceed to the next step and start looking at the traces themselves. To calculate the signal strength from the Cherenkov light, a double-pass method is used. For the first pass, the summation of traces is performed over a wide summation window (16 samples); at the same time, the $T0$ point (defined as the time at which the trace reaches

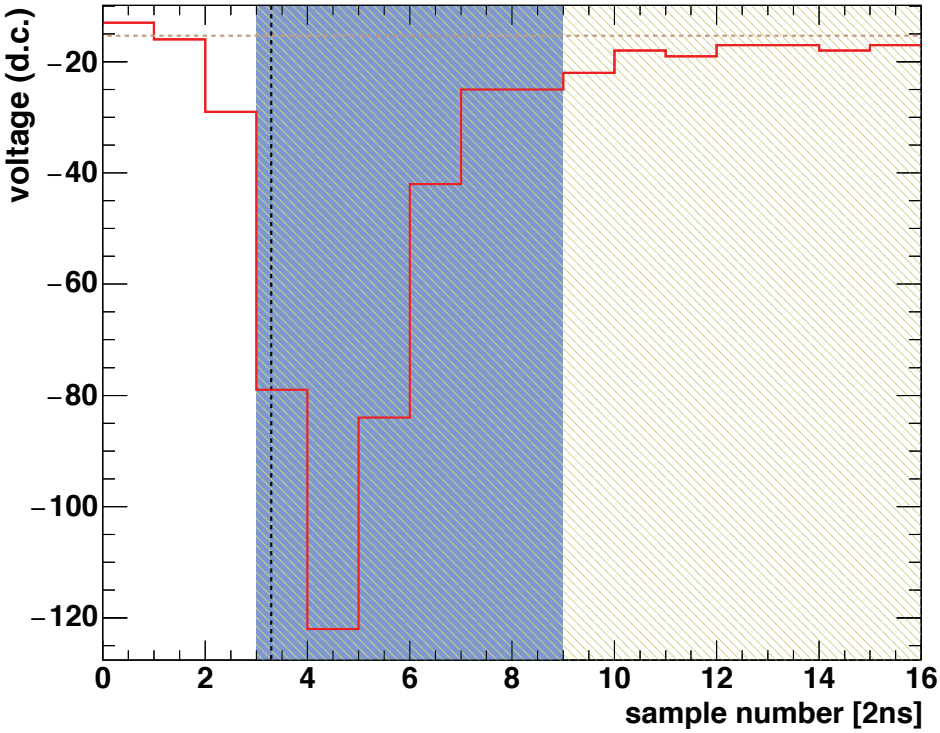

Figure 4–1: Example of a PMT trace with a Cherenkov light signal. The blue shaded region is the integration window chosen after the double-pass process. The vertical black dashed line represent the position of $T0$ and the brown horizontal line labels the pedestal level.

half of its peak amplitude) of a trace is calculated. See Figure 4–1 for an example of the PMT trace. The $T0$ gives the arrival timing of the Cherenkov pulses at each PMT. Due to the difference in time required for Cherenkov light to travel from different points in a shower to the telescope, there are systematic differences in the arrival time of Cherenkov pulses across a shower image (with a gradient on the order of $\sim$ 2 ns/deg). An example of such a time difference can be found in Figure 4–2. The first pass of trace summation is used to create a preliminary shower image (after image cleaning, see next section). In the second pass, the $T0$ information is used to calculate the arrival time gradient along the primary axis of the preliminary shower image. The second pass of trace integration is then calculated using a smaller integration window with the start of the window adjusted using the time gradient calculated from $T0$. This method yields a higher

signal-to-noise ratio and avoids the issue of losing signal for high energy showers (> 1 TeV) when using a fixed time window.

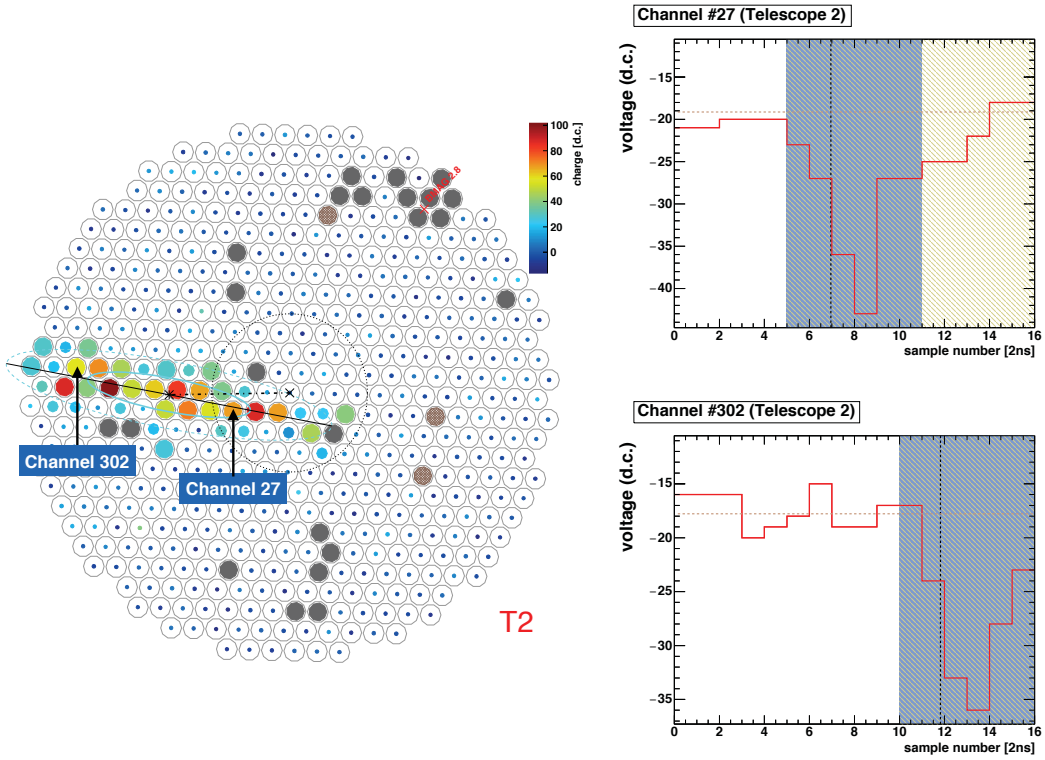

Figure 4–2: Example of Cherenkov light arrival time difference for an air-shower triggered event. Traces from two channels (channel 27 and 302) are shown. The $T0$ difference here is around 10 ns which is larger than a typical event due to its large distance (440 m from T2) to the telescopes. In general, once a telescope lies outside of the Cherenkov light pool, a larger impact distance will cause a larger time gradient. For more discussion on the relation of time gradient of an image and impact distance see [39]. The group of grey pixels to the upper right are pixels that are suppressed due to the presence of a bright star in the field of view.

Nightly LED flasher runs are taken to measure the relative gain of each PMT and the timing characteristics. The uniform light produced by the flasher allows us to calculate the relative gain using the difference in responses to the flasher pulses by each PMT. The nightly relative gains are applied to data analysis to adjust integrated traces. The timing difference of each channel due to cable length and electronic delays can be obtained as the flasher pulses arrive at each PMT

simultaneously (at least within the timing resolution of the FADCs). The timing of data events are adjusted accordingly.

4.2.2 Image Cleaning

For a triggered event, not every PMT receives Cherenkov light pulses. Image cleaning is the process of removing channels unrelated to the shower image from the analysis. A dynamic thresholding method is used for image cleaning.The selection of pixels is based on the signal-to-noise ratio of that channel:

$$(S/N)_k = \frac{Q_k}{\sigma_k} \tag{4.1}$$

where Q_k is the integrated trace from channel k and σ is the standard deviation of the pedestal. To select channels of interest, a high threshold of $(S/N) > 5$ is first applied; pixels passing this criteria are called "image" pixels. At the first pass, this only includes the brightest core of the shower image; the dimmer rim of an image wouldn't necessarily be included. So, in order to include the dimmer pixels, a second pass is applied. All the pixels neighbouring image pixels are inspected and a lower threshold of $(S/N) > 2.5$ is applied; the selected pixels are called "border" pixels. The combined list of "image" and "border" pixels is then used for further analysis.

4.2.3 Image parameterization

The air shower image is a 2D projection of the distribution of the charged particles in the air shower; since hadronic showers have more substructure and larger lateral distribution (see Chapter 2), by parameterizing the image it is possible to differentiate between the two. In 1985, Hillas [40] first introduced parameters derived from a moment analysis, which led to the first detection of TeV emission from the Crab nebula using the Whipple-10m telescope [19].

This analysis procedure is based on the assumption that the light intensity distribution $G(x, y)$ in an image resembles an 2-D elliptical Gaussian distribution:

$$-\ln G(x,y) = \frac{(x-\mu_x)^2}{2\sigma_x^2} + \frac{(x-\mu_x)(y-\mu_y)}{\sigma_{xy}^2} + \frac{(y-\mu_y)^2}{2\sigma_y^2} + \tilde{C} \tag{4.2}$$

where $\tilde{C}$ is a constant defining the normalization of the image.

With this assumption, one can calculate the terms $\{\mu_x, \mu_y, \sigma_{x^2}, \sigma_{y^2}, \sigma_{xy}\}$ from the first and second moments of an image (Equation 4.3). Here, (x_i, y_i) is the coordinate of the i-th pixel and S_i is the pedestal-subtracted integrated charge after image cleaning. The average of a parameter $< a >$ is defined as $\frac{\sum_i a_i S_i}{\sum_i S_i}$. The centre of an image is simply the first moment (μ_x, μ_y). The second moments (Equation 4.3) fully describe the rotation angle and half-length of the major and minor axes.

$$\left.\begin{aligned} \mu_x &=< x > \\ \mu_y &=< y > \\ \sigma_x^2 &=< x^2 > - < x >^2 \\ \sigma_y^2 &=< y^2 > - < y >^2 \\ \sigma_{xy}^2 &=< xy > - < x >< y > \end{aligned}\right\} \tag{4.3}$$

In the original proposal of Hillas, there are six parameters derived from the moment analysis of an image. More parameters were proposed and used in the analysis since then; collectively these parameters are generally referred to as Hillas parameters. Here, the original Hillas parameters are listed:

- `Width`(`Length`): The RMS width/length of the shower image's semi-minor/minor axis, denoted w and l.
- `Distance`: The angular distance between the centroid of the image and the centre of field of view.

- `Frac2`: The fraction of the total size contained in the 2 brightest PMTs. This parameter is used to measure the concentration of light; it can be extended to `FracN` to measure the concentration of light in the top n PMTs.

The original analysis of Hillas was applied to Whipple with only a single telescope. There are a few other parameters that are only useful in that context and have since been removed from the current generation of IACT analyses:

- `Azwidth`: The RMS width of the image along the direction perpendicular to the line between the centre of field of view and the centroid of the image. This was used to measure the shape and orientation of the image.
- `Miss`: The perpendicular distance between the major axis of the image and the centre of the camera. This parameter has been replaced by the θ^2 parameter in the more modern analysis (see more details in Section 4.4).

Several new parameters were found to be useful since Hillas' analysis and have been added to standard IACT data analysis; here we list a couple of important ones:

- `SIZE`: The sum of integrated charge of all the pixels in the cleaned image. This parameter measures the brightness of the image. In what follows, it is denoted S.
- `LOSS`: The fraction of the size of the image that is contained on the edge of the camera. It is a first-pass measure of how well the image is contained in the camera.

A graphical representation of the six original Hillas parameters can be found in Figure 4–3.

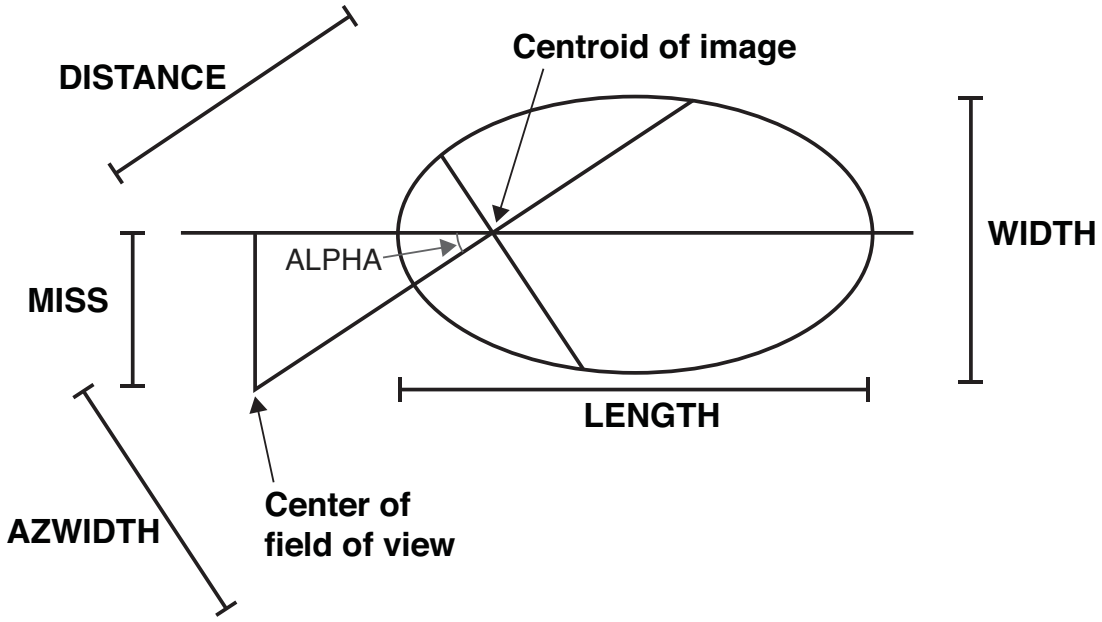

Figure 4–3: Illustration of the original six Hillas parameters. `Azwidth` and `MISS` are no longer used. credit: Figure 4.1 of [11]

4.3 Intermediate Level Analysis

Once we have the single telescope image information, the images from the telescope array can then be combined stereoscopically to reconstruct the geometry and brightness of the air shower and thus the properties of the primary particle. The principle goal of this stage of analysis is to obtain the arrival direction and energy of the primary gamma rays.

4.3.1 Direction and Shower Core Reconstruction

Recall that the showers resulting from gamma-rays interacting with the atmosphere are narrow and long and the shower's major axis is collinear with the arrival direction of the primary gamma-ray (Figure 4–4). This geometry means that the arrival direction of the primary gamma-ray is somewhere on the major axis of a shower image; while there is a degeneracy as to the precise location of the arrival direction of the primary particle, with more than one telescope viewing a shower stereoscopically this degeneracy can be broken.

One way to calculate the direction of a gamma-ray-like event is by first overlaying the shower images (Figure 4–5) and finding the point that minimizes the squared sum of the closest distance to the major axis of each image. The perpendicular distance from a point (x, y) to the major axis of an image can be calculated as follows:

$$l_i^2 = \frac{1}{1 + \tan^2 \theta_i} \left(- \tan \theta_i (x - x_i) + (y - y_i) \right)^2 \tag{4.4}$$

where θ_i is the angle of the major axis of a shower image relative to the x-axis and (x_i, y_i) is the coordinate of an arbitrary point on the major axis. The arrival direction (x, y) is then obtained by minimizing the sum of the squared distances $\sum_i l_i^2 s_i$ weighted by the size of the image. This amounts to solving the following

equations:

$$\begin{cases} (\sum_i S_i \tan^2\theta_i\gamma_i)x - (\sum_i S_i\gamma_i \tan\theta_i)y + \sum_i S_i D_i\gamma_i \tan\theta_i = 0 \\ (\sum_i S_i \tan\theta_i\gamma_i)x - (\sum_i S_i\gamma_i)y + \sum_i S_i D_i\gamma_i = 0 \end{cases} \tag{4.5}$$

where D_i and γ_i are values derived from the angle θ_i and the coordinate (x_i, y_i):

$$D_i = y_i - \tan\theta_i x_i \tag{4.6}$$

$$\gamma_i = \frac{1}{1+\tan^2\theta_i} \tag{4.7}$$

The other method that is implemented in the analysis pipeline is to first determine the points of intersection of the major axes and aggregate the intersection points between pair of lines; a weighted average of the intersection points is then calculated. The analysis presented here performs the weighted average using the following relation:

$$W_{mn} = \left(\frac{1}{S_m} + \frac{1}{S_n}\right)^{-1} \times \left(\frac{w_m}{l_m} + \frac{w_n}{l_n}\right) \times \sin\theta_{mn} \tag{4.8}$$

where m and n denote the telescope pair and θ_{mn} is the angle between the image major axes of the two-telescope images (the other parameters were introduced in the earlier section). The scaling with $\sin\theta_{mn}$ ensures that two images with small angles (i.e. near parallel) will have a smaller weight due to the large error on the intersection point that this scenario introduces. This method was pioneered by the HEGRA Cherenkov telescope array [42].

Another important property of the shower is its location relative to the telescope. The location of the shower major axis intersecting with the ground plane is called the *Shower Core*; it is the position on the ground if the particles in the air shower are not absorbed by the atmosphere (Point **P** in Figure 4–4). The reconstruction of the *Shower Core* position is essentially the same as direction; the difference is that instead of performing the analysis in the camera plane the shower

images are projected onto the ground plane (Figure 4–6). The *impact parameter* (denoted r) or *impact distance* is the distance between a telescope and the shower core in the plane perpendicular to the shower axis (distance between **Ti** and **P** in Figure 4–4); it is an important parameter when estimating the energy of the primary gamma ray.

The two methods described above are the default direction and core reconstruction algorithms for the two analysis packages of VERITAS.

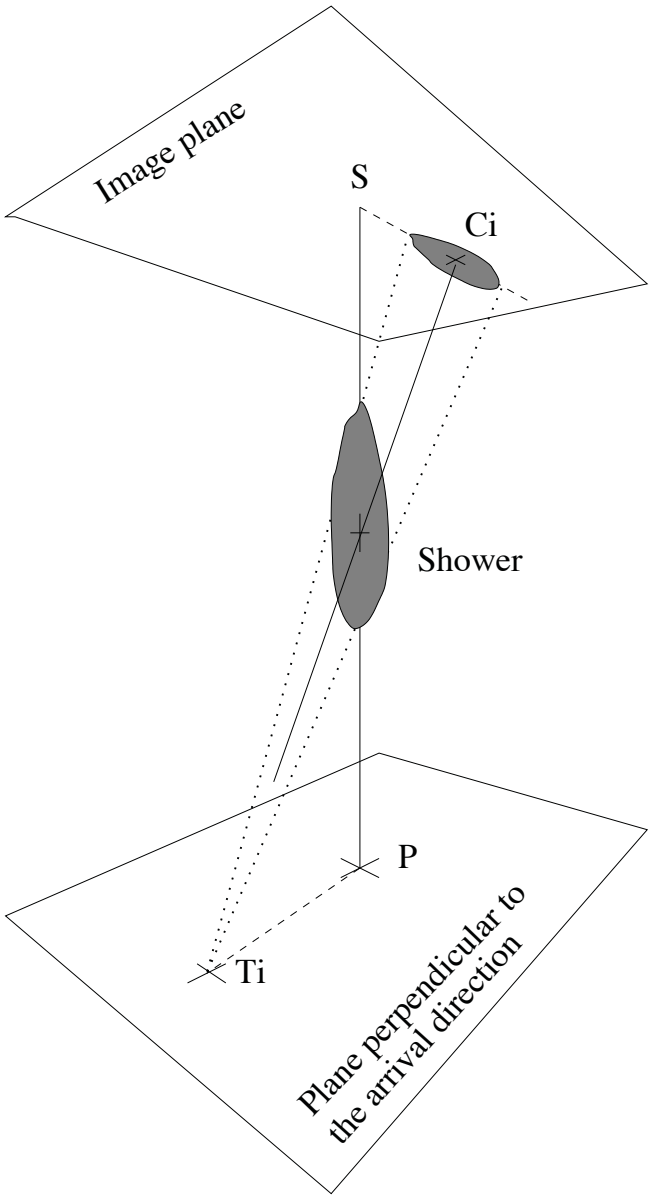

Figure 4–4: Schematic of how the shower is projected onto the camera plane. **P** is the core position, **S** is the source location. **Ti** is the telescope location, and **Ci** is the location of the image centroid in the camera plane. Image Credit: Figure 1 in [41].

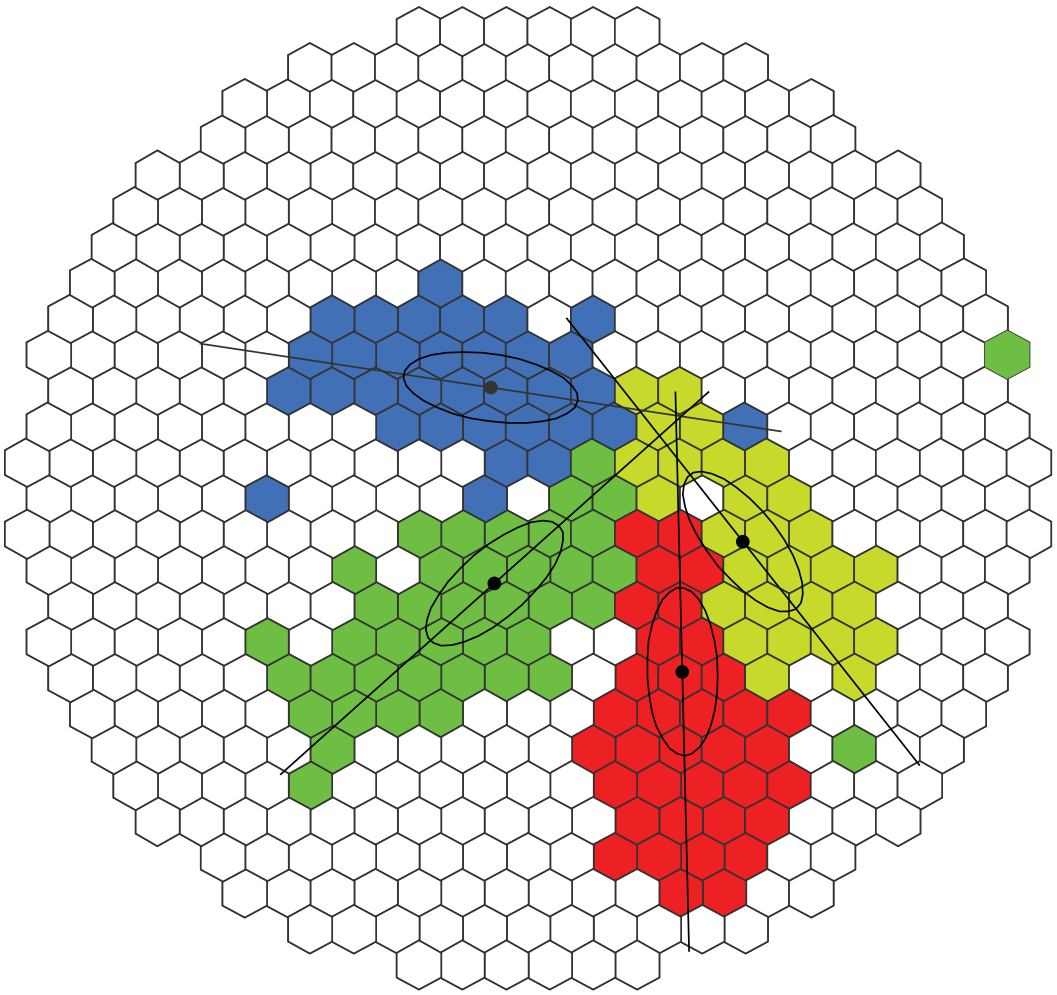

Figure 4–5: Schematic arrival direction reconstruction. The four camera images have been superimposed, and the arrival direction is calculated using the major axes of the four images. Image credit: A. McCann.

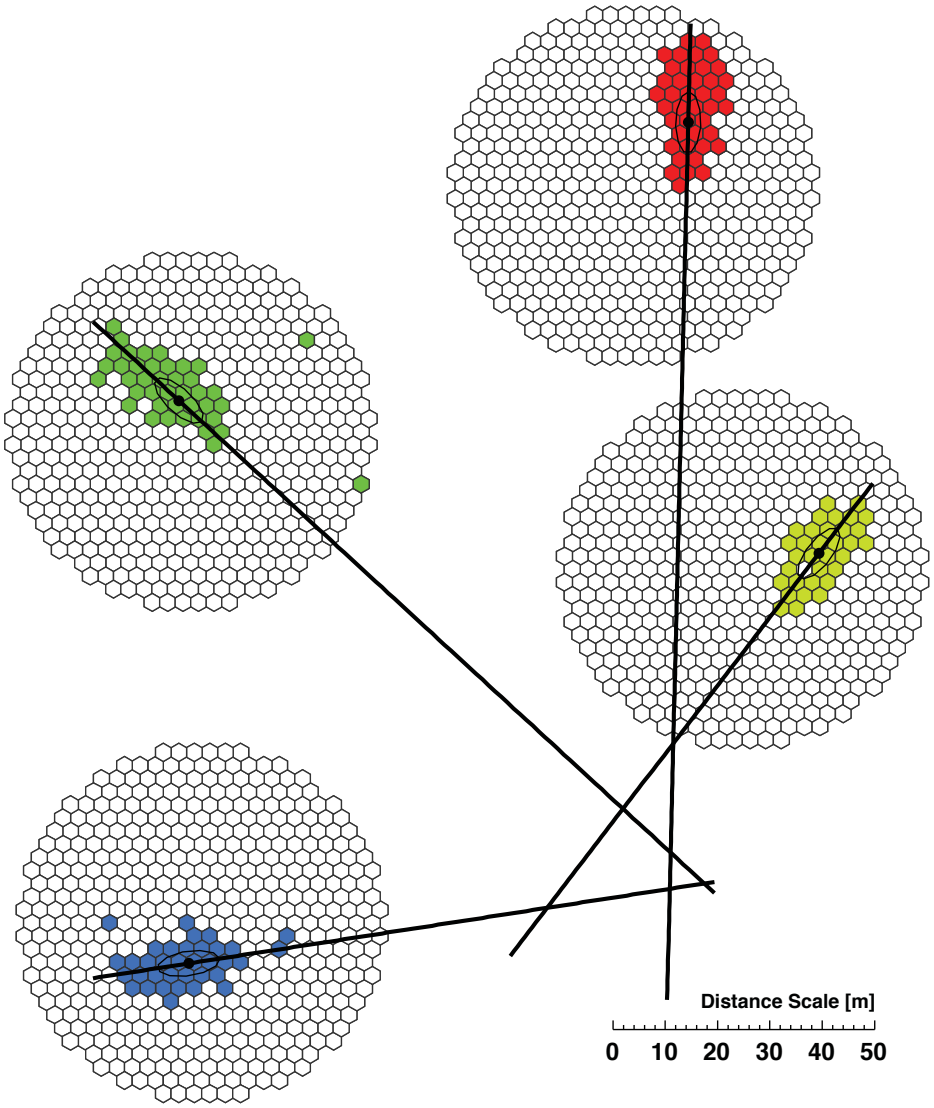

Figure 4–6: Schematic of the shower core location reconstruction. The four camera images are projected onto the ground plane, and the core location is calculated using the major axes of the four images in the same way as the arrival direction reconstruction. Image credit: A. McCann.

4.3.2 Height of Shower Maximum Reconstruction

One can also determine the height of the air shower through a relatively simple geometric analysis (Figure 4–4). Since extensive air showers are extended objects, the exact position along the shower axis to be associated with the "height" of the showers is subject to discussion. In general, the position where an air shower contains the maximum number of particles, named *Shower Maximum*, is of interest in characterizing the properties of an air shower. Traditionally, the reconstruction of the height of shower maximum is done by reconstructing the corresponding position of the centroid of the shower images in physical space. These methods are in fact subject to biases; more discussion on the correction and biases will be presented in Chapter 6. Here, we will only describe the standard methods implemented in the VERITAS analysis chain.

Two Telescope Parallax Method

The main analysis method that is used by both `EventDisplay` and `VEGAS` is the two telescope parallax method. Figure 4–7 shows a schematic of the geometric set-up; by having two telescopes seeing the same shower the parallax angle ϕ of the two telescopes to the air shower can be obtained from the distance of the centroid of the images from each telescope.

The height of the shower can then be calculated as:

$$h_{ij} = \frac{d_{ij}}{\phi_{ij}} \tag{4.9}$$

where d is the distance between two telescopes on the ground and i and j denote the telescope pair that is being analyzed. Here, the approximation $\tan\phi \sim \phi$

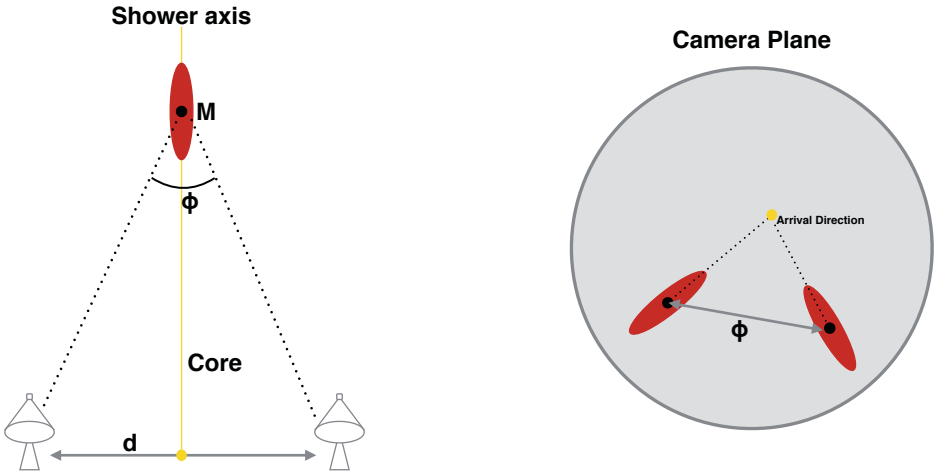

Figure 4–7: Schematic of the reconstruction of the emission height using the two telescope parallax method. The shower is represented as the red ellipse and M is the shower maximum (left). The angle ϕ between the lines connecting the two telescopes to the shower maximum is obtained from the angular distance between the centroids of the shower images (right).

is used; this is valid given that ϕ cannot be larger than 3.5° (VERITAS' field of view). The calculation is then averaging over all available telescope pairs[1] .

Single Telescope Method

An alternative method that is implemented in `VEGAS` but not widely used by the collaboration is the single telescope method. This method relies on knowing the shower core position and arrival direction *a priori*, which we obtain from the methods described in the earlier part of this section. With a known shower core position and hence a known impact parameter (r) we can use the angular separation between the centroid of the image and the reconstructed arrival direction to obtain the angle between the line from a telescope to the shower and

[1] Note that because not all shower cores lie on the line connecting two telescopes, the value h_{ij} could be different even if looking at the same point in the shower. However, since a typical shower height is $\sim$ 8 km and core distance $<$ 500 m this effect would only contribute less than 1% difference.

the shower axis θ. A schematic drawing of the geometry is shown in Figure 4–8; from simple geometry, we can then calculate the height of the shower as:

$$h_i = \frac{r_i}{\tan \theta_i} \tag{4.10}$$

In the standard implementation the final shower height is also calculated as the mean of all the available telescope values. But as mentioned earlier the method presented here is subject to biases; we will delay the discussion on the method of combination of the individual single telescope heights to Chapter 6.

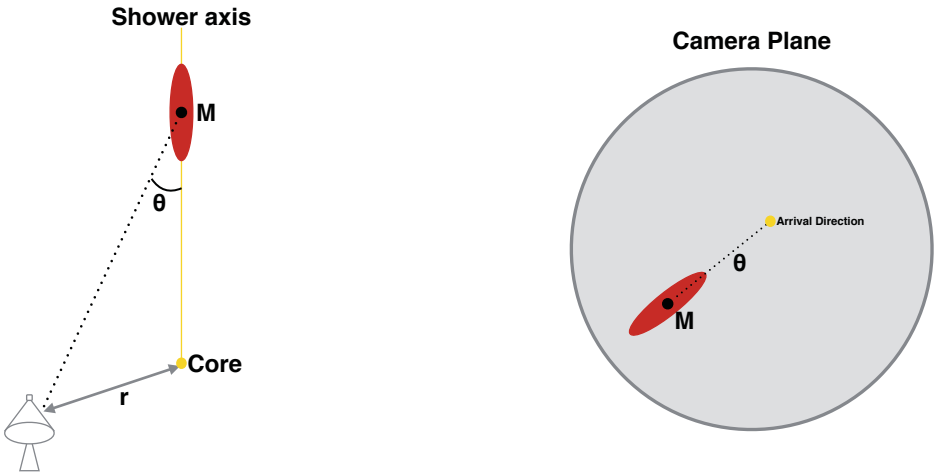

Figure 4–8: Schematic of the reconstruction of the emission height using a single telescope. The shower is represented as the red ellipse and M is the shower maximum (left). The angle θ between the lines connecting the telescope to the shower maximum and the shower axis is obtained from the angular distance between the centroid of the shower image and the arrival direction (right).

4.3.3 Energy Estimation

The last property of the primary gamma ray to be reconstructed is its energy. To first order, the number of charged particles scales with the energy of the primary particle. Hence, a higher energy gamma ray will produce more Cherenkov light. The brightness of the images detected by the telescopes is therefore a good proxy for the primary energy. However, the amount of light received by the telescopes also depends on the distance of a telescope to the showers. The

reconstruction of energy relies on simulating gamma-ray showers and using the shower size and the impact parameter to produce reference tables. At each zenith and azimuth angle, two dimensional tables are filled so one can look up the mean energy $E'(r, S_i)$ and the standard deviation $\sigma(r, S_i)$ of the energy within each impact distance bin.

The reconstructed energy is computed as a weighted average of the look-up energies $E'(r, S_i)$:

$$E = \frac{\sum_{i=1}^{N_{img}} E'(r, S_i)/\sigma^2(r, S_i)}{\sum_{i=1}^{N_{img}} 1/\sigma^2(r, S_i)} \tag{4.11}$$

Figure 4–9 shows an example of such a reference table.

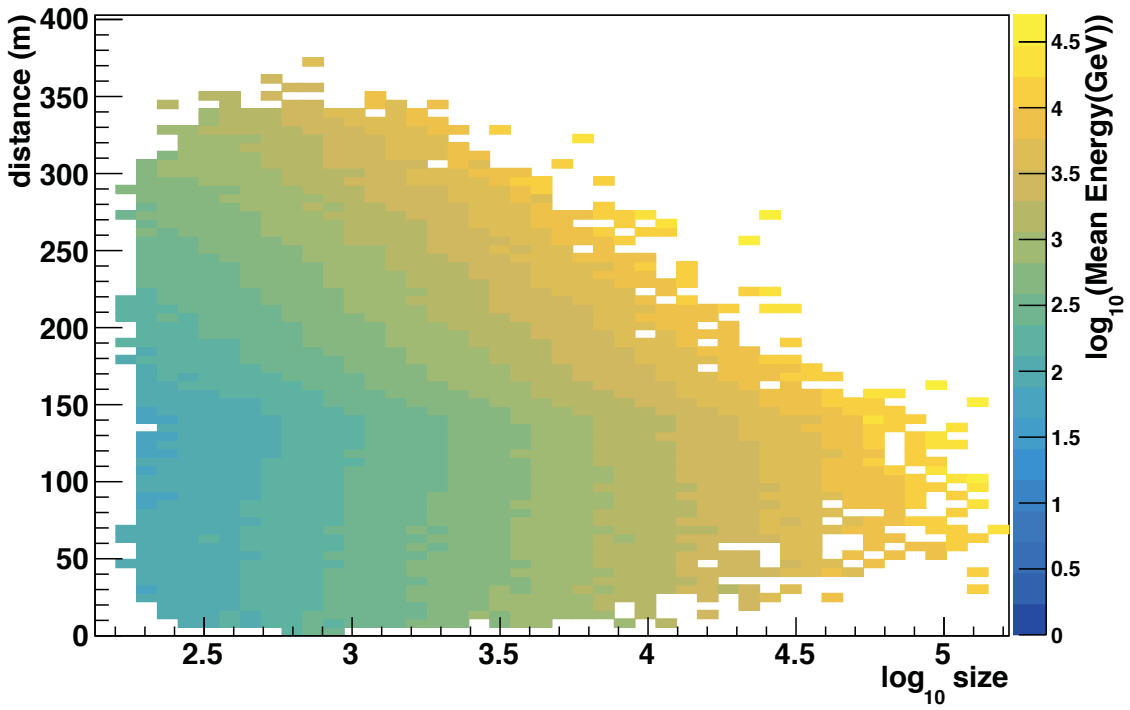

Figure 4–9: Lookup table for mean energy $E'(r, S_i)$. The y axis is the impact distance and the x axis is the log size of the image.

4.3.4 Event Selection

At this stage of the analysis, we have all the required properties of gamma-ray showers reconstructed. The remaining issue is whether the events we have been analyzing are gamma rays or cosmic ray events. The geometrical differences between hadronic showers and leptonic showers mean that we can differentiate the gamma-ray initiated showers using the width and length parameters; hadronic showers create larger and less elliptical images in the camera plane. Width and length of a shower image also depend on the primary energy and distance to a telescope, so to break the degeneracy and to combine images recorded by different telescopes we compare the width and length of an image to the expected image shape of a gamma-ray initiated shower obtained from simulations. These are called *mean scaled parameters*. The definition of mean scaled variables are as follows:

$$MSP = \frac{1}{N_{tel}} \sum_{i=1}^{N_{tel}} \frac{p_i}{\overline{p}_{sim}(\theta_{ze}, S_i, r_i)} \tag{4.12}$$

where p_i is the parameter of interest (*width* or *length*) as seen by telescope i, and $\overline{p}$ is the mean value of the parameter for simulated gamma rays with size s and impact parameter r, observed at a zenith angle θ_{ze}.

The alternative *mean reduced parameters* follow a similar logic but with a slightly different definition:

$$MRSP = \frac{1}{N_{tel}} \sum_{i=1}^{N_{tel}} \frac{p_i - \widetilde{p}_{sim}(\theta_{ze}, S_i, r_i)}{\sigma_p} \tag{4.13}$$

where $\widetilde{p}$ is the median value of the parameter p for the simulated events, and σ_p is the standard deviation. The mean reduced scaled parameters are known to be more robust against outliers. The two main parameters used in gamma-hadron separation are the mean scaled width (MSW) and length (MSL), or the alternative mean reduced scaled width (MSCW) and length (MSCL). Figure 4–10 shows plots of the mean scaled width and length distributions for simulated gamma rays and

events selected from background regions, assumed to be gamma ray free. One can clearly see the difference in distribution between the gamma rays, which have a distribution peaked around 1, and the background events.

Other than the two main parameters (MSL/W or MSCL/W), there are also other less powerful parameters. For example, the reconstructed height of shower max as described in the earlier section is also used since proton initiated showers interact deeper in the atmosphere than gamma-ray initiated showers. Traditionally, gamma-ray like events are selected by setting thresholds on the aforementioned parameters and removing events that have values outside of the desired range. For example, in the case of Figure 4–10, a reasonable selection criteria on MSW would be $MSW < 1.4$. This method is generally referred to as the "box cut" and is the standard approach for VERITAS event selections. Prior to any analysis, the selection cuts need to be decided *a priori*; typically, the cuts are separated into three "classes": soft, moderate and hard. They are optimized according to the spectrum of the sources of interests. The main difference between the different classes is the energy threshold. Soft cuts are used for sources with soft spectral index (less than -2.5), moderate cuts are used for Crab-like spectra (index of -2.5), and hard cuts are used for sources with harder spectra than the Crab.

The "box cut" technique is most efficient if the parameters where the cuts are applied are statistically independent, which is not necessarily the case. For example, a shower with a larger number of particles due to statistical fluctuations will result in a larger shower in both width and length. To optimize background rejection, machine learning techniques can be applied as an alternative to the standard "box cuts". Boosted Decision Tree (BDT) is a machine learning method that trains a set of decision trees (Figure 4–11) that can be used for classification or regression. In the context of gamma-hadron separation, we train classification decision trees with two classifications: gamma-ray shower (signal) and hadronic

shower (background). The performance of a single tree is unstable and prone to statistical fluctuations. To stabilize the performance, BDT is based on an ensemble of decision trees (collectively called a forest). A weighted average is applied to the classification result of the trees; the final output of BDT is a value between -1 and 1 with value closer to 1 to be more "signal" like and vice versa. With BDTs, instead of applying multiple cuts on different variables, one can then apply a single cut to the BDT output to select more "signal" like events (see an example in Figure 4–12). BDT-based event selection is implemented in both `VEGAS` and `EventDisplay` and has been shown to enhance the sensitivity up to 25% compared to standard box cuts [43, 44].

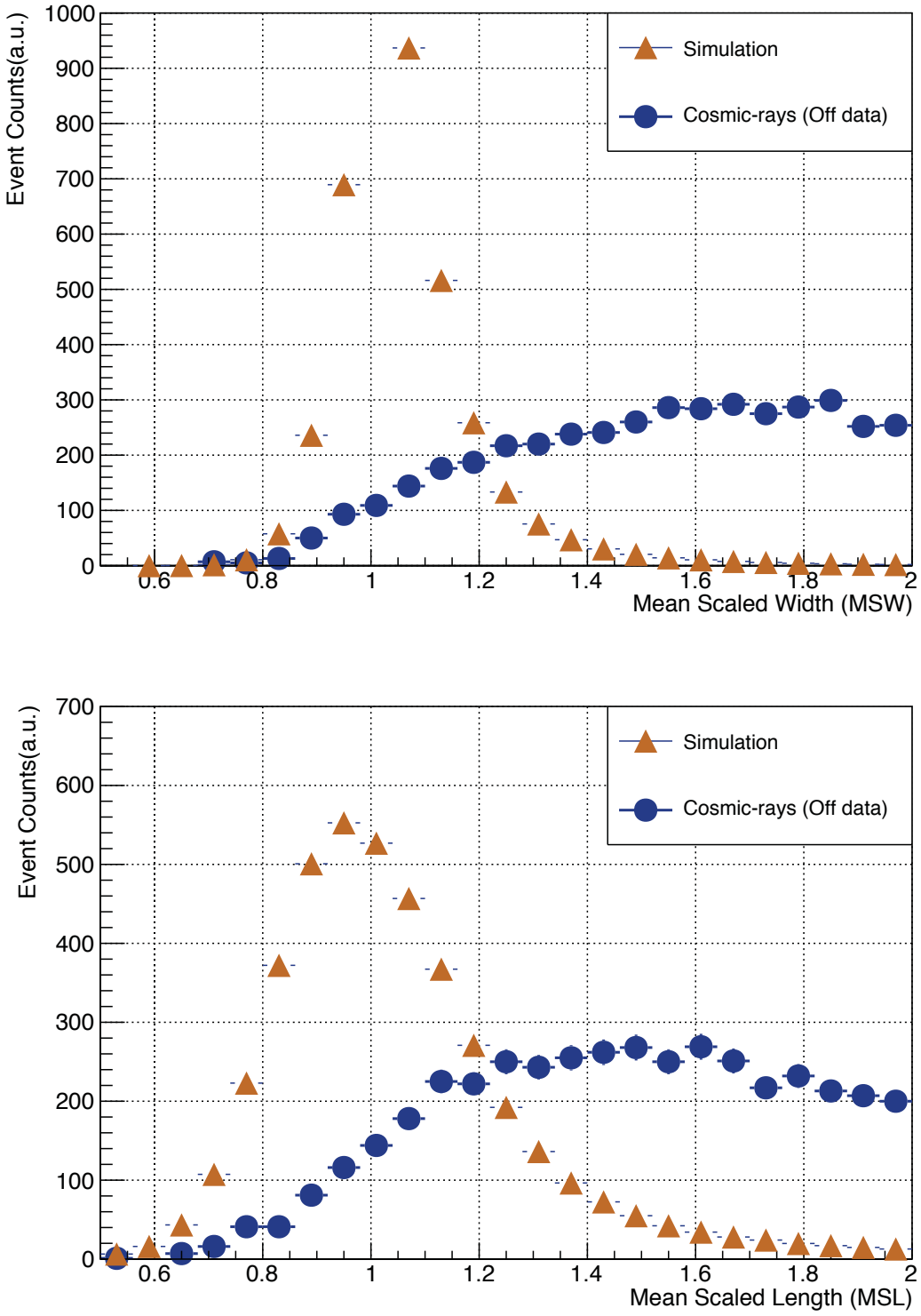

Figure 4–10: Mean scaled width/length distribution for simulated gamma-ray showers and cosmic-ray showers (obtained from data taken from regions with no gamma-ray sources (off regions).). (Top): Mean scaled width. (Bottom): Mean scaled length.

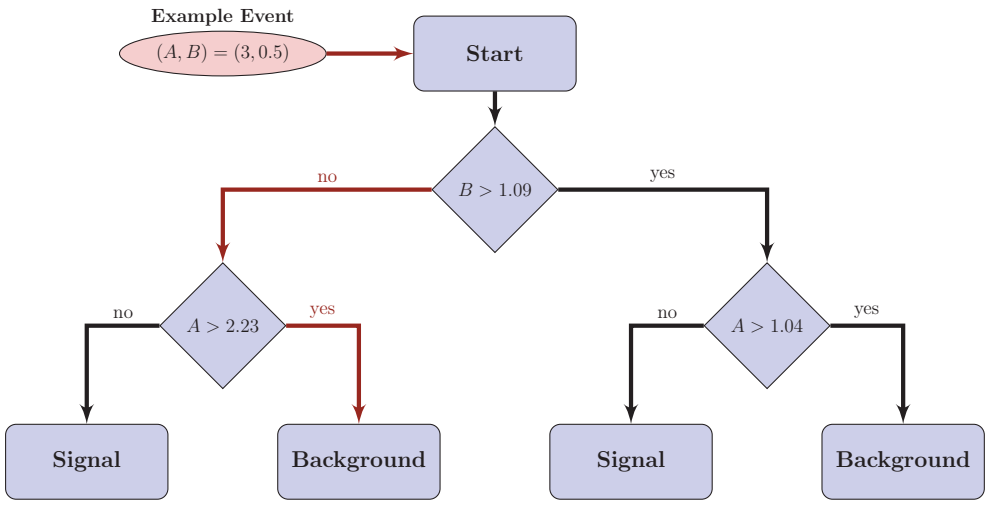

Figure 4–11: Example of a single decision tree. Here, an event has two variables: A and B. An event starts from the top and traverses the tree until the bottom is reached. The path it takes is determined at each node, where a simple cut is applied to one of the two variables. As an example, the route an event with $(A, B) = (3, 0.5)$ takes when traveling down the tree is marked in red. This example event is classified as background by this decision tree.

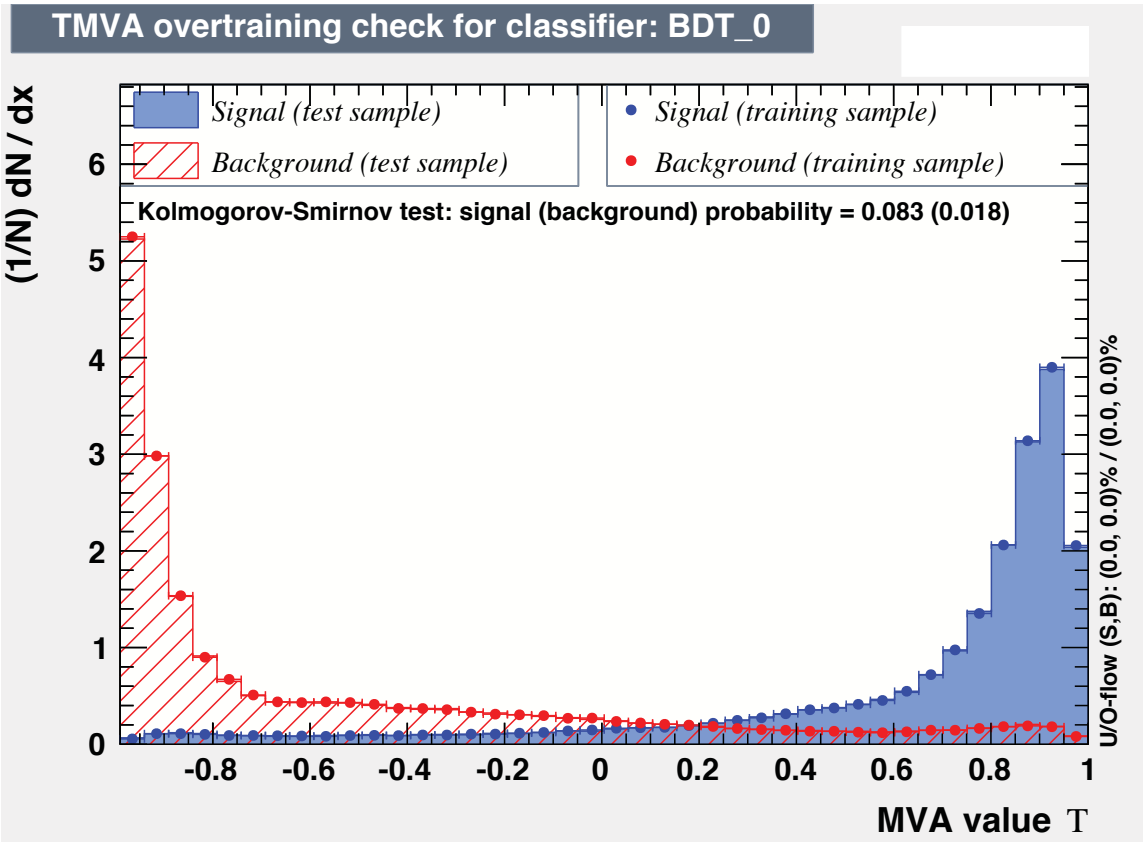

Figure 4–12: Example BDT response to gamma-ray events and cosmic-ray events. The histograms are BDT responses for a test set (i.e. not used for optimizing BDTs) and the points are responses of events used for training. The good agreement between the training samples and test samples implies that there is no over training here. Image credit: Elisa Pueschel.

4.4 High Level Analysis

After the characterization of event properties and gamma-hadron separation, the data is reduced down to a list of gamma-ray like events and their direction and energy. The next step of the analysis is to find potential gamma-ray sources and reconstruct their properties based on the list of selected events. While the gamma-hadron cut is good at selecting gamma-ray events, there are still irreducible backgrounds left. These events could be hadronic showers that look like gamma-ray showers (e.g. gamma-ray sub shower due to early π^0 decay) or other leptonic induced showers (cosmic ray electron/positrons). To identify potential sources a background estimation and subtraction technique is required. As an example Figure 4–13 shows a sky map of selected events from two Crab nebula runs. We can make several observations. Firstly, we note the concentration of events coming from the Crab, which signifies it as a gamma-ray source. Secondly, the sparser event density towards the edge of the field of view, which means that the acceptance has a dependency on the distance from the centre of the Field of View (FoV).

4.4.1 The θ^2 parameter

Now is a good point to introduce the parameter θ^2; θ is the angle between the reconstructed event direction and the direction of a candidate source. For a point-like gamma-ray source, the real[2] gamma-ray events will be concentrated at the location of the source (with spread due to the direction reconstruction resolution; also called gamma-ray point spread function) which means the θ^2 distribution[3]

[2] as opposed to a cosmic-ray-initiated shower that appears to look like a gamma-ray shower

[3] The reason to use the square of θ is to account for the larger phase space further away from the candidate source.

will have a peak at 0 on top of a broad distribution due to background events (see Figure 4–14). By applying a cut on θ, we can enhance the signal-to-noise ratio as well as selecting regions in the sky containing only background.

4.4.2 Background Estimation

The most straightforward method to estimate and subtract background is to select regions in the sky where there is no gamma-ray source (OFF region) and compare with the region containing the potential source (ON region). The size of the ON/OFF regions is defined by θ as mentioned previously. With ON and OFF regions defined, the number of excess events (the number of gamma-ray events sitting on top of background) can be calculated from the number of events in the ON region (N_{on}) and OFF region (N_{off}):

$$N_{excess} = N_{on} - \alpha N_{off} \tag{4.14}$$

where α is the ratio of exposure of the OFF region to ON region. While on paper it looks like a rather simple task, the acceptance variation across the field of view introduces complications as to where the OFF regions should be located.

There are two main methods of selecting the OFF regions: *Reflected Region method*, *Ring Background method*. Both methods are designed so that background estimation and observation of the source can be achieved within the same observing run as opposed to the historical method of dedicated background runs. The *Reflected Region method* relies on the symmetry in acceptance (only strongly depend on distance to the centre of FoV). By strategically pointing the telescope away (often 0.5°) from the target of interest, regions symmetric to the ON region around the centre of camera with the same acceptance are observed simultaneously with the target (right figure of Figure 4–16). This observation strategy is generally referred to as the "Wobble" technique and the pointing offset from the target

source is called the "wobble angle".Under this scheme, the parameter α is the reciprocal of the number of OFF regions.

The *Ring Background method* defines the background region to be a ring around the source position (left figure of Figure 4–16). Different from the reflected region which are selected so that the OFF regions have the same acceptance as the ON regions, the ring background method needs to account for the differences in the acceptance (called *radial acceptance* as it is symmetric in azimuth). A point that is worth noting is that the acceptance discussed here is the acceptance of the background events as opposed to the gamma-ray events. Figure 4–15 shows an example of radial acceptance as a function of angular distance from the centre of the camera. In this scheme, α is then the ratio of the solid angle subtended by the background ring compared to the ON region along with the correction of acceptance.

4.4.3 Detection Criteria

Now that we have the excess and the estimation of background level, the next step is to determine if the gamma-ray signal (if any) is statistically significant. The standard calculation of significance in VHE gamma-ray astronomy is based on a log-likelihood test of the null hypothesis where all the N_{on} and N_{off} are background events:

$$|\sigma| = \sqrt{2}\left[N_{on}\ln\left(\frac{1+\alpha}{\alpha}\cdot\frac{N_{on}}{N_{on}+N_{off}}\right) + N_{off}\left((1+\alpha)\cdot\frac{N_{off}}{N_{on}+N_{off}}\right)\right]^{1/2} \quad (4.15)$$

This is derived by Li and Ma [46] in 1983. The sign of the significance is decided by the sign of excess $N_{on} - \alpha N_{off}$. Typically, the source is considered significant if $\sigma \geq 5$ (commonly denoted as 5σ).

4.4.4 Instrument Response Characterization

To convert the instrument-specific values to physically meaningful results, a set of functions characterizing the response of the instrument are needed.

Instrument Response Functions (IRFs) are the responses of the telescopes to showers of known physical properties (e.g. direction, energy, primary particle ... etc.); in general, the IRFs are calculated from Monte-Carlo simulations. We will describe the simulation process in more detail in Section 4.6. For VERITAS analysis, there are three main IRFs:

- Lookup Tables (LUT): Tables tabulating the expected shower width, length, and energy given observation conditions and image properties. These tables are required for obtaining the mean (reduced) scale variables and the reconstruction of energy. See Figure 4–9.
- Effective Area (EA): The effective collection area of gamma-ray events; it is calculated using simulated gamma-ray events and looking at the ratio of the number of events that pass all the analysis cuts to the number of events that was originally created. Effective area can be thought of as the efficiency of the instrument and analysis chain in detecting a gamma ray times the collection area of the instrument. So, it is very sensitive to the observing conditions (zenith angle, wobble directions ... etc) and the analysis cuts (e.g. gamma-hadron cut, θ^2 cut) that are applied. This is used to convert from number of excess events at a given energy to physical flux. An example of effective area can be found in figure 4–17.
- Radial Acceptance: Discussed in Section 4.4.2. The efficiency of selecting background events as a function of distance away from the centre of the camera. It is used in the ring background method. This is the only IRF that does not rely on simulations; it is estimated directly from data after excluding regions of potential sources.

4.4.5 Flux Measurement

The calculation of the differential energy spectrum of a source relies on the effective area. As mentioned earlier, effective area is the effective collection area

for a point-like gamma-ray source. It can be calculated by analyzing simulated gamma-ray events thrown uniformly on an area (A_{thrown}, normally a circle of radius $r = 750$m) on the ground and looking at the number of events that pass both the hardware trigger and software selection. At a given energy, the effective area is then calculated as follows:

$$A_{eff}(E) = \frac{N_{pass}(E)}{N_{generated}(E)} \times A_{thrown} \tag{4.16}$$

where $N_{pass}(E)$, $N_{generated}(E)$ are the number of simulated events that pass the analyses cut and the number of events that were generated at energy E, respectively. It is straightforward from the definition above to see the relation between the number of excess events and the flux. The two can be connected through the effective area:

$$A_{eff}(E) \times T_{obs}\frac{dF(E)}{dE} = \frac{N_{excess}(E)}{dE} \Rightarrow \frac{dF(E)}{dE} = \frac{N_{excess}(E)}{A_{eff}(E)T_{obs}dE} \tag{4.17}$$

Here, $F(E)$ is the flux of the source, T_{obs} is the dead-time corrected observation time and dE is the width of energy binning. Generally, most analysis requires combining data of different observing conditions (zenith angle, azimuth) which means different effective areas. The computation is then extended as follows:

$$\sum_i A^i_{eff}(E) \times T^i_{obs}\frac{dF(E)}{dE} = \frac{N_{excess}(E)}{dE} \Rightarrow \frac{dF(E)}{dE} = \frac{\sum N^i_{excess}(E)}{\sum A^i_{eff}(E)T^i_{obs}dE} \tag{4.18}$$

where i is the index for the number of observation runs used.

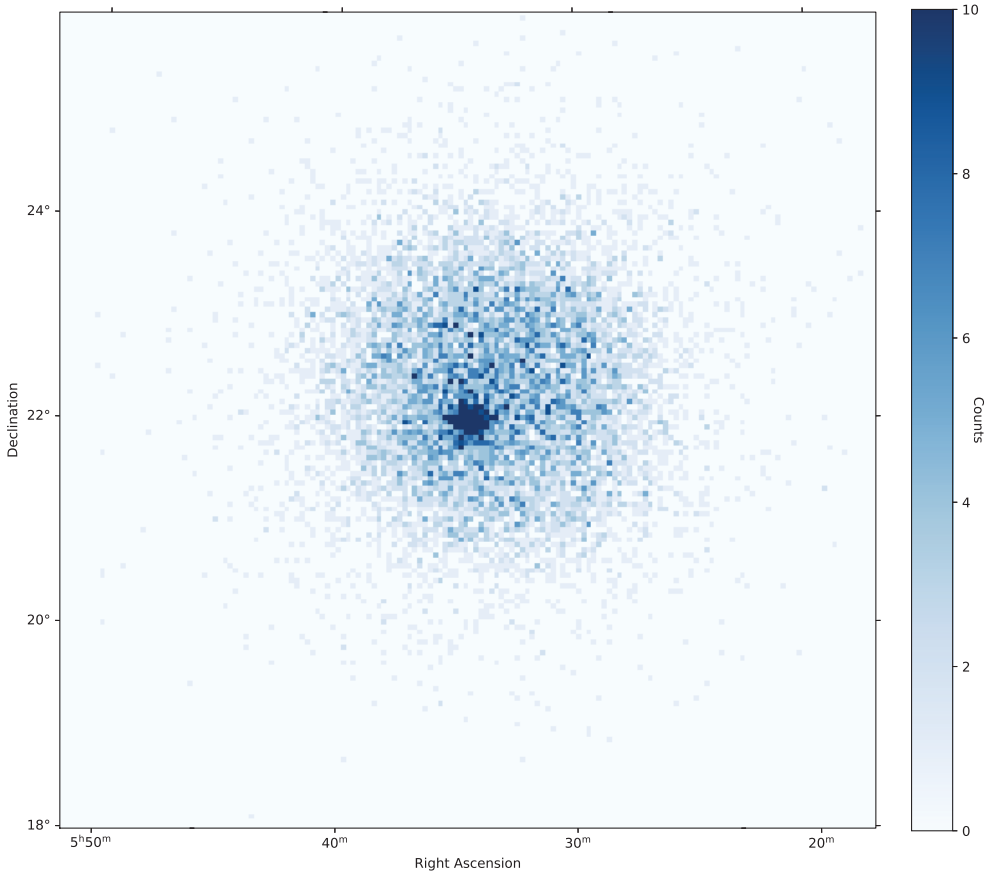

Figure 4–13: Event counts map after gamma-hadron cut using an hour of Crab data. The centre of the figure is the location of the Crab nebula. The asymmetry in the background events around the source is due to observing with a wobble angle.

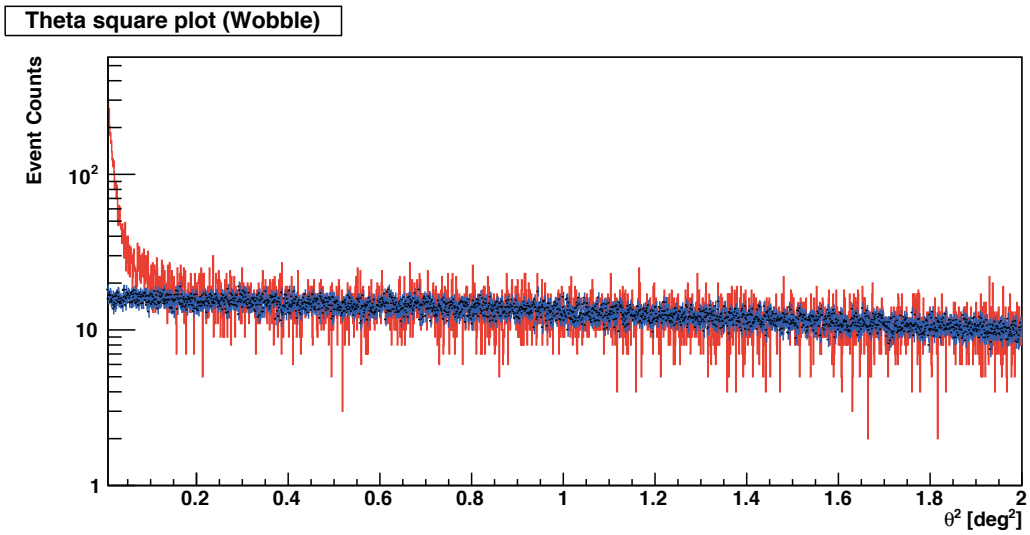

Figure 4–14: Example of θ^2 distributions; the red points include the source (Crab nebula) and the blue points are the distribution after removing the region of the source. The excess at θ=0 comes from the gamma rays emitted by the Crab nebula.

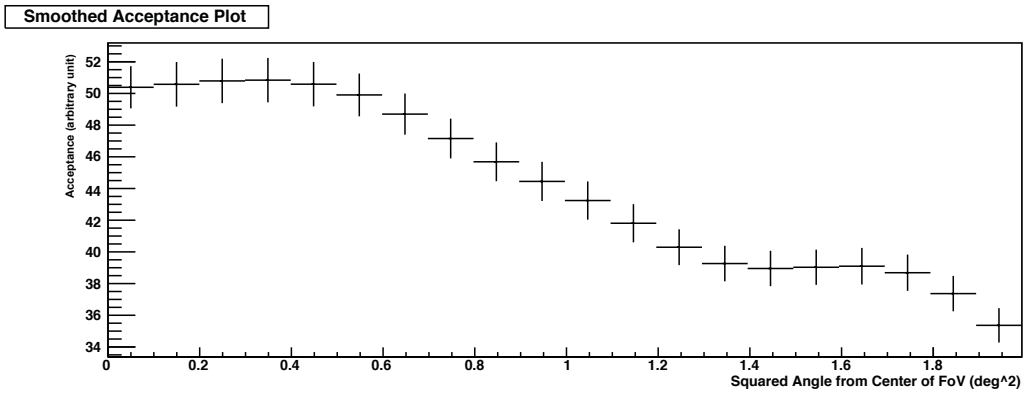

Figure 4–15: Example of radial acceptance.

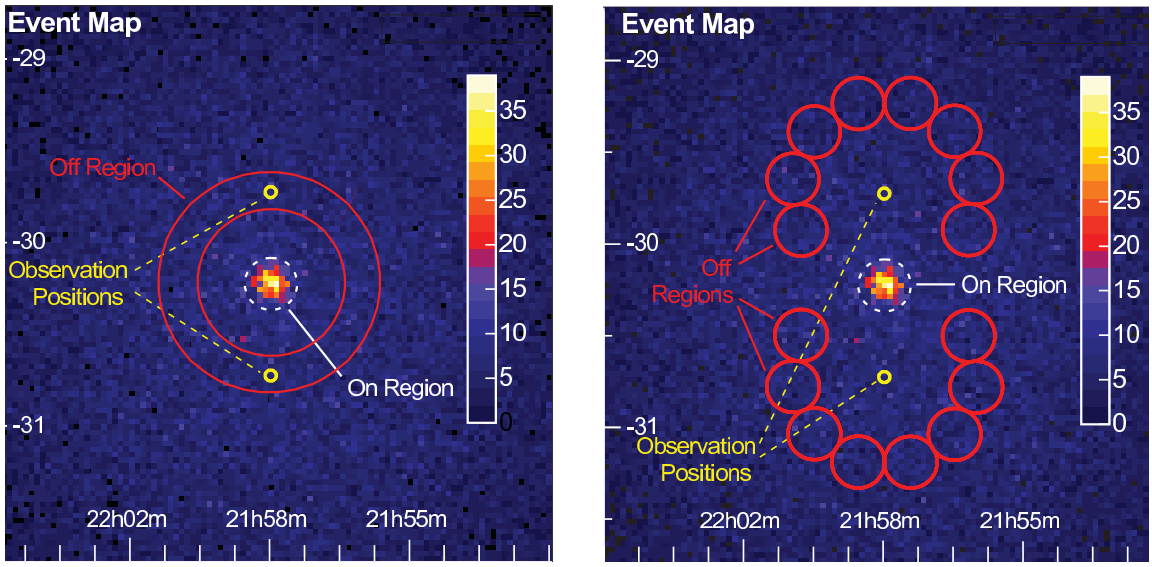

Figure 4–16: Counts map of 5 hours of H.E.S.S. observations of the active galaxy PKS 2155-304. The data was taken with a wobble of $\pm 0.5°$ in declination. (Left): *Ring background method*. (Righ)t: *Reflect region method*. Image credit: Figure 4 from [45].

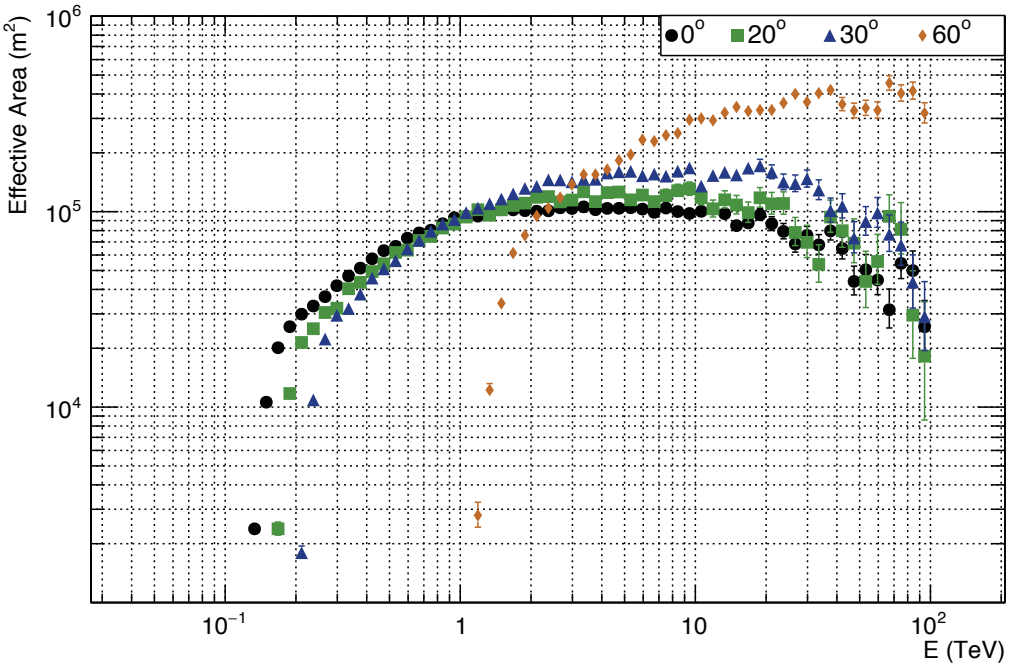

Figure 4–17: Examples of effective area at four different zenith angles. At small zenith angle (large elevation), the difference in effective area is small. However, at larger zenith angle the acceptance of low energy showers falls off rapidly. This is due to the combination of a larger extinction of Cherenkov light and the larger region on the ground where a Cherenkov light pool spans. The two factors combined means that the lower energy showers no longer have enough photons reaching the telescopes to trigger the array. On the other hand, for showers with energy above 1 TeV the effective area is significantly larger (due to the larger light pool projected on the ground). This behaviour can be exploited for observations of targets where the high energy fluxes are of interests (a recent example can be found in [47]).

4.5 *VERITAS* Data Analysis Software

The two packages, `VEGAS` and `EvnetDisplay`, were developed independently by different members of the collaboration and are used to cross validate analysis result prior to publications. While they are developed independently, both analysis packages follows the steps we outlined in earlier sections. The analysis pipelines are divided into stages. `VEGAS` is more granular with five stages: `vaStage` 1, 2, 4[4] , 5, 6. `EventDisplay` has three stages: `eventdisplay`, `mscw_energy`, `anasum`. The functionalities and comparison between different stages of `VEGAS` and `EventDisplay` are tabulated in Table 4–1

VEGAS	EventDisplay	Required IRF	Description
vaStage1	eventdisplay		Calculation of calibration parameters (e.g. *T0*, pedestal level).
vaStage2			Trace integration and single telescope image analysis.
vaStage4	mscw_energy	Lookup Tables	Stereo event reconstruction. Reconstruct energy, shower core position and direction.
vaStage5	anasum		Application of gamma-hadron cut.
vaStage6		Effective Area	High level analysis. Source detection, spectral analysis and light curve analysis.

Table 4–1: Stages of `VEGAS` and `EventDisplay` analysis and their corresponding functionality.

[4] `vaStage3` existed in the older versions of `VEGAS` but has been deprecated and merged with `vaStage4`.

To produce the work presented in this thesis, we mainly used `VEGAS`. The analysis presented in Chapter 6 is produced using a custom version of `VEGAS v2.5.7` with enhanced height of shower maximum reconstruction.

4.6 Air shower and detector simulation software

To generate the IRFs, the analysis of VERITAS relies heavily on Monte-Carlo simulations. Monte-Carlo simulated events are produced in three steps: simulation of air showers and Cherenkov light, propagation of Cherenkov light through VERITAS' optical elements, simulation of electronic response of PMTs to generate traces.

The simulation of air showers is performed with CORSIKA (Cosmic Ray Simulation for KASCADE). CORSIKA is a Monte-Carlo simulation code written in FORTRAN originally developed for the study of air showers for the KASCADE experiment [48] at Karlsruhe, Germany. CORSIKA models the interactions, decays and propagation of nuclei, hadrons, photons and electrons/positrons in the atmosphere at energies up to 10^{20} eV [49]. The simulated gamma-ray events have energies generated according to a power-law distribution with minimum energy of 30 GeV and a power-law index of 2. The selection of such a spectral shape is a balance between calculation time (computational resources required roughly scale with energy of an event) and coverage of energy. Although CORSIKA can simulate and track all secondary particles in an extensive air shower, in the context of the study for IACT, the only output needed are Cherenkov photons (the standard output of CORSIKA is suppressed); a list of photons entering a sphere centred at each telescope with 7 m radius is recorded and written to a binary output file. The showers are generated at different zenith angles at 10° intervals to be matched with observing conditions. The real properties of the simulated showers (energy, direction, primary type ... etc.) generated by CORSIKA are stored and

passed down the simulation chain so one can study the effectiveness of various reconstruction algorithms as well as producing the IRFs.

Once we have the list of photons, the next step in the simulation process is the simulation of the instrument itself. There are two simulation chains for the detector components: *GrISUDet*, and *GrOptics* with *CARE*. *GrISUDet* is a simulation package that does both the ray-tracing of Cherenkov photons and the generation of the PMT traces. It is an older package that takes a simpler approach to the simulation of PMT traces. The traces are generated based on a simple trace model and the number of photons received on a PMT after propagating the CORSIKA photon through the telescope mirror. There is no detailed electronic response simulated. The NSB noise is added to the output file after the PMT traces are generated; this approach simplifies the steps needed to cover a wide range of observing conditions. A single set of simulations can be used for arbitrary NSB noise levels. The drawback of using this package is that it does not model the inefficiency of the high-low gain switch (i.e. the low gain switch sometime does not trigger even when there is saturation), which causes issues especially for the reconstruction of gamma-rays above 1 TeV in the V6 epoch. The better PMT sensitivity after the upgrade means that the low-gain switch is triggered more often for the same number of photons received. This prompted the employment of the second detector simulation chain: *GrOptics* plus *CARE*.

GrOptics[50] is the ray-tracing program developed for the simulation of the passage of atmospheric Cherenkov photons through telescopes designed for IACT. As *GrOptics* is designed for general studies of IACT, it allows for custom-defined telescope geometries. In the case of simulation for VERITAS, only Davies-Cotton type telescopes are simulated. The geometric parameters of the telescopes are given in the *GrOptics* configuration files. *GrOptics* takes output files generated by CORSIKA as input and loops through every event and propagates Cherenkov

photons through the optical elements of a telescope and generates the position and directions of the photons on the focal plane. During this process, the mechanical structures of the telescopes are also taken into account. CameraAndReadout (*CARE*) [51] is a more elaborate electronic simulation code used to simulate the trigger system and electronics of VERITAS. It address the drawbacks of *GrISUDet*. *CARE* takes the output of *GrOptics* as input and simulates the trigger system and electronics response to build files in the same format as observation data of VERITAS. Due to its more detailed description of the electronic system, *CARE* needs to simulate night sky background (NSB) photons at the time of trace generation (by randomly adding photons at a rate specified in the configuration file). This process means that *CARE* requires a larger storage space for simulation files of various noise levels.

Simulations are generated for the different detector configurations (V4,V5,V6), zenith angle, wobble angle, wobble direction and season of the observation. The season of the observation affects the propagation of air showers due to the difference in air density and transparency to Cherenkov light. For simulation generation we have two standard atmospheric models, one for winter and one for summer. At the time of writing, the standard simulation sets for V4 and V5 are generated with *GrisuDet* and *GrOptics/CARE* for V6.

4.7 Legacy IACT Data in the Age of the Cherenkov Telescope Array

So far, the analysis method and software described are proprietary to the VERITAS collaboration; however, with the increasing requirement of multi-wavelength analysis by the community and the rapid development of Cherenkov Telescope Array (CTA), there is a new need for openly accessible software and a data format that can be used by the wider community. Also, with the rapid development of the next generation IACT instruments, it is becoming more important to be able to make the legacy data products available and supported. For

the current generation of major IACTs (VERITAS, MAGIC and H.E.S.S.), the data analysis and storage standards are largely inherited from particle physics experiments, where the ROOT [52] analysis framework and data format is the foundation. While all three major IACTs build their analysis on this foundation, the analysis software and detailed data structures are proprietary and are not shared across different collaborations. Also, the reliance on ROOT and collaboration specific software make access to these data by experts in other fields of astronomy, where FITS is the standard file format, difficult.

In the late 1970s, with the increasing use of CCDs and the need for cross wavelength data analysis (radio and optical then) the Flexible Image Transport System (FITS) was proposed and formally endorsed by IAU in 1982. In the mid 1990s the NASA Office of Guest Investigator Programs (OGIP) promoted multi-mission standards for the format of FITS data files in high-energy (HE) astrophysics. The standard has been regularly updated to address the diversity of research projects and data production types. FITS has since been the most widely use data format within the astronomy community, from radio to gamma ray . Driven by the effort to open data access for the upcoming CTA~~C~~[TB]TAtarted to push for implementation of a common high level data format based on FITs files for the current generation of gamma-ray instruments. From the perspective of the current generation IACT, adopting a common data format that will be supported under the umbrella of CTA not only ensures usability of legacy data but also allows the researchers within each collaboration to access advanced analysis techniques that are being developed for CTA's analysis pipeline.

The proposed high level data format should fit into the data model proposed for CTA [53], where the data model is separated into six levels (Data level 0 to 5, Table 4–2). Data levels 0 and 1 correspond to the data products of the low level analysis described in the earlier sections; the raw data recorded from cameras and

the calibrated single telescope data are stored using these data levels. Data level 2 corresponds to the intermediate analysis products. This data level is where the event level reconstruction data (energy, direction, probability of being background event) is stored. Up to Data Level 2 (DL2), the processing and definitions of data are very instrument specific and generally would not be made accessible to guest CTA observers. Starting from Data Level 3 (DL3), is what we would consider high level data. DL3 is the basis of data sharing to guest observers. This is the data level where the definition of data format and event information are required to be instrument agnostic and all the information required for scientific analysis is stored. To make the current generation of IACTs' data output compatible with this structure, DL3 is the data level where the common data format should be defined. In this section we will be describing the recent effort at standardizing the DL3 file format and attempts at implementing this standard to the current operating gamma-ray instruments.

Data Level	Description
Level 0	Data from the data acquisition system
Level 1	Calibrated measurements in each camera: photons, arrival times. Also include derived per-telescope parameter.
Level 2	Reconstructed shower parameter (per event, after combining data from multiple telescopes).
Level 3	Set of selected events, along with associated instrument response characterization and technical data needed for science analysis.
Level 4	High level binned data product like spectra, sky maps or light curves.
Level 5	Legacy observatory data, such as survey sky maps or source catalog.

Table 4–2: CTA Data levels (reproduced from [53])

4.7.1 DL3 data format

A first community effort to define a common DL3 data specification for the VHE gamma-ray data is carried out in the "Data formats for gamma-ray

astronomy"[5] forum, an open forum hosted on github with contributions from members of different IACT collaborations and mainly driven by CTA. While it is at the moment a non-official effort, the format described therein has started to be implemented for current instruments (Fermi-LAT, H.E.S.S., VERITAS, MAGIC, FACT) as well as CTA. On the analysis side, prototyping and support for this format has started to be adopted by the prototype CTA science tools `gammapy`[6] and `ctools`[7] . It is expected that CTA will partially adopt these formats (likely with amendments and new components) in the future.

The DL3 level data is composed of two main elements. The first is a list of events that are selected as "gamma-ray like", along with their arrival time, estimated direction ($\mathbf{P}'$) and energy(E'). The second element is the instrument response functions (IRFs). IRFs describe the performance of the detector and the relation between the estimated event property and their true values ($\mathbf{P}$,E). There are three main IRF components:

- Effective area, the effective collection area of an instrument, $A_{eff}(E, \mathbf{P})$.
- Energy dispersion, the probability density function of the estimated energy given a true energy and direction $f_E(E'|E, \mathbf{P})$.
- Point spread function (PSF), the spatial dispersion of the estimated event direction for a point source, $f_{\mathbf{p}}(\mathbf{P}'|E, \mathbf{P})$.

The IRFs vary depending on the event direction $\mathbf{P}$ due to the non-uniformity of the detector response across the field of view; this is generally expressed as the dependency on the radial offset of the events from the centre of the FoV. Under the current format, there are two types of IRF specifications: full-enclosure IRFs

[5] https://gamma-astro-data-formats.readthedocs.io

[6] https://gammapy.org/

[7] http://cta.irap.omp.eu/ctools/

and point-like IRFs. The full-enclosure IRFs include radial offset dependency. In the case where this dependency is not included, the IRFs are only suited for the analysis of a point-like source at a pre-defined position in the FoV (e.g. 0.5° from centre). The support for point-like IRFs is mainly for easing compatibility with analysis tools of the current generation of IACTs. The current specification does not explicitly mention the required serialization format; however, the majority of the implementations are based on using FITS files.

Within VERITAS we have implemented a python-based export tool, `V2DL3`, compatible with both `EventDisplay` and `VEGAS`. It is currently capable of exporting DL3 files with either point-like or full-enclosure IRFs (under test by the collaboration for consistency).

4.7.2 Joint Crab Analysis: an example

A joint effort by VERITAS, MAGIC, H.E.S.S., and FACT recently has resulted in the first joint analysis using an implementation of DL3 files and `gammapy` by each collaboration [1]. The analysis included data samples from Fermi-LAT and the four IACTs. The IACT DL3 files are released in files containing runs with observation time of typically 20-30 minutes, in accordance with the observation mode. The IACT DL3 datasets were produced with proprietary code of each collaboration that generated the event list and the IRFs; saved in the specified format. A summary of the datasets can be found in Table 4–3 and Figure 4–18. The VERITAS datasets released contained 40 minutes of archival observations of the Crab nebula taken in 2011, during the V5 epoch. We released IRFs that conform to the point-like IRF format that is valid for the analysis of point-like sources taken at the standard offset angle. The low-level, intermediate-level analysis is carried out using *VEGAS*.

The extraction of the spectrum ($\frac{d\phi}{dE}(E;\mathbf{V})$ where $\mathbf{V}$ is the set of spectral parameters) for the analysis is carried out using the open-source analysis prototype

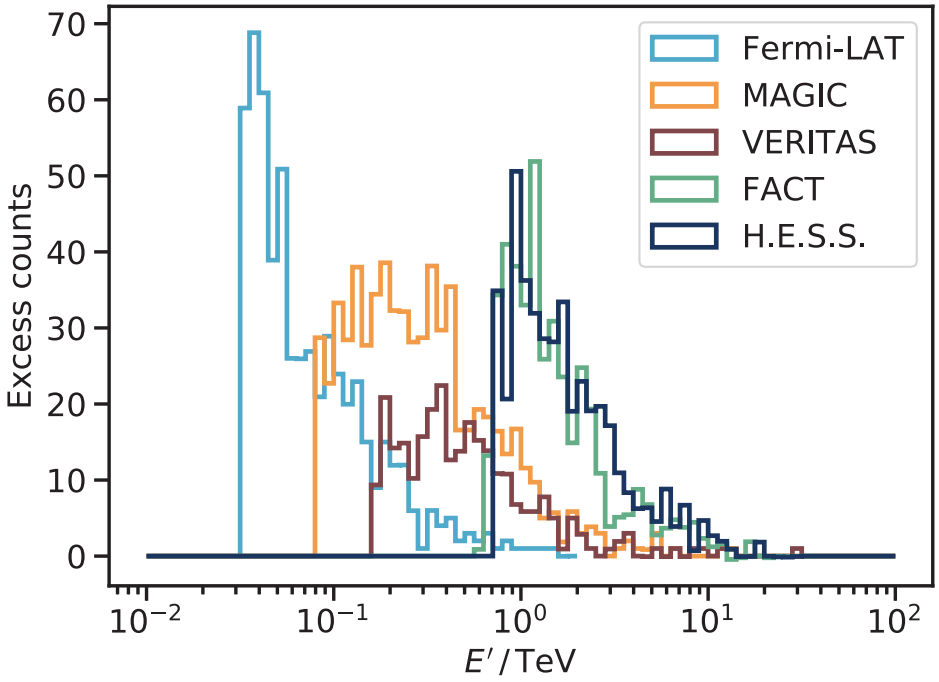

Figure 4–18: Histogram of the estimated mean number of excess events from the Crab nebula versus estimated energy for each dataset. Image Credit: [1].

`gammapy`. A binned maximum likelihood method was applied for the spectral analysis. For n_{runs} observation runs from n_{instr} instruments we can write the likelihood as:

$$L(\mathbf{V}|\mathbf{D}) = \Pi_i^{n_{intr}} L_i(\mathbf{V}|\{N_{on,ijk}, N_{off,ijk}\}_{j=1...n_{runs};k=1...n_{E'}}) \tag{4.19}$$

where $n_{E'}$ is the number of bins considered in the estimated energy space and $\mathbf{D}$ is the data set; the indices i, j, k loop over the number of instruments, the data runs for each instrument, and the list of events, respectively. The calculation of likelihood for each instrument is based on the estimated excess in each energy bin which is obtained using a forward folding technique (convolving the target spectrum with the effective area and energy dispersion of the instrument). The results of the spectral analysis are shown in Figure 4–19.

Instrument	T_{obs}	$E_{min}(TeV)$	$E_{max}(TeV)$
Fermi-LAT	$\sim$ 7 yr	0.03	2
MAGIC	0.66 h	0.08	30
VERITAS	0.67 h	0.16	30
FACT	10.33 h	0.45	30
H.E.S.S.	1.87 h	0.71	30

Table 4–3: Crab nebula datasets summary.

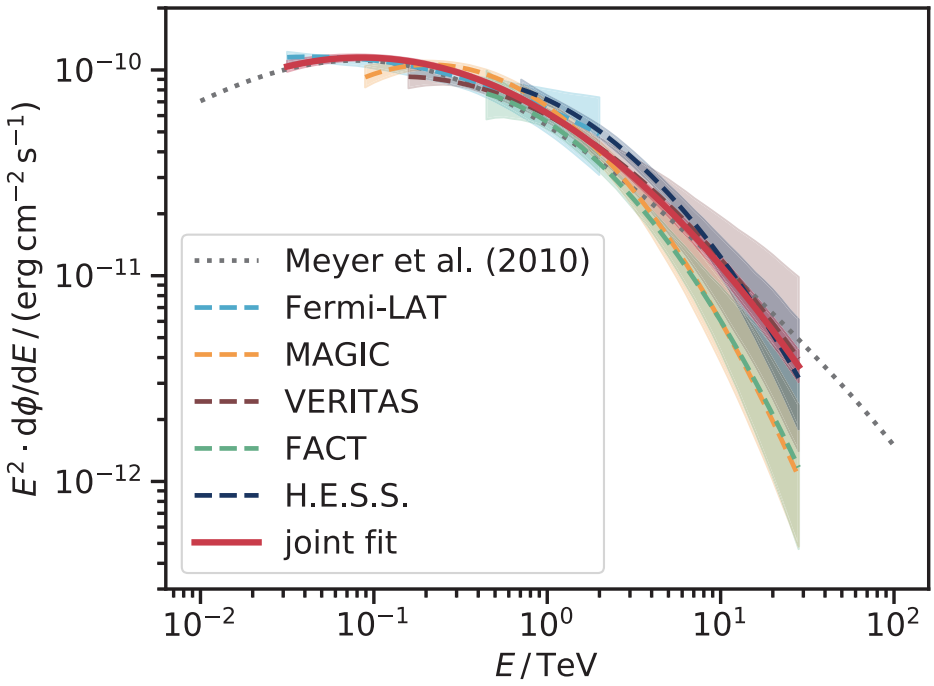

Figure 4–19: Crab nebula spectral energy density (SED) for fits on individual instrument and joint analysis. Image Credit: [1].

This analysis represents the first openly reproducible multi-instrument gamma-ray analysis using the common DL3 format and an open source analysis package. The datasets and analysis code are publicly available through the GitHub repository[8] along with a Docker container[9] on DockerHub. This is the first public

[8] https://github.com/open-gamma-ray-astro/joint-crab

[9] https://hub.docker.com/r/gammapy/joint-crab

joint release of data from IACTs and provides the astronomical community the opportunity to access VHE analysis prior to first-light of CTA.

5

The Quest for Quantum Gravity and Lorentz Invariance Violation

5.1 Introduction

Our current understanding of Nature is based on two disjointed pieces: "Quantum Mechanics" and "General Relativity". Quantum mechanics is extraordinarily successful at describing three of the four fundamental interactions (Electromagnetic, Weak and Strong interactions) under the framework of the Standard Model (SM) using Quantum Field Theory (QFT). This theory neglects the gravitational force and is formulated on a flat spacetime. On the other hand, the description of gravity is based on General Relativity (GR). GR is a classical-mechanics theory that does not consider any quantum property of particles. The experimental (or observational) verifications of GR are on systems where only the gravitational interaction is important (such as astronomical objects). In this limit, the objects (planets, stars ... etc.) are composed of large numbers of fundamental particles which revert the dynamics of the object to the classical limits. Similarly, the experimental verifications of quantum mechanics are done in an environment where a local Minkowskian approximation to space time is accurate and gravitational effects can be neglected. However, it is expected that there exists a scale where the interplay between quantum mechanics and gravity cannot be

ignored and a unified theory is necessary. This scale is given by the Planck mass m_p, Planck energy E_p, and Planck length l_p[54]:

$$\begin{cases} m_p = \sqrt{\frac{\hbar c}{G}} \approx 2.18 \times 10^{-8} \text{ kg} \\ E_p = m_p c^2 \approx 1.22 \times 10^{19} \text{ GeV} \\ l_p = \sqrt{\frac{\hbar c}{G}} \approx 1.6 \times 10^{-35} \text{ m} \end{cases} \tag{5.1}$$

where c is the speed of light, G is the gravitational constant, and $\hbar$ is the reduced Planck constant. There are many arguments pointing to the Planck scale (or the vicinity) as the characteristic scale of quantum-gravity effects. The most common argument comes from the extrapolation of the currently known strength of the coupling constants of the four fundamental interactions; it is shown that there will be a unification of the strength of these couplings at an energy close to the Planck energy [55].

While there are a plethora of approaches to formally combine GR and quantum mechanics to form a quantum gravity (QG) theory, the high characteristic energy scale limits the experimental verification or rejection of these theories in a controlled lab environment such as an accelerator experiment. Observations of astrophysical sources therefore emerge as a promising alternative to indirectly constrain some QG theories. The formalisms that are considered as potential solutions to the quantum-gravity problem are complex and their physical implications sometimes not well understood; an exhaustive test of all the theories is not practical. So, the reasonable approach is to compare data to a "test model" that is inspired by common features of some quantum gravity theories that are understood. Lorentz invariance violation (LIV) is one such feature; LIV can be introduced through the modification to the dispersion relation of particles.

In this chapter, we will first introduce the motivation for establishing a QG theory. A brief description of some theoretical approaches to the quantum-gravity problem will follow. We will then discuss some phenomenological effects that arise

from LIV through a modified dispersion relation that can be tested using VHE gamma-ray telescopes. Finally, the constraints on the LIV energy scale from the literature will be summarized.

5.2 Current Theories

5.2.1 General Relativity

General relativity is the theory of the gravitational interaction; it describes the interaction as a deformation of the space-time geometry due to the presence of mass and energy. GR was developed by Albert Einstein and first published in 1915. It provided resolutions to several observations that cannot be explained by Newtonian gravity such as the anomaly in the orbit of Mercury [56]. It also provided novel predictions. For example, in his paper published in 1915 [57], Einstein calculated the bending of light due to gravity, which has a deviation angle twice as large as expected from Newtonian gravity. This prediction was verified by a British expedition led by Sir Arthur Eddington observing the May 1919 solar eclipse [58], the first observational confirmation of GR. Einstein also predicted the existence of gravitational radiation. Gravitational waves are ripples in space-time coming from heavy objects accelerating and generating disturbances in the gravitation field. These distortions in space-time structure can have effects that are detectable (although minuscule) when they reach Earth. In 1974, through the observation of the binary pulsar PSR J1913+16 [59, 60, 61], the existence of gravitational waves was demonstrated indirectly (Figure 5–1). It was not until 2015, with the LIGO detector , that dints of gravitational waves from black hole merger event were made [62].

Through the 20th century, GR has proven to be extraordinarily successful in describing observations of the macroscopic universe; however, it is not without limitations. There are scenarios that exists in the universe where knowledge of GR is likely to be not applicable. Some of the issues are related to black holes. In the

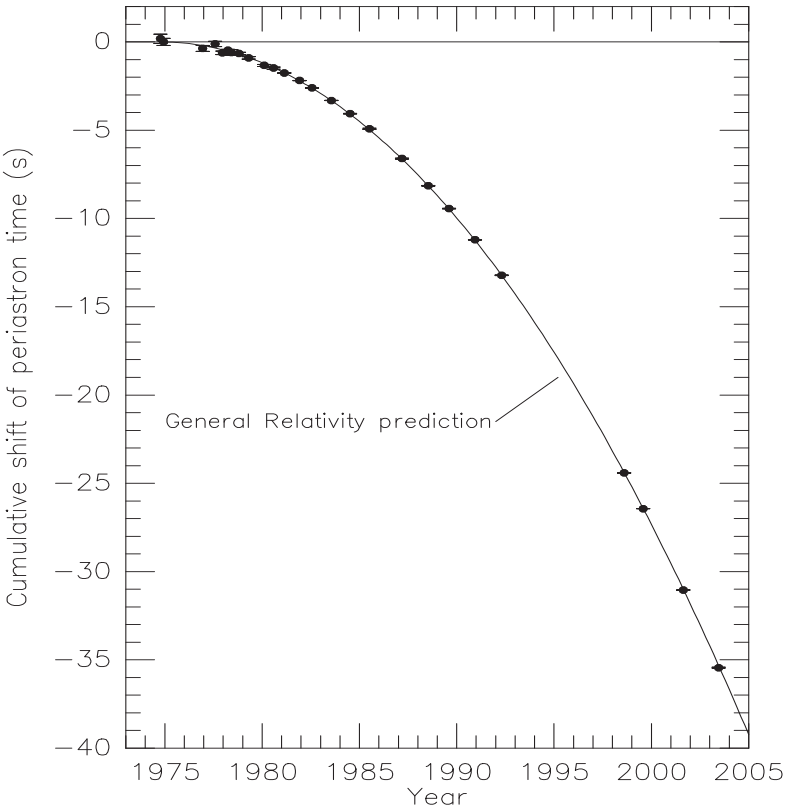

Figure 5–1: Orbital decay of PSR J1913+16. If gravitational radiation exists the energy of the system would be radiated away and modify the orbit. The data points are the changes in the epoch periastron and the parabola shows the general relativity prediction of the orbital decay due to gravitational radiation. Image credit: Figure 1 of [63].

GR description of black holes, the centres of the black holes have infinite density (i.e. a singularity) which implies that GR is insufficient at describing the physics inside the event-horizon of a black hole. Also, if one assumes (which has yet to be experimentally proven) the existence of Hawking radiation [64], black holes radiate particles from the event-horizon and lose mass. This means that there exists a stage in a black hole's evolution when the event-horizon reaches the size of the Planck length; at this stage we are left without any approximate answer to the dynamics of further development. Another case that requires physics beyond GR arises from cosmology: under the current Big Bang cosmology paradigm, there

would exists a time horizon before which the energy/matter density is beyond the Planck scale. A combination of GR and quantum mechanics is necessary to understand this region.

5.2.2 Quantum Field Theory

Quantum field theory (QFT) is a theory merging quantum mechanics and special relativity; QFT has led to successful development of Quantum Electro-Dynamics, describing the electro-magnetic and weak interactions, and Quantum Chromodynamics, describing the strong interaction. Along with all the known fundamental particles (Figure 5–2), these descriptions of the three fundamental interactions form the Standard Model. Over the latter half of the 20th century, QFT and the SM have proven to be powerful at predicting the existence of particles and their physical properties. Some examples worth mentioning are the predictions and discovery of the W boson [65] and the Z boson [66]. Also, the recent first detection of the Higgs boson [67, 68] at the Large Hadron Collider (LHC) finally confirmed the Brout-Englert-Higgs mechanism that provides mass to particles [69, 70]. The discovery was made nearly half a century after the introduction of the idea in 1964.

Despite these successes, the Standard Model is a not a complete description of nature. QFT is developed with the assumption of flat space-time and ignores gravity, so the scenarios discussed earlier for GR also present issues to QFT. While there are approximate descriptions of quantum systems under strong gravitational fields (such as the derivation of Hawking radiation), there is no success at energy/density scales beyond the Planck scale. Apart from the quantum gravity problem we have been discussing, the Standard Model is incomplete even without invoking gravity. One issue is the description of neutrinos; in the Standard Model, neutrinos have only left-handed helicity which prevents them from interacting with the Higgs boson to acquire mass. However, experimental

evidence of non-zero neutrino mass emerged in the 1970s through the measurement of the neutrino flux from the Sun (by experiments such as the Homestake Solar Neutrino Detector and the Kamiokande experiment [71, 72]). They reported a deficit in the neutrino (specifically the electron neutrino) flux compared to a calculation of the solar ^{8}B and ^{7}Be nuclear reactions. While the deficit of neutrinos obtained by earlier experiments could be explained by the oscillations of neutrinos between three different flavours, it was not until the results obtained by the Sudbury Neutrino Observatory (SNO) in 2001 [73], which is sensitive to all three neutrino flavours, that the existence of neutrino oscillations was confirmed. The existence of oscillations requires neutrinos to have non-zero mass [74]. Extra mechanisms are required in the SM to introduce mass to neutrinos [75].

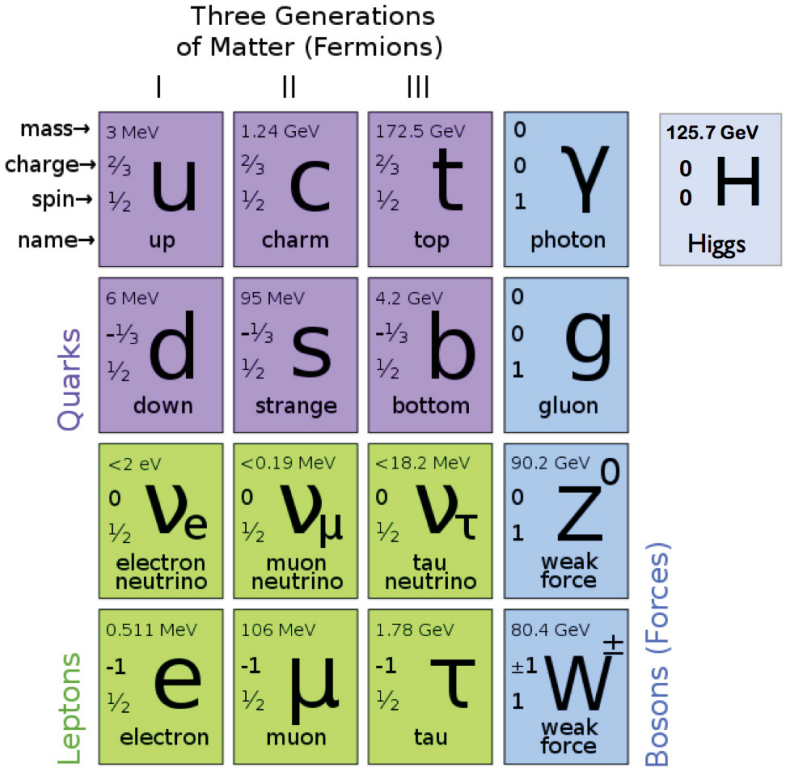

Figure 5–2: Elementary particles of the Standard Model. From [76].

5.3 Theoretical Approaches to Quantum Gravity

In the last section, we discussed some of the limitations and issues of our current understanding of GR and QFT. These issues sparked a need to develop theories beyond QFT and GR. Currently there is no accepted quantum gravity theory; however, several candidate models exist that could potentially lead to a full QG theory in the future. In this section, we will briefly discuss some of these models.

5.3.1 Effective Field Theory

A naive approach to combine QFT and GR is to introduce terms in the Standard Model Lagrangian to represent gravitational interactions. This procedure introduces a massless tensor field corresponding to particles of spin 2 (known as *gravitons*). While this seems at first a straightforward task, further inspection of this form shows that it is problematic; this theory is non-renormalizable due to the dimensionful coupling constant [77] ($\sqrt{G}$ where G is the gravitational constant; unlike the case for electromagnetism which has a dimensionless coupling constant). The divergence for high energy particles that appear in QFT that are normally removed through renormalization would not be removed unless one introduces an infinite number of counter terms in the Lagrangian to remove the infinities. At lower energy, these divergence terms are irrelevant so one can make sense of the phenomenological implications of a quantum gravity theory; however, at higher energy (close to or beyond the Plank scale), this theory would lose its predictive power. Although this approach is not a viable solution to the quantum gravity problem it is still useful from a phenomenological point of view and it is called effective field theory (EFT).

5.3.2 Loop quantum gravity and String Theory

The failure of directly introducing gravity into the framework of QFT means that it requires a more drastic reformulation. Two of the most popular approaches are Loop Quantum Gravity (LQG) and String Theory (ST).

LQG is an attempt at merging QFT and gravity by rewriting QFT in a way that does not rely on a flat space-time (recall that QFT is actually a special relativistic quantum theory). The approach of LQG is to replace representations of fields in a flat space time (i.e. as a function of spatial/temporal coordinates) by representations in terms of Wilson loops (analogous to representations of wave functions in momentum space). This reformulation also applies to GR [77]. This approach puts GR and QFT under the same formalism; a consequence that comes naturally out of this formalism is the quantization of space and time. This formalism results in quantized gravity without the divergence issues of EFT. The quantization of space-time also means that space-time cannot be arbitrarily small which nicely negates the formation of a singularity in Big Bang cosmology. Despite having many nice properties in solving the quantum gravity problem, it has proven difficult to obtain crisp physical predictions. However, attempts can be made from the structure of the theory to infer some candidate LQG effects that have observational consequences. One such effect is the breaking of Lorentz invariance at the Planck scale due to the quantization of space-time [55].

Another more ambitious approach is String Theory. The development of String Theory came out of research into describing strong interactions in the 1960s; although it was disfavoured for Quantum Chromo-Dynamics, it was realized subsequently that the properties of ST made it a promising candidate for the quantum gravity problem. In place of particles, the fundamental building elements of the universe are one dimensional objects called *strings* [78]. The different particles that form the Standard Model are identified as different vibrational modes on

the strings (including gravitons). Similar to LQG, the String Theory description of gravity also removes the issue of divergence that comes with EFT. It also addresses some profound questions in the Standard Model such as the fine-tuning problem (i.e. the requirement of about 20 dimensionless adjustable parameters); in String Theory, there is only a single dimensionful parameter: the length of strings [78]. The most prevalent form of String Theory is superstring theory (i.e. supersymmetric string theory) that includes descriptions for both fermions and bosons (unlike the original version of string theory, which is purely bosonic). A signature of string theory is the requirement for extra dimensions; for string theory to be self consistent the Universe has to exist in a 10 dimensional space for superstring theory; for bosonic strings, it requires 26 dimensions [78]. Similar to LQG, one of the issues in ST is that it is challenging to extract prediction at energies that are accessible to current accelerator experiments.

5.4 Lorentz Invariance Violation Phenomenology

Lorentz invariance violation, although not a general prediction of all QG theories, is a possible observational signature that can be used to verify or reject some classes of QG approaches. As an example, the work done by Colladay and Kostelecký [79], following the approach of EFT, includes gravitational forces in the Standard Model and adds extra terms to the Lagrangian (this approach is named Standard Model Extension (SME)); in such a framework, all possible Lorentz symmetry breaking and CPT breaking terms are introduced. Although it is possible to attempt to observationally verify specific theories, it is more preferable to formulate the question as a more generic model.

5.4.1 Modified Dispersion Relation

To make the experimental investigation model agnostic, the common approach is to represent the modified dispersion relation as a Taylor-expansion of the

standard dispersion relation $E^2 = p^2c^2$ with a characteristic energy scale E_{QG}:

$$E^2 \approx p^2c^2 \left[1 + \sum_{n=1} \epsilon_n \left(\frac{E}{E_{QG}}\right)^n\right] \tag{5.2}$$

where $\epsilon_n \in [-1, 1]$ controls the LIV effect to be either sub-luminal or super-luminal [80, 81].

One thing worth noting is that this representation of LIV is only meant to be a convenience for experimental searches; the parameters ϵ_n and the order of modification n is not a parameter set naturally arising from any specific theory. Some scenarios could be favoured under a theory but not viable in another; for example, under the Standard Model Extension framework the scenario $n = 1$ violates CPT symmetry and is regarded as less favoured than the $n = 2$ case. Also, from calculations from LQG, the linear dispersion has the associated effect of vacuum birefringence (i.e. speed of light in vacuum also depends on polarization) [82], which is highly constrained by the observed high degree of polarization in soft gamma ray observations of GRB 021206 [83]. However, under some String Theory models such as the one proposed by Amelino-Camelia et al. [84], the $n = 1$ scenario is preferred and allowed without an associated birefringence effect.

Observationally, the search for LIV is then performed on signatures of the kinematic and dynamic changes of photons due to the modified dispersion relation. Here, we will describe some major effects that LIV can introduce that could be verified through VHE gamma-ray observations.

5.4.2 Time of Flight Dispersion

From Equation 5.2, for the leading order n dispersion effect, one can derive the speed of the photon as follows:

$$v_\gamma(E) = \frac{\partial E}{\partial p} = \frac{\partial pc\left[1 + \epsilon_n/2\frac{E}{E_{QG}}^n\right]}{\partial p} \approx c \times \left[1 + \epsilon_n \frac{n+1}{2}\frac{E}{E_{QG}}^n\right] \tag{5.3}$$

So, photons of different energy emitted simultaneously from a distance source propagate at different speeds and will arrive at an observer at different times. For the case where $\epsilon_n = -1$, high energy photons are moving at a lower velocity than low energy photons; this scenario is referred to as the sub-luminal LIV, and $\epsilon_n = 1$ is referred to as the super-luminal scenario. As we mentioned earlier, this expansion is merely a phenomenological description to provide model independent approaches to observational or experimental searches; the class of theory that can lead to sub-luminal and super-luminal (as well as $n = 1$ and $n = 2$) LIV effects is generally different and often not directly comparable [55].

The quantum energy scale E_{QG} is expected to be close to the Plank energy scale ($\sim 10^{19}$ GeV, which means a $10^{-18} \times c$ difference in speed for a 1 GeV photon with $n = 1$), so it is difficult to perform terrestrial experiments to search for such an effect. To produce detectable speed differences from time delay, one needs to produce photons at high enough energy and detect them over a long distance; neither of the criteria can be met in a lab. A viable solution is to turn to high energy gamma ray sources (blazars, gamma-ray pulsars... etc.). Not only are these sources the most energetic accelerators known to mankind, but many of them are also extremely distant; that makes them ideal for the searches of time-of-flight dispersion LIV effect.

For a galactic source that is at a distance D away, the arrival time dispersion of photons of energy E_{low} and E_{high} emitted simultaneously by the source can be simply expressed as:

$$t(E_{high}) - t(E_{low}) = -\epsilon_n \frac{n+1}{2} \times \frac{D}{c} \times \frac{E_{high}^n - E_{low}^2}{E_{QG}^n} \tag{5.4}$$

On the other hand, for extra-galactic sources, the effect of the expansion of the Universe needs to be taken into account. The calculation above assume photons of two energies are traveling through the same distance, which does not apply if

the Universe is expanding. For a source at redshift z, Jacob and Piran [85] have derived the time delay between the two photons:

$$t(E_{high}) - t(E_{low}) = -\epsilon_n \frac{1+n}{2H_0} \frac{E_{high}^n - E_{low}^n}{E_{QG}^n} \int_0^z \frac{(1+z')^n}{\sqrt{\Omega_m(1+z')^3 + \Omega_\Lambda}} dz' \qquad (5.5)$$

where Ω_m, Ω_Λ, and H_0 are parameters in the ΛCDM (Lambda - Cold Dark Matter) cosmological model. Ω_Λ and Ω_m are the dark matter and regular matter density, respectively. H_0 is the Hubble constant. The values of these parameters can be found in the latest Plank mission results [86]. Figure 5–3 shows the arrival time differences due to LIV at $E_{QG} = E_p$ for the linear case and $E_{QG} = 10^{-8} E_{planck}$ (chosen to match the order of magnitude from the best quadratic limits obtained through time-of-flight analysis).

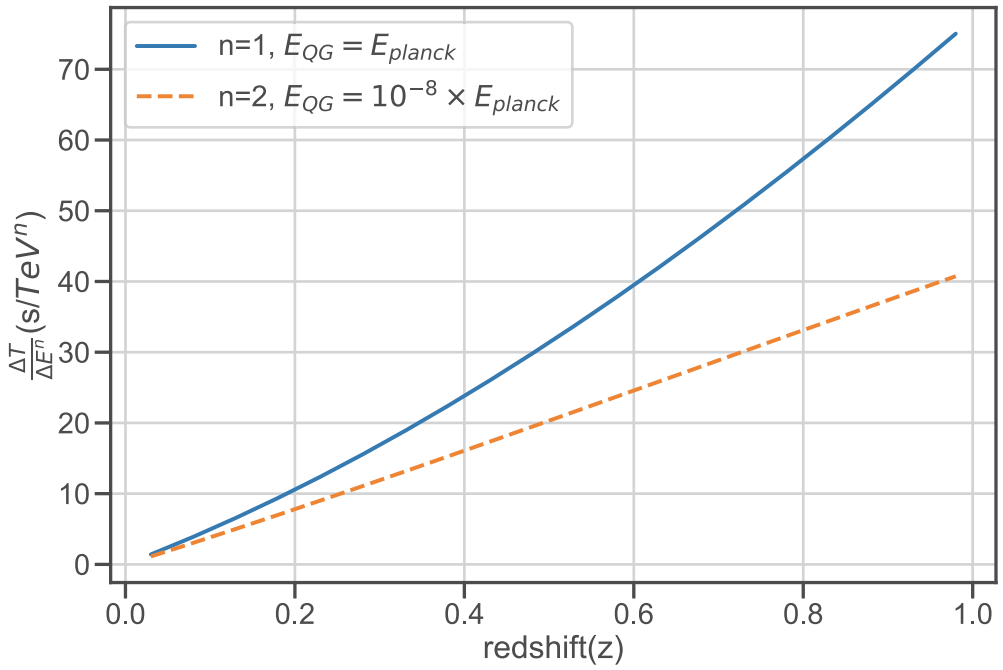

Figure 5–3: Time delay due to linear and quadratic LIV, calculated using Equation 5.5.

5.4.3 Modified Pair-Production Interaction Threshold

The modified dispersion relation not only affects the propagation of photons, it can also change photon interactions with other particles. For extra-galactic gamma-ray sources, TeV gamma rays can be absorbed during propagation due to interaction with the Extra-galactic Background Light (EBL). EBL is the optical/UV light coming from all the galaxies in the Universe throughout cosmological evolution. The main channel of the interaction between gamma rays and EBL photons is through the $\gamma\gamma$ pair production [87]:

$$\gamma + \gamma \rightarrow e^+ + e^- \tag{5.6}$$

From simple kinematic arguments, we can see that for this process to be kinematically viable, for a gamma ray with energy E, the EBL photon needs to have a minimum energy $E_{threshold}$:

$$E_{threshold} = \frac{m_e^2 c^4}{E} \tag{5.7}$$

The kinematic changes due to equation 5.2 can modify the energy threshold. Under the sub-luminal scenario ($\epsilon_n = -1$), the term $\epsilon_n \frac{E}{E_{QG}}^n$ in the modified dispersion relation effectively acts as a negative rest-mass which means that to reach the required energy to produce stationary positron and electron pairs in the centre of mass frame the energy of the EBL photon needs to be higher than what we previously calculated. The threshold energy then becomes[1] :

$$E_{threshold} = \frac{m_e^2 c^4}{E} \times \left[1 + \frac{1 - 2^{-n}}{4} \frac{E^2}{m_e^2 c^4} \left(\frac{E}{E_{QG}}\right)^n\right] \tag{5.8}$$

[1] the term $1-2^{-n}$ should be replaced by 1 if only the photons are affected by LIV [87].

Here, the focus is on the sub-luminal case because the super-luminal scenario would allow for photon decay; the new term acts as a positive rest mass for photons. An investigation of this case would require assumptions of the dynamics of the process, which is a topic we will delay until later. A raised threshold means that for a given gamma ray, the density of EBL that it can interact with is reduced (Figure 5–4). Figure 5–5 shows the optical depth of gamma rays for sources at $z = 0.03$, 0.05 and 0.07 for a LIV of $n = 1$ and E_{QG} at the Planck energy.

Observationally, the signature of the modified pair-production threshold would manifest in the observed spectrum of sources at cosmological distances (e.g. AGNs). As the Universe at moderate redshift starts to be opaque for photons above 1 TeV, there generally exists a spectral cutoff in this regime for these sources. With the above modification, the raised threshold leads to a smaller optical depth for gamma rays at high energy and hence a raised cutoff energy. To constrain such effects, one can look for anomalous spectral upticks of these sources after correction for EBL absorption.

5.4.4 Photon Decay

We mentioned earlier that the modified dispersion relation in effect introduces an energy dependent mass (which could be negative) for the photon. In the case of super-luminal LIV, the effective photon mass becomes positive:

$$m_{\gamma,eff}(E) = \frac{\epsilon_n}{c^2}\frac{E^{n+2}}{E_{QG}^n} \tag{5.9}$$

This opens up reactions that were kinematically forbidden without LIV. From energy conservation we can then derive the threshold energy for the photon for this process to be kinematically viable. At the threshold energy, the resulting electron and positron should have the same energy and should be moving parallel to the direction of the original photon; hence, the energy threshold (E_{th}) can be derived

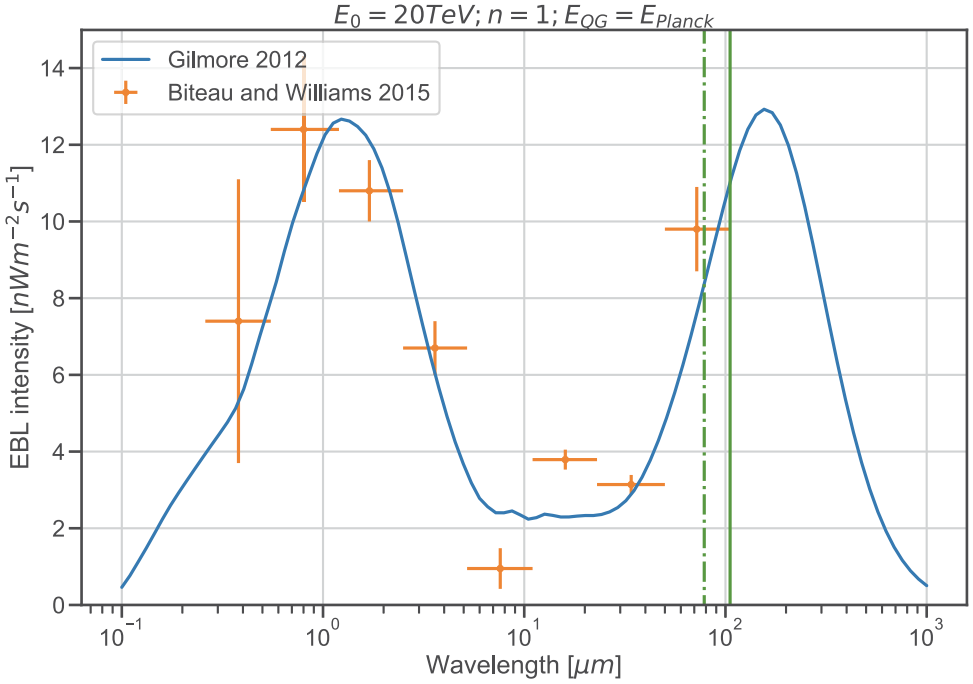

Figure 5–4: Wavelength threshold for EBL photons that are viable to interact through pair production with gamma rays with 20 TeV energy. The vertical solid line is the unmodified threshold. The dashed line is the modified threshold with a linear ($n = 1$) LIV and $E_{QG} = E_{Planck}$. The points overlaid are the measured EBL spectrum at $z = 0$ by Biteau and Williams [87] and the blue line is the EBL model by Gilmore et al. [88].

as follows [89]:

$$p_e c = \frac{1}{2} \frac{E_{th}}{\sqrt{1 + \frac{E_{th}}{E_{QG}}^n}} \tag{5.10}$$

$$E_{th} = 2 \times \sqrt{p_e^2 + m_e^2 c^4} \Rightarrow E_{th} \times \left(\frac{E_{th}^2 - 4m_e^2 c^4}{4m_e^2 c^4} \right)^{1/n} = E_{QG} \tag{5.11}$$

where p_e is the momentum of the outgoing electron and positron, and m_e is the rest mass of the electron[2] . According to the calculation by Martínez-Huerta and Pérez-Lorenzana [89], which applies modified dispersion relations in standard

[2] This derivation assumes that LIV only affects photons but not electrons.

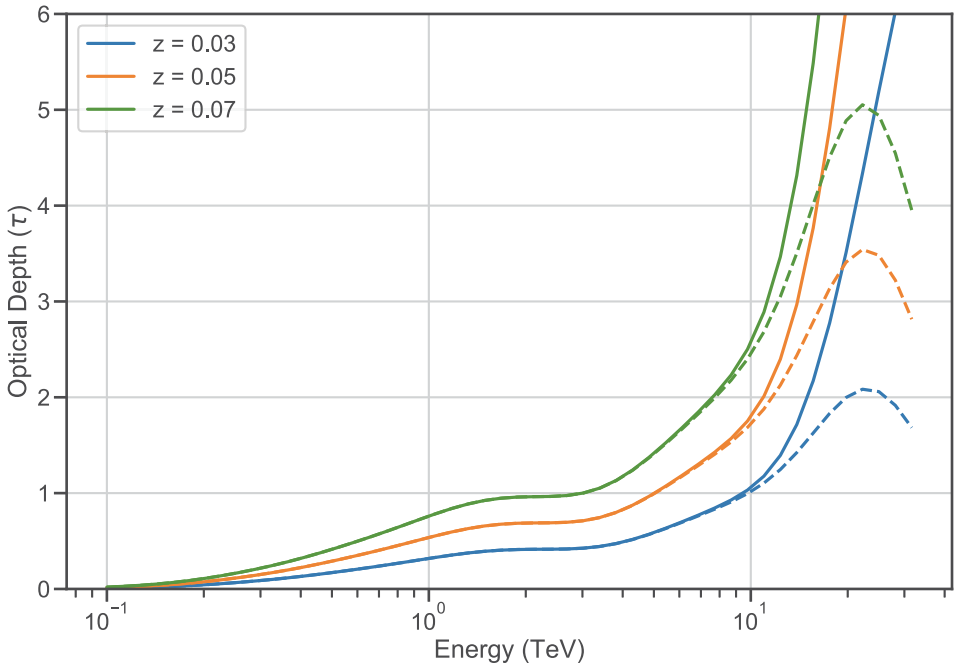

Figure 5–5: EBL optical depth for gamma rays at three redshifts. The x-axis is the energy of the gamma ray at $z = 0$. The solid line is the classical case and the dashed line is the case of linear LIV modification. Image credit: Fig 9 from [87] (reproduced).

QED rules, this decay process is very efficient and would not allow photons to survive traveling through astronomical distances (for example, with $E_{QG} \approx E_{planck}$, 100 TeV photons cannot survive further than $\sim$ 1 m). So, one would not expect detection of any gamma ray above the threshold E_{th}; therefore, one can place limits on E_{QG} by searching for gamma rays at very high energy. For the detection of photons at energy E_γ we can place the limit at:

$$E_{QG} > E_\gamma \left[\frac{E_\gamma^2 - 4m_e^2c^4}{4m_e^2c^4} \right] \tag{5.12}$$

5.4.5 Modified Bethe-Heitler Cross Section

Similar to the case of photon decay, the modified dispersion relation can change the interaction dynamics of the pair production interaction cross section

in the presence of a Coloumb field (the Bethe-Heitler process). However, unlike in the previous cases where the majority of the changes in the process come from kinematic arguments (with the exception of photon decay, although even in this case the threshold is derived through pure kinematic arguments), the modification to the Bethe-Heitler cross section is mainly dynamic. A simple description for how a modified dispersion relation affects the Bethe-Heitler process is given by Vankov and Stanev [90]. The argument is based on the concept of formation length (also called coherence length) of the interaction. Ter-Mikaelian [91] first realized that particle interactions do not take place at a single point but over a long distance (formation length) according to the uncertainty principle. For highly relativistic particles, the momentum transfer between the interacting particle and target nuclei is small and the formation length can be macroscopic. In the case of the Bethe-Heitler process or bremsstrahlung, the macroscopic formation length opens up the interaction to be disrupted by the neighbouring medium and suppresses the interaction probability. This is the physical mechanism of the Landau-Pomeranchuk-Migdal (LPM) effect (for more details see the review by Klein [92]). Analogously, the extra term the modified dispersion relation introduces, $\epsilon_n \frac{E}{E_{QG}}^n$, acts as a suppression (or boosting) to the formation length and hence the interaction cross section. The suppression/boosting factor S is [90]:

$$S = \frac{\sigma_{LIV}}{\sigma_{BH}} = \frac{l_f}{l_0} \tag{5.13}$$

$$S = \frac{1}{1 + \epsilon_n \left(\frac{E}{E_{QG}}\right)^n \times \frac{E^2}{4m_e^2 c^4}} \tag{5.14}$$

where l_f is the formation length with LIV introduced and σ_{BH}, σ_{LIV} are the Bethe-Heitler cross-section with and without LIV introduced, respectively. For the sub-luminal scenario, the Bethe-Heitler cross section is suppressed ($S < 1$); the cross-section is boosted in the super-luminal case.

A more model dependent approach can also be taken, for example the derivation of Rubtsov et al. [93] is based on Standard Model Extension (SME) and yields the suppression factor at $\frac{E}{E_{QG}}^2 >> 4m_e^2$:

$$S(E, E_{QG}, n) = \frac{12 m_e^2 c^4 E_{QG}^2}{7E^4} \log \frac{E^4}{2m_e^2 E_{QG}^2} \tag{5.15}$$

This is in agreement with Equation 5.13 up to a logarithmic term. Since only the CPT conserving term in the Lagrangian is considered in the derivation, they only consider $n = 2$ in their calculation (since in the case of $\epsilon_n = 1$ photon decay is the dominant process, they only considered the subluminal scenario).

The suppression or the boosting of the Bethe-Heitler cross section will affect the formation of gamma-ray induced showers. The mean-free-path of a gamma ray (expressed in the unit of g/cm^2) in the atmosphere can be calculated as:

$$< X_0 >= \frac{m_{air}}{\sigma_{BH} \times S(E, E_{QG}, n)} \tag{5.16}$$

where m_{air} is the averaged molecular mass of air. So, with the introduction of LIV, the mean-free-path can be enhanced (suppressed). A longer mean-free-path of gamma rays means that, on average, the showers form deeper in the atmosphere (and the reverse for boosting of the cross-section). This can yield observable signatures from astrophysical gamma ray sources. As suggested by Rubtsov et al. [93], with the introduction of sub-luminal LIV the electromagnetic cascades initiated by gamma rays will form deeper, and hence the shower maximum will occur deeper in the atmosphere. If the depth of shower maximum limiting value (eg. the depth of the location of the telescopes or explicit shower height cut in the analysis) the air shower can no longer trigger the telescopes/detectors. This introduces an opposite effect to the EBL absorption of VHE gamma rays, where the modified threshold due to LIV makes EBL more transparent to gamma rays and hence leads to a higher than expected flux at large energy. Here, the reduced

probability of registering gamma ray showers means a suppressed measured flux for astrophysical sources at the largest energies. Alternatively, one can also treat astrophysical gamma-ray sources as a photon beam and investigate the distribution of the shower maximum X_{max}; the distribution of the shower max is affected by the distribution of the first interaction point of the gamma rays. By analyzing the shape of the X_{max} distribution one can extract direct measurements of the mean-free-path and hence the cross section itself. We will explore this idea in Chapter 6 and Chapter 7.

5.5 Target Astrophysical Sources for LIV Searches

To search for various signatures of LIV from astrophysical sources, there are some criteria for source selection that depend on the specific scenario in question. The one common requirement is the energy range available from the source. The breaking of Lorentz invariance is suppressed at an energy scale of E_{QG} that is expected to be close to the Planck scale; high energy (closer to E_p) is required for any observable effect to be present. We will briefly go through the main factors that effect a source to be a viable target for each of the LIV signatures we discussed above:

- Time of flight dispersion (section 5.4.2): The requirement for this search is an interplay between two factors: distance and source variability. The further away the source is, the more significant the time delay between photons would be. On the other hand, to be able to detect such delay, a variability in the source is required, the smaller the time scale of the variability the higher the sensitivity is for small time delay. The sensitivity to E_{QG} is then dictated by the ratio of $\frac{\Delta T}{\Delta E^n}$ to the variability time scale.
- Modified EBL absorption threshold (section 5.4.3): Similar to the time of flight studies, the source requirement for modified EBL absorption is also a two factor criteria. A far source is also preferred, as the longer distance

allows for a more significant difference in optical depth. However, the intrinsic spectrum of the source also needs to be hard enough so there are high energy gamma rays that can reach Earth. Essentially, we require detection of high enough energy gamma rays that propagated through a large enough space to place a stringent limit. This requirement somewhat limits the number of sources that can be used.

- Photon decay (section 5.4.4): Unlike the previous cases, photon decay requires only one criteria, namely energy of the photon, as the decay time for photons in the regime where it is kinematically allowed is small enough that any astrophysical sources that have photons detected at multi TeV energies can be used to place limits on E_{QG}.
- Modified Bethe-Heitler Cross Section (section 5.4.5): For this case, as the search is based on changes in the air shower formation, the only requirement is to have enough statistics of gamma rays with energy above 1 TeV. The sensitivity to E_{QG} is only related to the highest energy photons that are detected (depending on the method, telescope location can also be important).

The different kind of sources and the corresponding LIV signatures suitable for the source will be discussed here. For simplicity, we will use the following shorthand to denote the different LIV signatures:

- **TOF**: Time-of-flight dispersion.
- **EBL**: Modified EBL absorption threshold.
- **DECAY**: Photon decay.
- **CS**: Modified Bethe-Heitler Cross Section.

5.5.1 Gamma-ray bursts

Type of LIV searches: **TOF**

Gamma-Ray Bursts (GRB) are fast transients first observed in gamma rays in the late 1960s by the U.S. military satellites *Vela*, a group of 12 satellites originally designed to detect potential Soviet nuclear tests in space during the Cold War. They detected gamma-ray flashes of unknown origin that led to the first discovery of GRBs [94]. There was much debate about the origin of GRBs after the discovery (whether they originated from galactic or extra-galactic sources). The launch of NASA's Compton Gamma Ray Observatory (CGRO) in 1991, with one of the instruments on-board being the Burst and Transient Source Explorer (BATSE), established the isotropic nature of GRBs' spatial distribution [95]; this discovery is generally considered strong evidence of an extragalactic origin for GRBs.

Due to their fast variability and large redshift ($z \in [0.0085, 9.4]$), GRBs are a great target for **TOF** type searches of LIV. However, the large redshift of GRBs means that the energy of the observable gamma rays is limited due to EBL absorption. Also, the random (both spatial and temporal) nature of the GRBs means that they are hard for IACTs to observe due to the limited field of view and various observation constraints (zenith angle, moon ... etc.). Although there are promising recent developments with the detection of GRB 190114C by MAGIC [96] and GRB 190829A and GRB 180720B by H.E.S.S. [97, 98], most of the GRB observations in the gamma-ray energy range at the time of writing are made by satellite instruments (e.g. Figure 5–6 shows the photon count rate of GRB 090510 detected by Fermi/LAT and Fermi/GBM) that have limited collection area. The two factors combined limit the energy lever arm that can be obtained. For the case of $n = 1$ the lack of energy lever arm is mostly compensated by the large redshift, but for $n = 2$ the time delay scales as E^2 so the lack of photons at the TeV scale can be a limiting factor.

5.5.2 Active Galactic Nuclei

Types of LIV searches: **TOF**, **EBL**, **CS**

At the centre of some Galaxies there exists a compact core region that is extremely luminous; these core regions are called active galactic nuclei (AGN) and the galaxies that exhibit such features are denoted active galaxies. The commonly accepted model for AGNs is that the central engine powering the luminous emission is a supermassive black hole with strong accretion of materials. Although the current picture of AGNs is rather concise, there are numerous varying observational signatures for different type of AGNs. These characterizations of AGNs originated from observational classifications prior to the current unification scheme that relate the different observational signatures to the viewing angle of the central super massive black hole ([100],[101]). Figure 5–7 shows a schematic of this unification scheme.

Among the different types of AGNs, blazars are the most important for LIV searches due to their higher gamma-ray flux, large energy lever arm and fast variability. Blazers are normally in the low emission state but occasionally they go into a flaring high state. The time scale for flaring variability in gamma rays ranges from hours down to a few minutes; coupled with the cosmological distances, blazars are good for **TOF** type LIV searches. The energy range of the detected gamma rays can also reach $\approx$ 10 TeV for the closer ones. The wide range of redshift for blazars also makes them ideal for the **EBL** type LIV searches, where a balance between distances and the highest energy observables need to be found. For strong flares, some of the blazars can reach fluxes that are multiple times the flux of the Crab nebula, and this can also be a useful source for gamma ray event statistics for the **CS** type LIV searches.

5.5.3 Gamma-Ray Pulsars

Types of LIV searches: **TOF**

Pulsars are rapidly rotating magnetized neutron stars. Neutron stars are massive stars which have collapsed after the nuclear reactions fuelling the thermal and radiation pressure that support the structure of the star have ceased. Due to conservation of angular momentum, the collapse causes the neutron star to rotate very rapidly. The collapse also boosts the magnetic field on the surface of the neutron star considerably (typically up to 10^{12} G). The combined result of fast rotation, and strong magnetic field is that pulsars produce strong electro-magnetic emission ranging from radio to gamma rays; also, due to the fast rotation, the emission as seen on Earth is very consistently periodic. The first pulsar (PSR B1919+21) was discovered in 1967 by Jocelyn Bell Burnell [103] while analyzing data from a radio telescope. Jokingly nicknamed LGM-1 (standing for "Little Green Man"), it was first thought to be potentially a signal from extra terrestrial intelligence due to its consistent pulse (it was later renamed after it was shown to have an astrophysical origin after the discovery of the second pulsar). The three pulsars (Vela, Geminga and Crab, at the time of writing) that are detected in VHE gamma-rays have rotational periods below 1s (see Figure 5–8 for the example of the Crab pulsar). The fast variation of the pulsar makes it a good target of **TOF** type LIV searches; it compensates the lack of distance and can produce competitive limits. Also, the consistent nature of a gamma-ray pulsar means that the statistics of the photons observed can be accumulated over time (unlike the case for AGN where it relies on transient events). One drawback of using pulsars to perform LIV searches is the smaller energy range due to a soft spectrum; so, although the effect of EBL absorption is negligible (which is the limiting factor for GRBs) the highest energy observable is limited.

5.5.4 Crab Nebula

Types of LIV searches: **CS**, **DECAY**

The Crab Nebula is a supernova remnant associated with a bright supernova observed by Chinese astronomers in 1054 [105]. The Crab nebula can be seen at a wide range of electromagnetic wavelengths from radio to VHE gamma ray (up to $\approx$ 100 TeV [106]). It is widely considered as the most studied astrophysical object. In the field of VHE gamma ray astronomy, the Crab nebula was the first object successfully detected at TeV energies by the Whipple observatory [3] and thus started the rapid development of IACTs in the 1990s. For IACTs located in the northern hemisphere, it is generally used as the standard candle for calibration and tests of advanced analysis techniques.

The strong and consistent gamma-ray flux along with a relatively hard ($\gamma \approx -2.5$) spectrum makes it an ideal source for searches of types **CS** and **DECAY**. For these types of searches the achievable limit relies on the energy of the photon detected and the number of events detected at the highest energies; the Crab is suitable due to the high flux and hard spectrum that result in a large number of detected high energy photons.

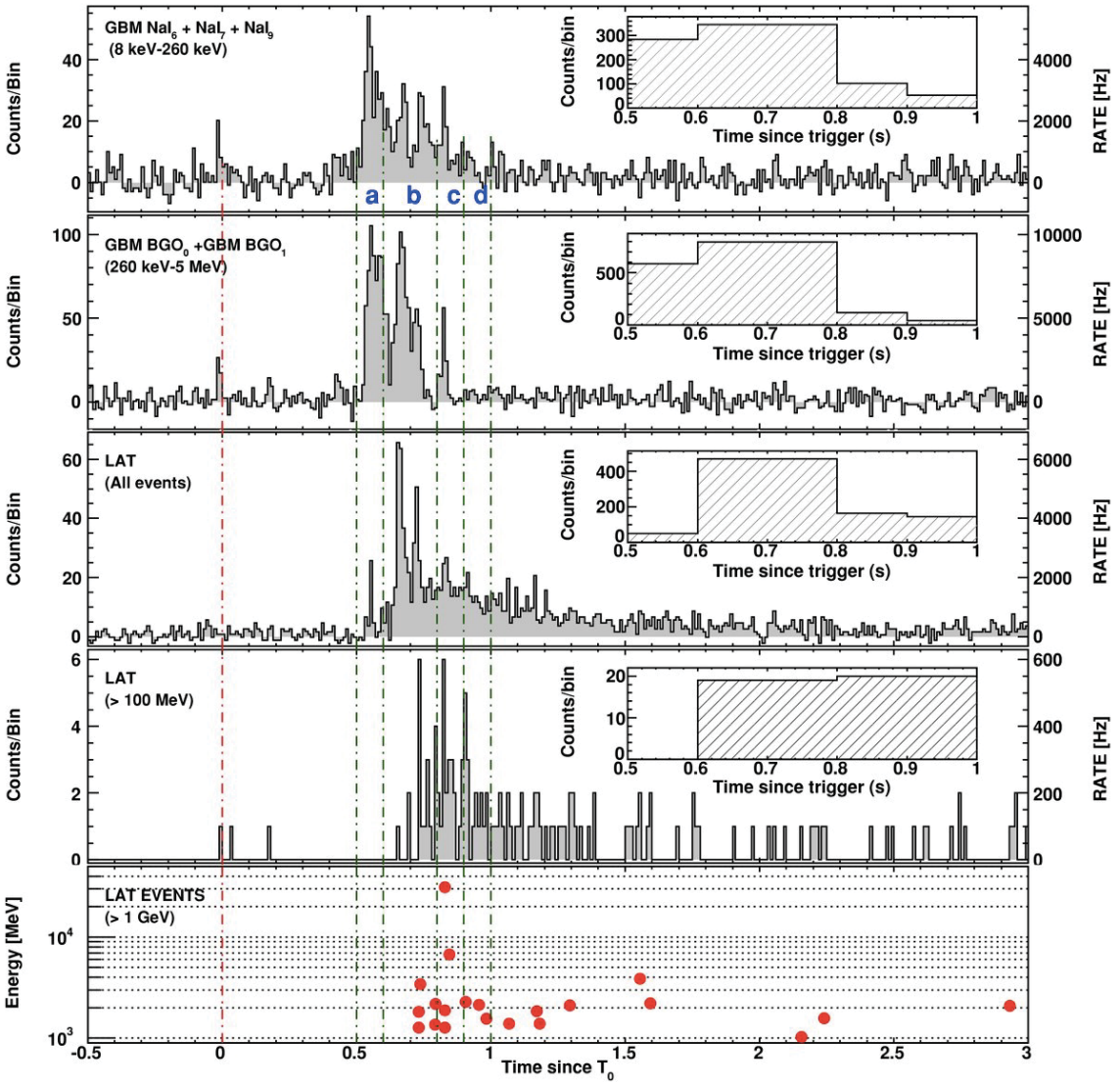

Figure 5–6: The four panels show the Fermi-GBM and Fermi-LAT gamma-ray detections of GRB 090510, from lowest to highest energy. The bin size for the top three light curve is 0.01 s. For the last panel, due to the lower statistics, the individual photon energy and the corresponding detection time is plotted. The red vertical dot-dashed line is the trigger time and the green lines are the boundaries used for spectral analysis in the paper from which the plot is extracted. Image credit: Figure 1 of [99].

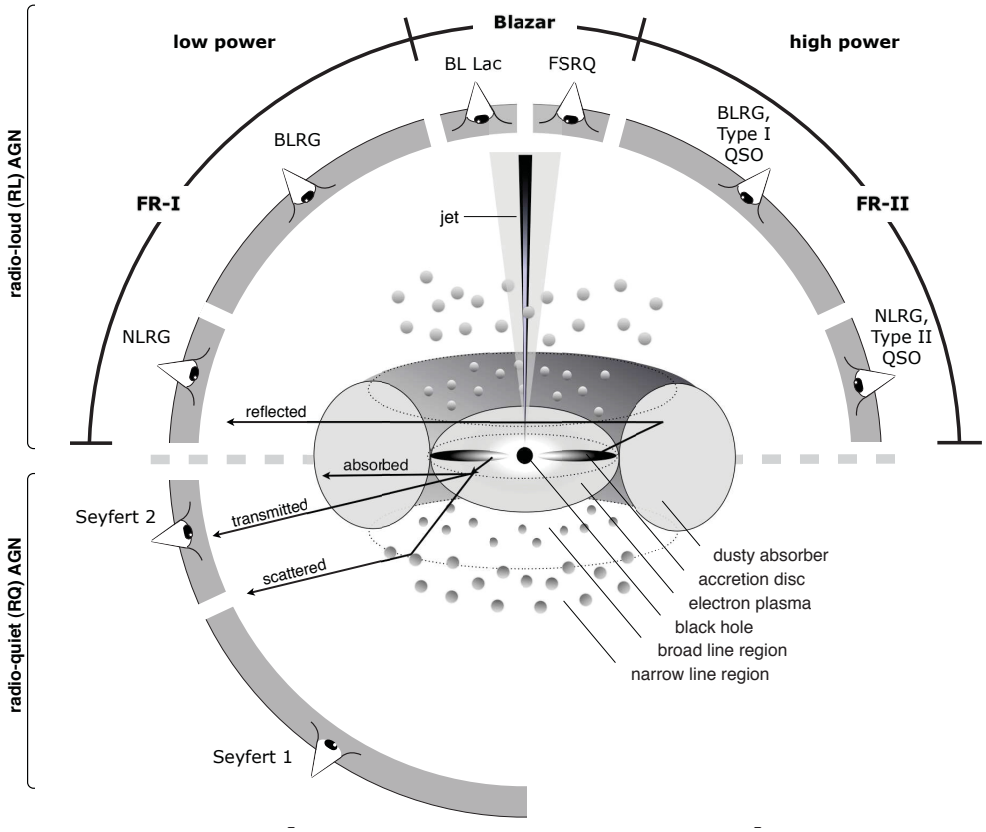

Figure 5–7: Schematic representation of the unification scheme of AGN based on viewing angle relative to the central engine. Image credit: Figure 1 of [102]

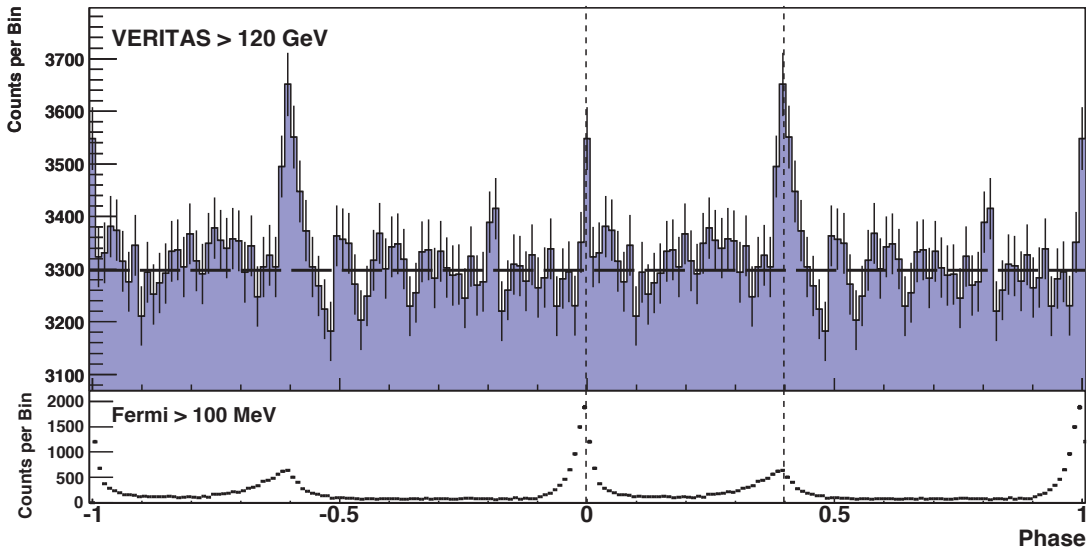

Figure 5–8: Phaseogram of the Crab pulsar detected by VERITAS (**TOP**) and Fermi (**bottom**). The vertical dashed lines indicate the location of the main pulse and the inter-pulse as determined by radio observations. The rotational period of the crab pulsar is ∼33 ms, and the width of pulses is ∼2% of the rotation period which means the variability time scale is sub-millisecond. Image credit: [104]

5.6 Summary of Past LIV Searches

Here, we will summarize the results of previous searches of LIV using HE and VHE gamma-ray observations. For the discussion here, only the linear and quadratic terms of the modified dispersion relation are of interest due to the constraint of the energy range of HE and VHE gamma rays.

A summary table of the best current limits on searches using time-of-flight dispersion can be found in Table 5–1. The best linear limit is achieved by Fermi observations of GRB 090510, which yield a limit exceeding the Plank scale and outclass all other sources. The limit is reliant on a single photon of ∼30 GeV coming from z=0.903; the high energy and large redshift enable the stringent constraint. However, this is the only Fermi-detected GRB with these properties to date and more observations of this type are needed to confirm the limit. The limits derived from IACT measurements are dominated by the PKS2155-304 flare observed by H.E.S.S. due to its exceptional timing characteristics and high photon flux. On the other hand, the PG1553+113 flare measured by H.E.S.S suffers from lower statistics but benefits from large redshift ($z \sim 0.5$) and was used to produce competitive limits. For more close-by AGNs such as Markarian 501, the linear limit is generally smaller than for AGNs of larger redshift; but, the higher energy range due to less EBL absorption makes them competitive for the quadratic limit. The LIV limits obtained using pulsars are similar to the limit from Markarian 501 and more competitive for the quadratic case. While some sources produced less competitive limits, the analysis sources of multiple classes and redshifts remains important for two reasons. The first is the reliance of all time-of-flight searches on the assumption of minimal intrinsic light curve dispersion, which is generally not well constrained. Secondly, the time delay due to LIV is redshift-dependent. A combined analysis of multiple source classes and redshift ranges would allow

a selection of the correct redshift-dependent dispersion and minimize the source-intrinsic effects [2].

Table 5–2 shows a summary of limits obtained using the modified EBL absorption method. As mentioned in an earlier section, the sensitivity of this method is the result of a balance between redshift and the intrinsic spectrum of the source. One such source is the blazar Markarian 501 [107]. As in case for time-of-flight searches, combining multiple sources can produce better limits. The first such an analysis was done by Biteau and Williams [87] in conjunction with constraints on the EBL spectrum. In 2019, Lang et al. [108] performed an updated analysis. This method generally produces limits that are higher than the time-of-flight searches; however, it is worth mentioning that the limits obtained here are only applicable to the subluminal LIV and the constraints are on a different effect.

For searches of photons decay, the only criterion is the detection of the highest energy photon. So, this kind of analysis is done on the measurements from HAWC, which is sensitive to energies up to 100 TeV, instead of IACTs. The analysis result using HAWC's detection of the Crab nebula at 100 TeV can also be found in Table 5–4.

Lastly, the modified Bethe-Heitler cross section search is similar to the photon decay searches where the limit is mainly affected by the highest energy detectable. Rubtsov et al. [93] and Satunin [115] performed the analysis based on searches for modifications to the Crab nebula spectrum using measurements from HEGRA, HAWC and the Tibet air shower array; the result can be found in Table 5–3.

Source Type	Source(s)	Redshift	Instrument	$E_{QG,1}$(GeV)	$E_{QG,2}$(GeV)	Reference
GRB						
	GRB 090510	0.903	Fermi-LAT	93×10^{18} GeV	13×10^{10} GeV	Vasileiou et al. [109]
AGN						
	Markarian 501	0.034	MAGIC	0.30×10^{18} GeV	5.7×10^{10} GeV	Martínez and Errando [110]
			H.E.S.S.	0.27×10^{18} GeV	7.34×10^{10} GeV	Abdalla et al. [107]
	PKS 2155-304	0.113	H.E.S.S.	2.1×10^{18} GeV	6.4×10^{10} GeV	Abramowski et al. [80]
	PG 1553+113	~ 0.49	H.E.S.S.	0.41×10^{18} GeV	21×10^{10} GeV	Abramowski et al. [111]
Pulsars						
	Crab Pulsar	0	MAGIC	0.55×10^{18} GeV	5.9×10^{10} GeV	Ahnen et al. [112]
		0	VERITAS	0.19×10^{18} GeV		Zitzer and VERITAS Collaboration [113]
	Vela Pulsar	0	H.E.S.S	0.0035×10^{18} GeV	0.064×10^{10} GeV	Chrétien [114]

Table 5–1: Summary table of limits obtained using time-of-flight dispersion.

Source(s)	Instrument	Redshift	$E_{QG,1}$(GeV)	$E_{QG,2}$(GeV)	Reference
Multiple Sources	Multiple Observatories		0.95×10^{19} GeV		Biteau and Williams [87]
Multiple Sources	Multiple Observatories		12.08×10^{19} GeV	2.38×10^{12} GeV	Lang et al. [108]
Markarian 501	H.E.S.S.	0.034	2.6×10^{19} GeV	7.8×10^{11} GeV	Abdalla et al. [107]

Table 5–2: Summary table of limits obtained using modified pair-production threshold.

Source(s)	Instrument	$E_{QG,1}$(GeV)	$E_{QG,2}$(GeV)	Reference
Crab Nebula	HEGRA		2.1×10^{11} GeV	Rubtsov et al. [93]
Crab Nebula	HAWC		5.7×10^{12} GeV	Satunin [115]

Table 5–3: Summary table of limits obtained using modified Bethe-Heitler cross section. The authors of these papers do not consider the linear scenario in their analysis.

Source(s)	Instrument	$E_{QG,1}$(GeV)	$E_{QG,2}$(GeV)	Reference
Crab Nebula	HAWC	3.4×10^{21} GeV	2.26×10^{13} GeV	HAWC Collaboration et al. [116]
2HWC J18250134	HAWC	15.5×10^{21} GeV	6.26×10^{13} GeV	HAWC Collaboration et al. [116]

Table 5–4: Summary table of limits obtained using photon decay.

6

Measurement of the Bethe-Heitler Cross Section for Multi TeV Gamma Ray Photon

In the last chapter we discussed different signatures of Lorentz invariance violation and the corresponding suitable sources. A common drawback for most of the LIV searches is the reliance on the assumptions of the astrophysics of the target sources (in the case of time-of-flight searches) or the EBL model. The alternative to searching for LIV based on propagation effects is to look for such a signature in the development of air showers within the atmosphere and thus minimize the reliance on assumptions of the astrophysical process; as discussed in Chapter 5, the introduction of Lorentz invariance breaking can suppress or boost the pair-production cross section (Bethe-Heitler cross section) of photons in a Coloumb field. The modification of the pair production cross section mainly affects the interaction position of the primary gamma-rays in the atmosphere. The first attempt at such searches using measurements by an IACT was done by Rubtsov et al. [93]; the authors suggested a suppression of the gamma-air cross section would cause a lowered acceptance of gamma-ray primaries above 10 TeV and hence a cutoff in the measured spectrum of astrophysical sources (in this case the Crab nebula) at tens of TeV.

While the analysis of Rubtsov et al. [93] used the signature of cross section changes in air-shower formation, it still relied on a robust understanding of the

intrinsic spectrum of the source as the search is for a non-astrophysical cut-off in the spectrum. In this thesis, we propose an alternative approach by directly measuring the interaction cross section through analyzing the depth distribution of the shower maximum.

6.1 Depth of Shower Maximum X_{max}

To understand the development of electromagnetic cascades such as gamma ray initiated air showers, the best option is to describe the cascade development as a function of traversed air mass. The number of interactions and the amount of energy loss of secondary particles depends on the number of atoms encountered. The traversed air mass (referred to as slant depth X from now on) is obtained by integrating the density of air along the direction of arrival of the shower through the atmosphere. For showers arriving at small zenith angle (generally the case for IACT observations), the atmosphere can be assumed to be plane parallel with density described as $\rho(h)$ where h is the height above sea level. The slant depth of a position at height h above sea level on the axis of an air shower arriving at zenith angle θ then can be calculated as:

$$X(h) = \int_h^\infty \frac{\rho(h)}{cos(\theta)} dh \tag{6.1}$$

The slant depth at which the energy deposit reaches maximum (referred to as shower maximum or shower max) is the target of this analysis. In the rest of the chapter we will use the notation X_{max} for the slant depth of the shower maximum and *shower height* to describe the physical height of the shower maximum above ground level at VERITAS (located at 1.2 km above sea level). The conversion between the two relies on knowing the atmosphere density profile $\rho(h)$; in Figure 6–1, the slant depth for showers with 0° zenith angle at different height above ground level from VERITAS is shown.

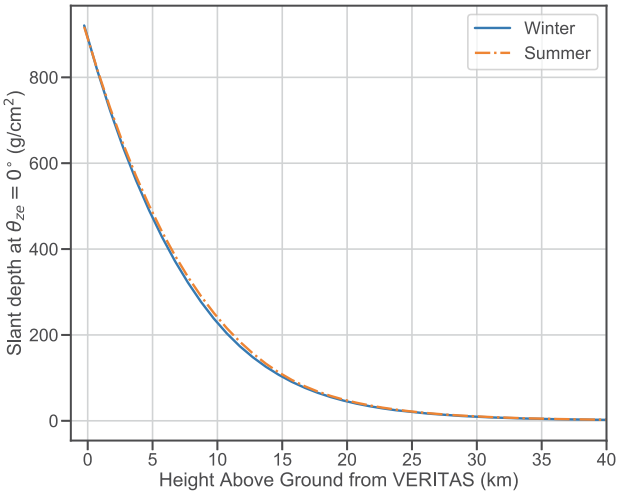

Figure 6–1: Conversion of height to slant depth at zenith angle of 0 degree. Both the standard summer and winter atmospheric profile is shown. The x-axis is the height from VERITAS which is located at 1270 m above sea level. The full atmosphere depth is ~ 1000 g/cm^2.

6.2 Characterizing X_{max} Distribution

Analogous to the measurement of the proton-air interaction cross section by the Pierre Auger and Telescope Array (TA) observatories [117, 118], one can obtain the interaction cross section of gamma rays with air molecules using information from X_{max} distributions. Several functions have been proposed to characterize the shape of the X_{max} distribution. Traditionally, the exponentially modified Gaussian (EMG) distribution is widely used among the ultra-high-energy cosmic-ray (UHECR) community. The motivation behind the EMG function is the assumption that X_{max} can be decomposed into two distinct components: the first interaction point X_{first} and the length of shower development ΔX (Equation 6.2):

$$X_{max} = X_{first} + \Delta X \tag{6.2}$$

If one assumes the X_{first} and ΔX are statistically independent, the probability density function $P(X_{max})$ can be expressed as a convolution of $P(X_{first})$ and

$P(\Delta X)$. $P(X_{first})$ is known to follow an exponential decay with the length scale to be the mean free path of the primary particle. Although $P(\Delta X)$ is not known *a priori*, a simple approach is to assume $P(\Delta X)$ to be a Gaussian distribution with mean at μ and variance σ^2. The resulting form of $P(X_{max})$ is then [119]:

$$f(x|\lambda,\sigma,\mu) = \frac{1}{2\lambda} e^{-\frac{x-\mu}{\lambda}+\frac{\sigma^2}{2\lambda^2}} \left(1 - \mathrm{erf}(\frac{\mu - x + \sigma^2/\lambda}{\sqrt{2}\sigma})\right) \tag{6.3}$$

An advantage of the EMG function is that the parameters λ, σ and μ have simple physical interpretations. λ is the mean free path of the primary particle, and μ, σ describe the mean and standard deviation of the distribution of ΔX, respectively.

An alternative to the EMG is the Generalized Gumbel distribution (GMB) [120]:

$$f(x|m,n,\mu) = \frac{1}{m}\frac{n^n}{\Sigma(n)}\exp\left(-n\left[\frac{x-\mu}{m} + \exp(-\frac{x-\mu}{m})\right]\right) \tag{6.4}$$

The GMB distribution arose first from the study of extreme value statistics and was later found to have a connection to leaky system dynamics; Domenico et al. [121] first proposed to use Equation 6.4 to describe X_{max}. As has been shown by Antal et al. [122], GMB is the asymptotic limit of the sum of a series of random variables drawn from an exponential probability density function. Hence, one can interpret the shower max X_{max} as a sum of interaction depths of multiple generations of particles [119]. Under this construction, the mean free path of the primary particle is then $\frac{m}{n}$.

In this analysis, we will be using the GMB function to extract the mean free path of the primary particle. We follow the suggestion of [119], in which the authors concluded that the GMB better describes the X_{max} distribution compared to the EMG, especially for the tails of the X_{max} distribution. Figure 6–2 shows an example of fitting GMB to CORSIKA gamma-ray simulations.

6.3 Shower Height Distance Correction

To measure the interaction cross section of the primary gamma-rays, we need a method to reconstruct the X_{max} (derived from shower height) accurately. In chapter 4, we described two different methods that are currently implemented in `VEGAS` and `EventDisplay` to calculate the shower height: the single telescope shower height and the two-telescope parallax method. The main method that is used currently is the two telescope parallax method. However, as pointed out by Hillas [123], due to the combination of limited angular acceptance of a Cherenkov telescope and the light cone geometry, the height from which most of the photons are emitted as seen by a telescope would be different given different distances to the shower core. To demonstrate this, Figure 6–3 shows the average shower height of simulated gamma-ray showers using the single telescope method. The events are selected based on the distances between the telescope and the shower core. We can clearly see that depending on the distance to a telescope, the reconstructed height of the shower will have different biases: positive bias (higher) for shower cores landing further than the rim of light pool ($\sim$ 100 m) and vice versa. The same issue exists for the two telescope parallax method. By using the parallax of the shower images from two telescopes, one effectively calculates the average of the results of two single-telescope shower heights. As there is more phase space for showers landing further away from the array, the end result of averaged shower heights as seen by two telescopes would be a net positive bias in reconstructed shower height. Figure 6–4 shows the mean reconstructed X_{max} of simulated showers at different energies compared with the CORSIKA simulations; one can see that above 200 GeV the reconstructed shower height remains steady at $\sim$ 250g/cm^2 ($\sim$ 10km) while the real shower max should go deeper in the atmosphere as the energy of the primary gets higher.

6.3.1 Impact distance correction

In effect, the measured single-telescope shower height is a function of the impact distance D and the real shower height (H): $H_{\rm rec}(H, D)$. A more accurate shower height measurement then can be achieved through modelling the relation $H_{\rm rec}(H, D)$. Because the standard VERITAS simulation software chain does not save the X_{max} information, we need to produce a custom set of CORSIKA simulations and pass through the CARE detector simulation package with the X_{max} information stored. The shower height is obtained by using the CORSIKA keyword "LONGI" [49], which directs CORSIKA to fit the particle longitudinal distribution of a shower to the Gaisser-Hillas function [124] and obtains the X_{max}. The X_{max} of each unique shower is then converted to physical height using the corresponding atmosphere density profile (winter or summer). We match the simulated showers to the event number generated by CARE. Once a "true shower height" for every event is established, we can start to study the function $H_{\rm rec}(H, D)$.

Figure 6–5 shows 2D histograms of the reconstructed single telescope shower height versus real shower height of 1.5×10^7 gamma-ray shower simulations; the showers are selected based on their reconstructed impact distance to a telescope. We use the binned average (binned in real height) of the reconstructed shower height as the calibration curve of the single telescope method (Figure 6–6) within each impact distance range. For real shower heights within the range of 5 km to 11 km (roughly $X_{max} = 500$ g/cm^2 to $X_{max} = 200$ g/cm^2) the relation between average reconstructed single telescope shower height and the real height are reasonably linear (as shown by the red line in Figure 6–6). The upward bias below 5 km ($X_{max} > 500$ g/cm^2) is due to the clipping of shower images by the edge of the camera; as the single-telescope shower height calculation is based on the centroid of a shower image, a truncated image causes the centroid of the image

to be closer to the centre of the camera than a non-truncated one hence giving a higher reconstructed height. Within this range we can then model $H_{\rm rec}(H, D)$ as a linear function:

$$H_{\rm rec} = T_{\rm slope}(D) \times \Delta H_{\rm real} + \Delta_{\rm offset}(D) \tag{6.5}$$

Once $T_{\rm slope}(D)$ and $\Delta_{\rm offset}(D)$ are known we can calculate the distance-corrected shower height as:

$$H_{\rm corrected} = \frac{H_{\rm rec} - \Delta_{\rm offset}(D)}{T_{\rm slope}(D)} \tag{6.6}$$

To characterize the functions $T_{\rm slope}(D)$ and $\Delta_{\rm offset}(D)$ we can bin the simulated shower events in impact distance (D) relative to each telescope and fit the calibration curve in every impact parameter bin with a linear function (Figure 6–6). Figure 6–7 shows the $T_{\rm slope}$ and $\Delta_{\rm offset}$ at different impact parameter bins for showers initiated at 20° zenith angle. For the reconstruction algorithm, we fit the points in Figure 6–7 with an empirical piecewise linear function. As an example, for showers at 20°, the slope and offset fit functions are:

$$T_{\rm slope}(D) = \begin{cases} -2.7 \times 10^{-3}[1/\text{m}](D - 150[\text{m}]) + 0.80 & D \leq 150\text{m} \\ 0.80 & 150\text{m} < D \leq 180\text{m} \\ -2.1 \times 10^{-3}[1/\text{m}] \times (D - 180[\text{m}]) + 0.80 & 180\text{m} < D \end{cases} \tag{6.7}$$

$$\Delta_{\rm offset}(D) = \begin{cases} 4.9 \times 10^{-2}[\text{km/m}](D - 150\text{m}) + 2.8km & D \leq 150\text{m} \\ 2.84\text{km} & 150\text{m} < xD \leq 210\text{m} \\ 3.33 \times 10^{-2}[\text{km/m}] \times (D - 210\text{m}) + 2.84\text{km} & 210\text{m} < D \end{cases} \tag{6.8}$$

The reason for choosing a three-region piecewise linear function for the fit arise from the expectation that the optical properties of shower image would be different when a telescope is inside, outside, and on the rim of the light pool (also, a single linear function will result in a poor fit).

For each event, we calculate the average of the corrected single-telescope shower heights from telescopes with a valid shower image:

$$H_{\text{corrected}} = \frac{1}{N} \sum_i \frac{1}{T_{\text{slope}}} (H_i(D_i) - \Delta_{\text{offset}}(D_i)) \tag{6.9}$$

Here, D_i is the impact distance for the shower to telescope i and N is the number of telescopes with valid images.

In Figure 6–8 we show the average reconstructed X_{max} using the distance-corrected method on simulated events compared to X_{max} directly obtained from CORSIKA simulations. The energy dependency follows what is expected from standard electromagnetic shower development theory as implemented in CORSIKA (based on [125]) much better than using the standard two-telescope parallax method. At low energy, the up-tick in the average shower height is due to trigger selection effects of showers close to the energy threshold. For showers that are high up (shallower) and close to the energy threshold the showers are too dim to trigger the array hence a selection bias towards deeper showers. So, the turnover of the uptick goes up in energy as we look at showers initiated at larger zenith angles as the energy thresholds are higher. At the higher energy end, due to the deeper average shower max the bias is mainly due to the image clipping effect. Looking at showers at larger zenith angles can reduce such bias. At a given X_{max} and impact distance, showers with a larger zenith angle are further away from the array due to the thicker atmosphere and that means a smaller angular separation between shower image centroid and the centre of the field of view .

In the next section, we will take a more comprehensive look at the performance (resolution and bias) of the distance correction method.

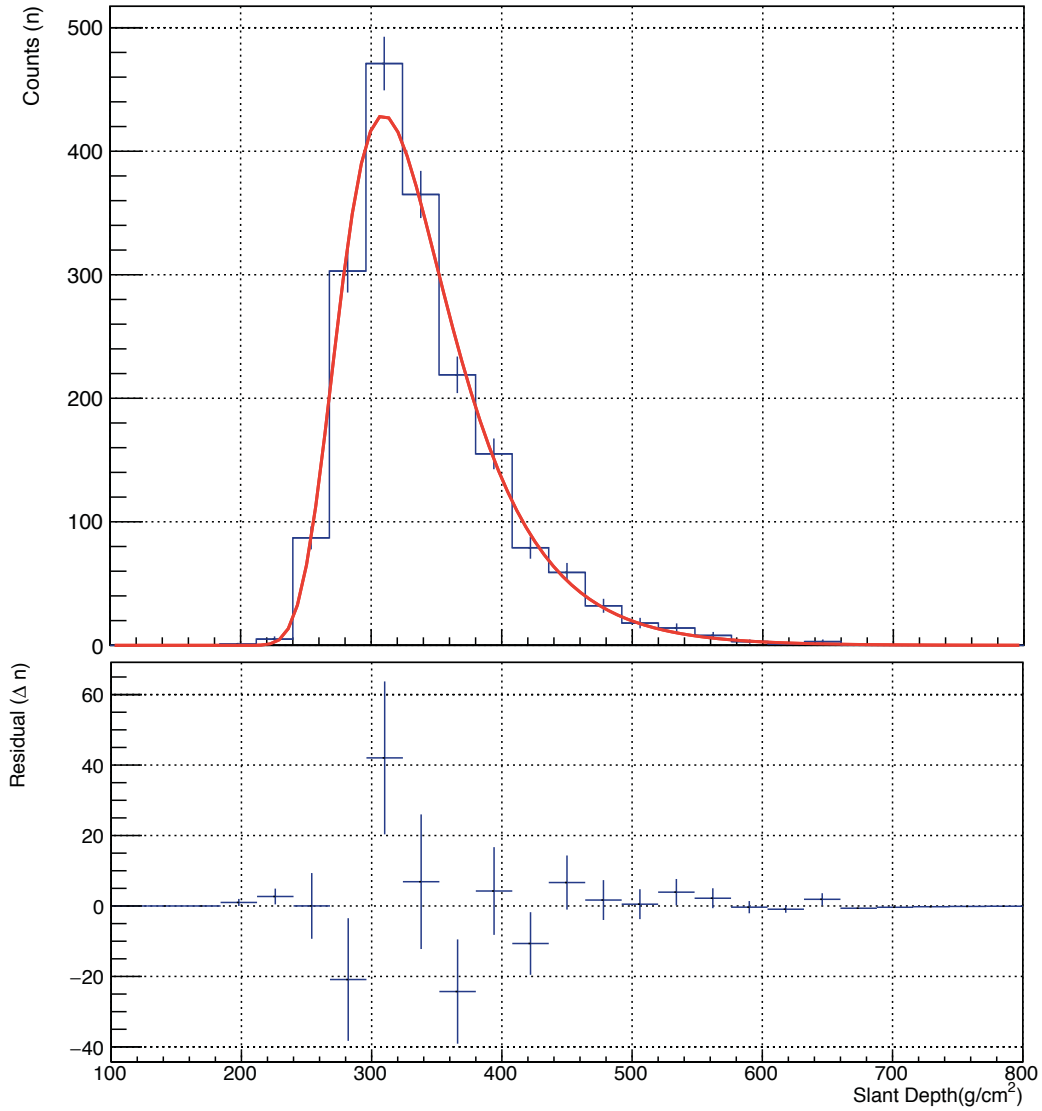

Figure 6–2: Fitting the GMB function (**redline**) to CORSIKA simulations (1.1 TeV $< E <$ 1.5 TeV). The lower plot is the residual of the fit. The fit yields a good χ^2 of 16.7 for 13 d.o.f.

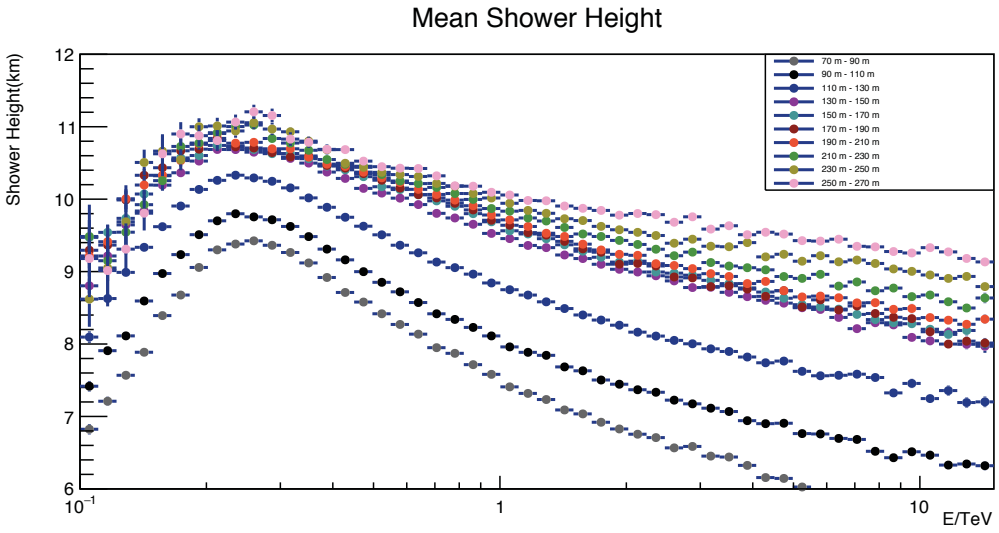

Figure 6–3: Averaged reconstructed single telescope shower height H_{rec}. The events are selected based on their impact distance relative to a given telescope.

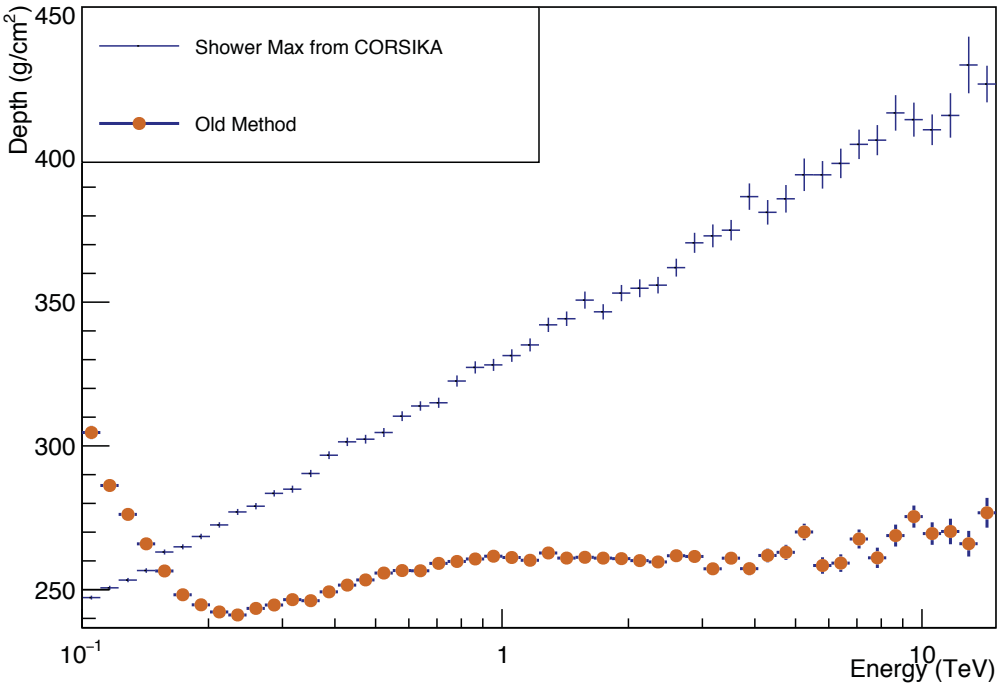

Figure 6–4: Averaged reconstructed X_{max} calculated using the two-telescope parallax method (referred to as the "old method" in the legend). The energy dependency of the mean clearly does not agree with expectations from shower simulations (blue points). In fact, the average reconstructed X_{max} stays almost constant above 200 GeV.

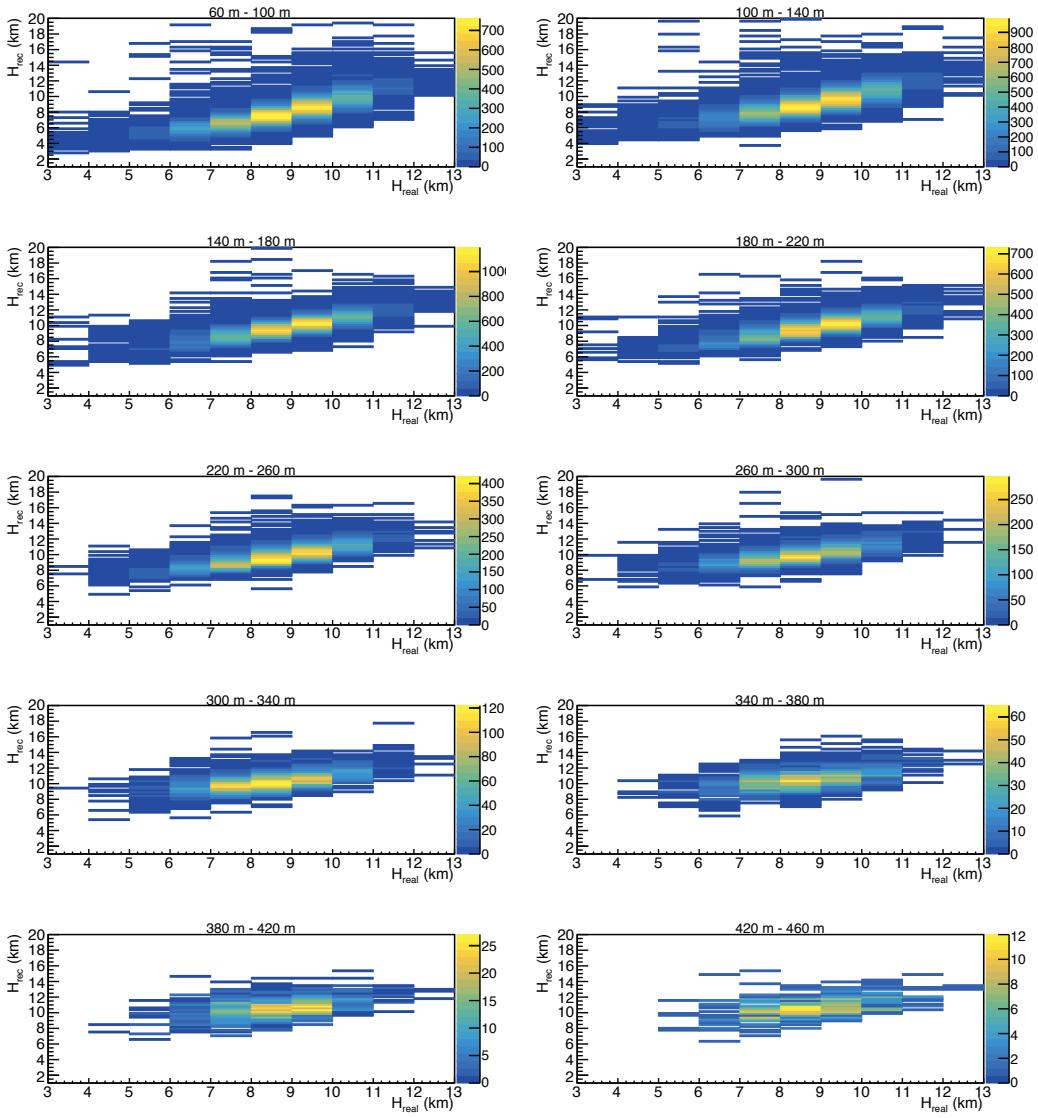

Figure 6–5: 2D histogram of reconstructed shower height versus real shower height. Each plot corresponds to a different impact distance bin. The binned average (binned in real height) of the reconstructed shower height of each plot here is shown in Figure 6–6.

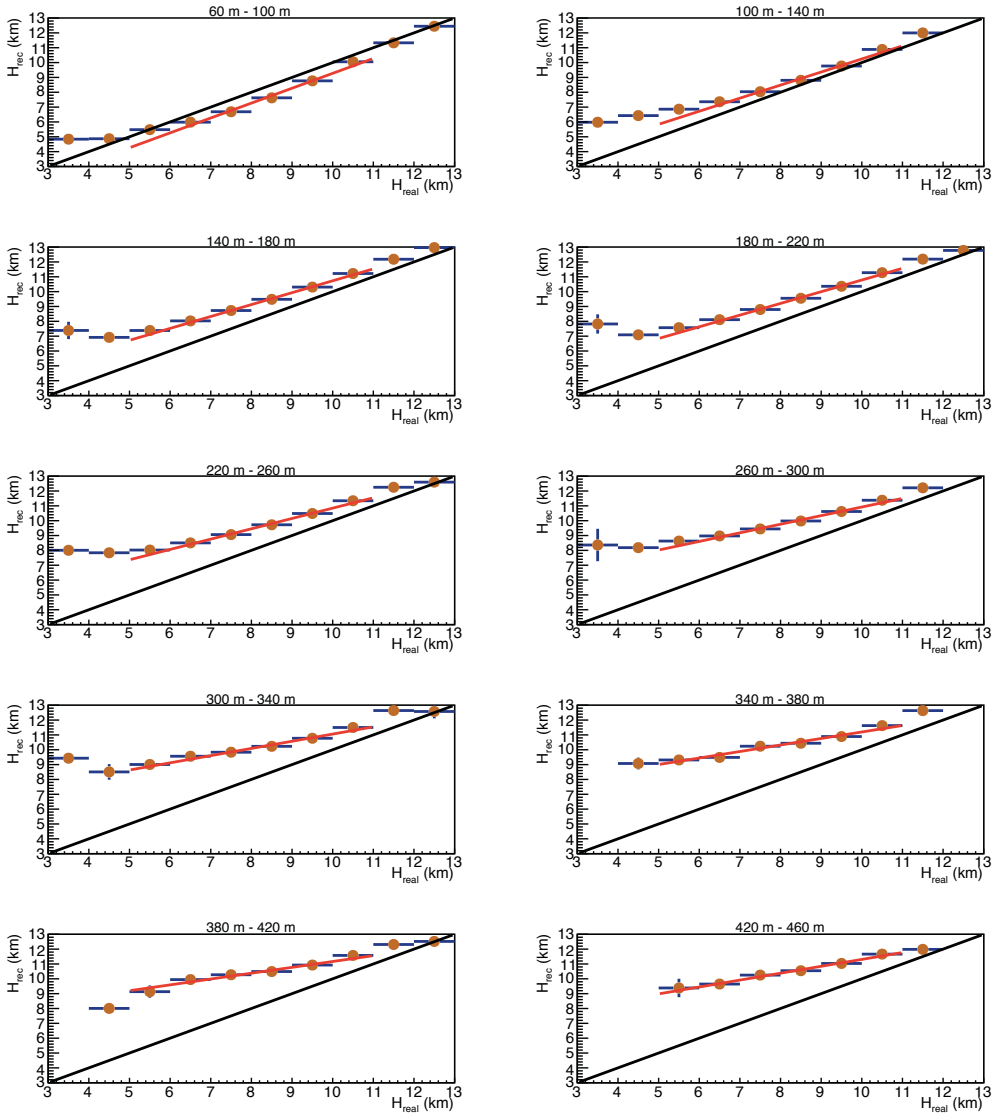

Figure 6–6: Profile of the distributions in Figure 6–5. The black line represent H_{rec}=H_{real}.

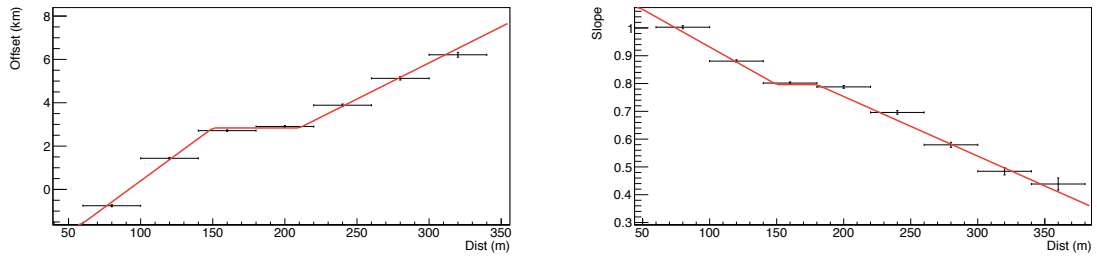

(a) Offset $\Delta_{\mathrm{offset}}(D)$ (b) Slope T_{slope}

Figure 6–7: Slope and Offset of the calibration curve as a function of impact distance. The x error bars represent the bin sizes for impact distances.

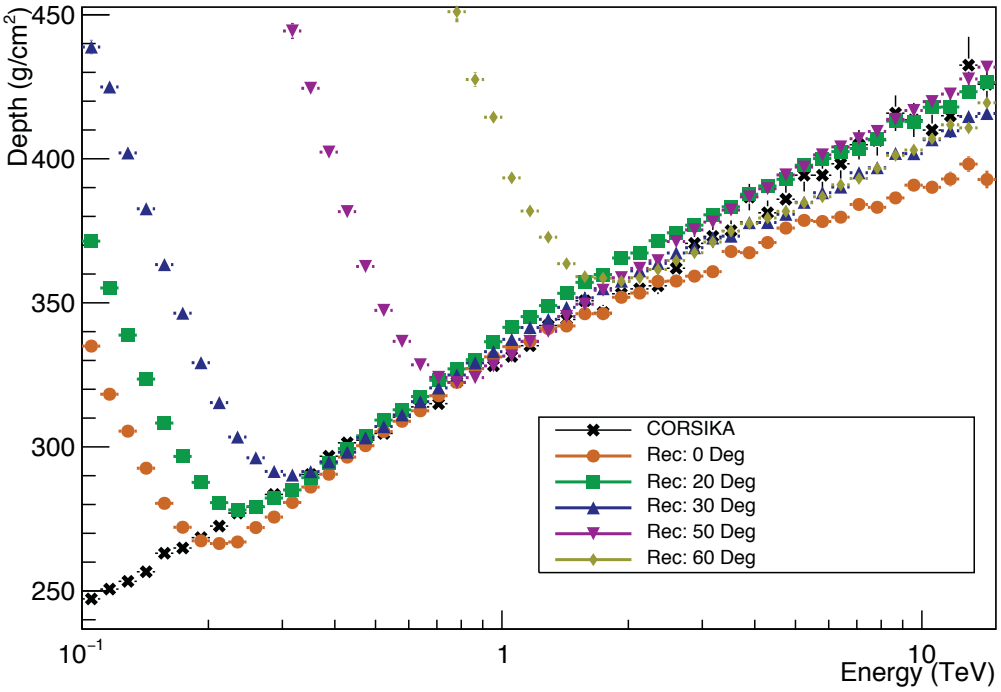

Figure 6–8: Average distance-corrected reconstructed shower max at different zenith angles. The black points are average shower max calculated directly from CORSIKA simulation without going through any detector simulation.

6.3.2 Bias and Resolution

To look at the bias and resolution of the impact-distance corrected shower height, we can look at the profile distribution of reconstructed shower height versus the true shower height for simulated showers. In Figure 6–9, the distribution of reconstructed X_{max} for showers with true X_{max} between 327 g/cm^2 and 386 g/cm^2 (separated into three bins) at 20° zenith angle is plotted. As the shape of the distribution is non-gaussian, especially for showers that are deeper ($\sim$ 200 g/cm^2) we fit the 10% to 85% percentile of each real shower max bin with a Gaussian function to extract the peak position of the distribution to characterize the bias of the reconstruction method and the standard deviation of the distribution to study resolution.

Figure 6–10 shows the resolution and bias of the distance correction method for different real X_{max} at 20° zenith angle. The resolution is relatively constant between 35 g/cm^2 to 45 g/cm^2 (a relative resolution of $\sim$ 10%). The bias, however, goes from $0g/cm^2$ to about $20g/cm^2$; the bias peaks around real depth of $\sim$ 300 g/cm^2. The optimization of the distance correction was done without applying an energy selection, so a look at the primary-energy dependent effect of the bias and resolution curves is necessary. The resolution curves are not very sensitive to the range of energy we are looking at. On the other hand, the bias is much more sensitive. For showers above 1 TeV there is an almost constant bias of $\sim$ 25 g/cm^2 up to a depth of 400 g/cm^2. The result we obtained without an energy cut is in fact a combination of showers of different energies; for shallow showers ($<$ 300 g/cm^2) the statistics is dominated by the lower energy showers and the reverse for deeper shower ($>$ 400 g/cm^2). The constant rise in bias when there is no energy cut between $250g/cm^2$ and $325g/cm^2$ is the result of shifting from low energy showers (with bias $\sim 0g/cm^2$) to higher energies (bias $\sim 20g/cm^2$). In a

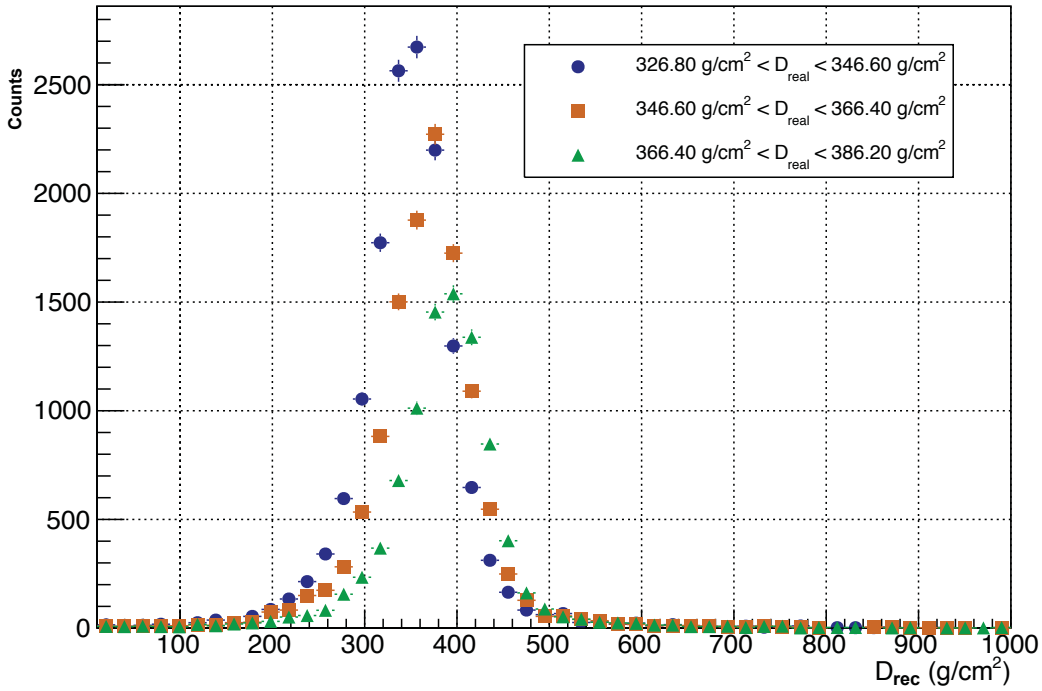

Figure 6–9: Distribution of reconstructed shower max at different true shower max bin. Three true shower max bins between 327 g/cm^2 and 386 g/cm^2 are drawn here. The number of events in each X_{max} range are different because at a deeper X_{max} the showers are on average more energetic and the simulations are produced based on a power-law spectrum.

later section, we are going to use this result when extracting the cross section from the reconstructed shower height distribution.

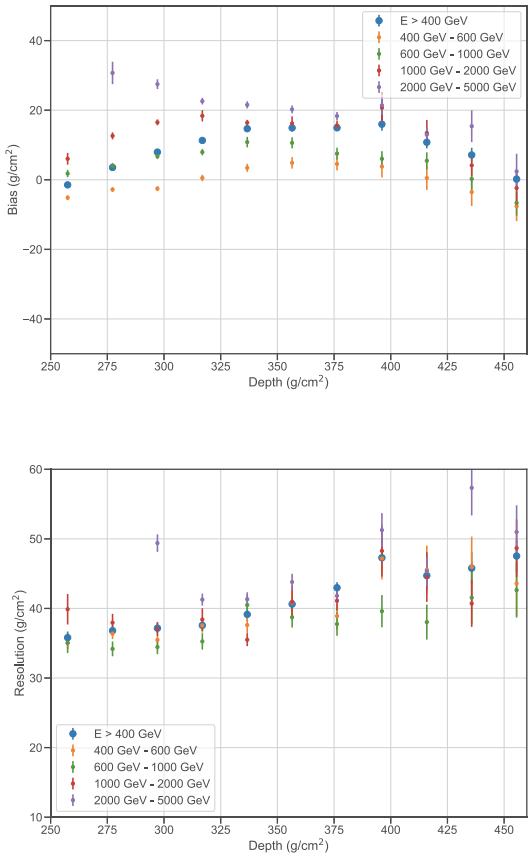

Figure 6–10: Bias(**top**) and resolution(**bottom**) as a function of X_{max}. The points of different colours correspond to different energy ranges. For the energy bin from 2 TeV to 5 TeV, the points below 280 g/cm^2 are removed as that is beyond the fit range we apply to data.

6.4 Extraction of a Cross Section from Data

To perform this analysis, we only look at the shower development of gamma-ray initiated showers in the atmosphere so there is little dependency on the astrophysical sources where the primary gamma rays were produced. While conceptually there is no restriction on the gamma-ray source that can be used for this analysis, we decided to use the standard candle and the brightest persistent source, Crab Nebula, as the target because this is the first analysis of this type.

6.4.1 Data Selection

For this analysis, we use VERITAS data after the upgrade of the camera (V6 epoch, see Chapter 3) up to the 2016 -2017 season. A strict quality selection cut is applied; all runs need to be designated as "A" weather by the observer and by FIR fluctuations (see Chapter 3). Here we focus the analysis on the data taken at zenith angles between 15° and 25° to maximize the amount of data available and at the same time avoid the biases due to image clipping for deep showers. At larger zenith angle, there is more atmospheric material for the the air shower to penetrate hence the shower will be further away from the array; this reduces the number of events that are affected by the imaging clipping problem. Under the above strict selection criteria, we have 24.3 hours (56 runs) of data.

We applied loose gamma-hadron cuts on the mean scaled width (MSW) and mean scaled length (MSL) which restrict both parameters to be within the range of 0.5 to 2. The background subtraction is done using the reflected region method (for more details see Chapter 4).

6.4.2 Instrument response modified GMB

As mentioned in Section 6.3.2, both bias and resolution of the impact distance correction method is on the order of $\sim 10\%$ which means when fitting the shower height distributions with the GMB function, we cannot directly apply the GMB function. As an example, Figure 6–11 shows the reconstructed X_{max} distribution

compared to the real X_{max} distribution obtained directly from CORSIKA. The reconstructed shower max distribution is wider than that of the real X_{max} as the non-zero resolution widens the distribution and the biases for shallow and deep showers cause a long tail on either end of the distribution.

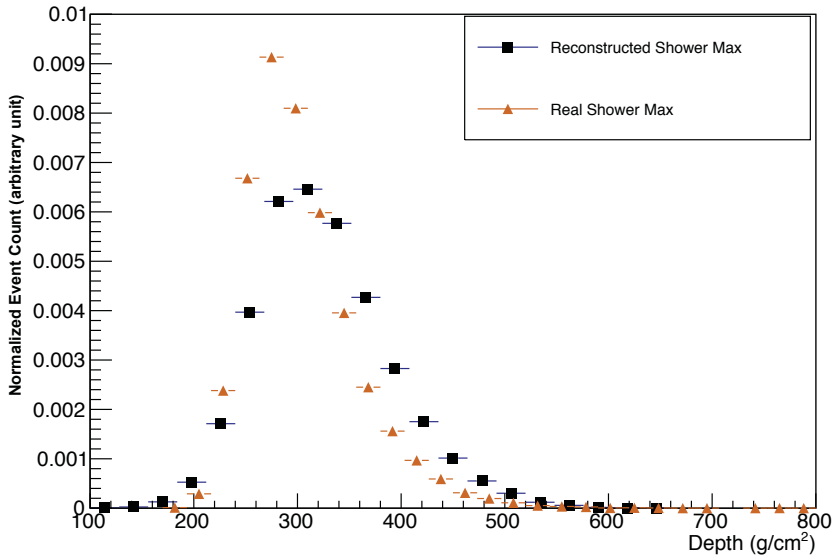

Figure 6–11: Reconstructed X_{max} vs. true X_{max} distribution (450 GeV - 740 GeV).

Apart from the bias and resolution of the reconstruction method, the acceptance of showers at different heights will also modify the shape of the distribution. We calculate the acceptance for showers at different heights from simulations using the number of generated showers ($N_{generated}(X_{max})$) with a given X_{max} and the number of events that pass the final event selection cut ($N_{passed}(X_{max})$):

$$A(X_{max}) = \frac{N_{passed}(X_{max})}{N_{generated}(X_{max})} \tag{6.10}$$

An example of the height acceptance is shown in Figure 6–12.

To address this, we convolve the GMB function with the resolution and bias function:

$$F(x'|m,n,\mu) = \int G(x' - x + B(x)|R(x)) \times f(x|m,n,\mu) \times A(x)dx \qquad (6.11)$$

where $f(x|m,m,\mu)$ is the GMB function and $G(x|R)$ is a Gaussian distribution centred at zero with a width of R and $A(x)$ is the acceptance function. For simplicity, we use the approximation that the bias and resolution of the new method are a Gaussian distribution and look at the systematics coming from this approximation by fitting the simulated showers (seen next Section 6.4.4). The values of R, B and $A(x)$ are then obtained from our characterization of resolution and bias.

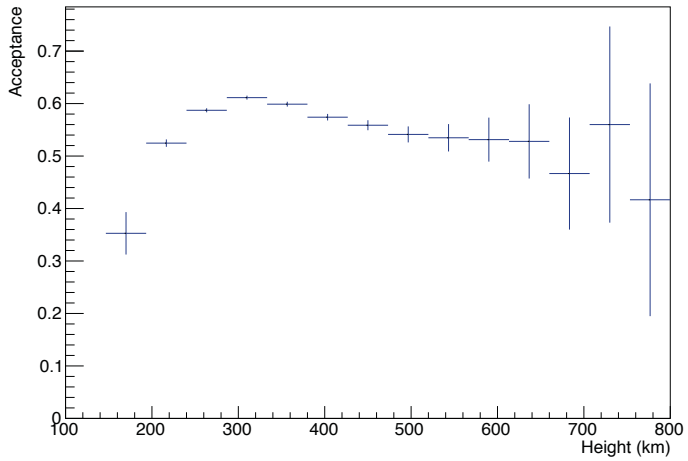

Figure 6–12: Acceptance curve for showers with reconstructed energy above 400 GeV.

To speed up the calculation of Equation 6.11 we parameterize the resolution and bias functions with quadratic functions for four energy bins (Table 6–1). Figure 6–13 shows an example of the fit to simulated events at energy bin 1.65 TeV to 2.02 TeV. The acceptance functions are parameterized using 5th order polynomials.

Bin ID	Energy Range
0	0.4 - 0.6 TeV
1	0.6 - 1.0 TeV
2	1.0 - 2.0 TeV
3	2.0 - 5.0 TeV

Table 6–1: Energy bins for characterizing instrument responses.

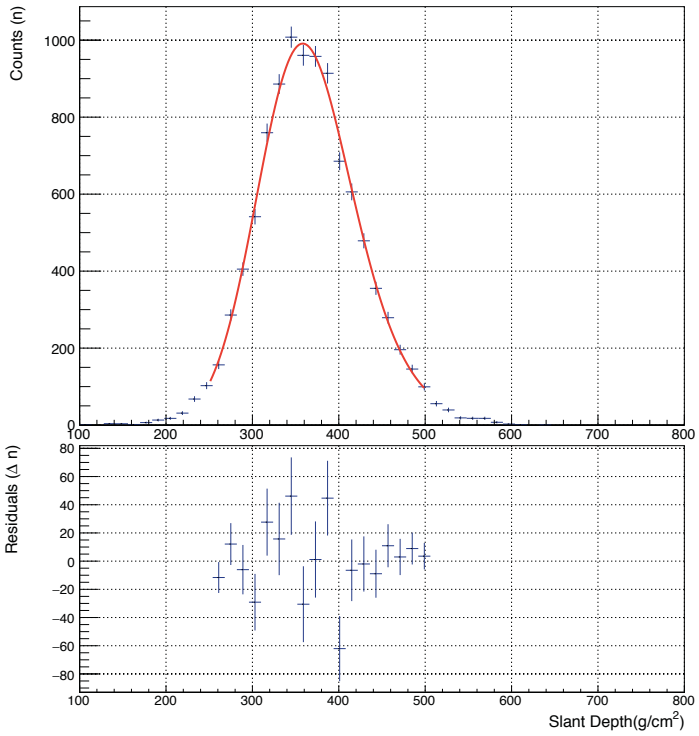

Figure 6–13: Fitting instrument-response-modified GMB function to simulated data in energy bin 1.65 TeV to 2.02 TeV.

6.4.3 Result of Cross Section Measurement

To apply the fit function to data, we modify the GMB function (Equation 6.4) so there are only three free parameters: N (Normalization), $L = \frac{m}{n}$ (mean free path), and μ (averaged shower length). GMB itself has three free parameter, along with normalization there should be four parameters. To reduce the dimension of the fit, we obtain the parameter m by fitting to CORSIKA simulations. Figure 6–14 shows the fit result to the X_{max} distribution for the energy bin 400 - 500 GeV; the instrument response modified GMB function fits to the data very well.

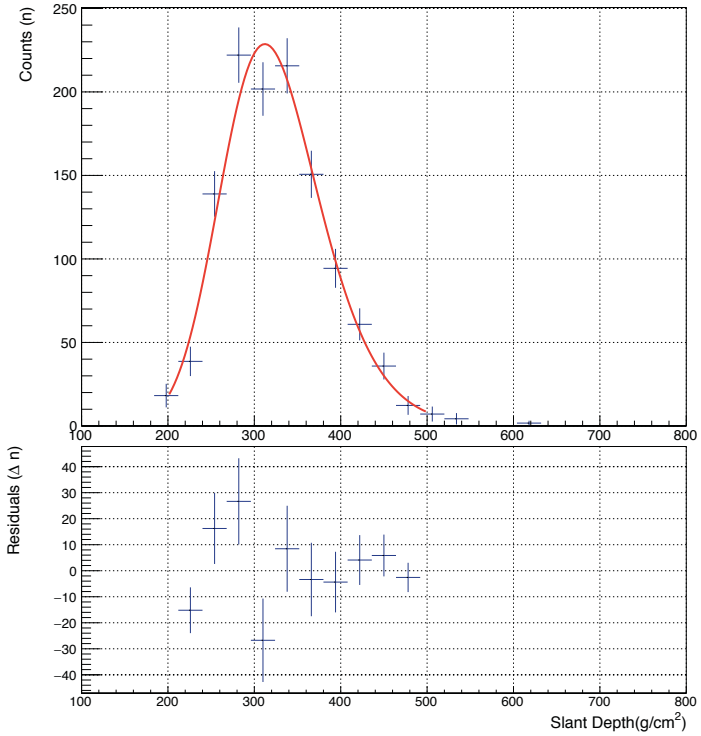

Figure 6–14: Fit of instrument-response-modified GMB function to data in energy bin 500 GeV to 600 GeV. The fit parameter *Lambda* corresponds to the mean free path of the primary gamma rays ($\frac{m}{n}$ in Equation 6.4).

In this case, we obtain the mean free path to be 46.6 ± 4.2 g/cm^2. For fit results of other energy bins, see appendix A. The conversion from mean free path to cross section is as follows:

$$\sigma[b] = \frac{m_{air}[\mathrm{g}]}{L[\mathrm{g/cm^2}]} \times 10^{24} = \frac{m_{air}[\mathrm{g/mol}]}{L[\mathrm{g/cm^2}] \times 0.6022} \tag{6.12}$$

where L is the mean free path and m_{air} is the average nuclear mass of air.

After converting the mean free path L to a cross section, we have the result of the measurement in Figure 6–15 and Table 6–2. Here, systematics are included in the plot; we will discuss factors that contribute to systematics in the next section. We restrict the fit range to be between 200 - 500 g/cm^2 for energy bins below 1 TeV and 250(280) - 500 g/cm^2 for energy bins above 1 TeV (2 TeV). In this energy range the primary photon interacts with the atmosphere mainly

through pair-production (Bethe-Heitler process[4]). In the high-energy limit the Bethe-Heitler cross section can be expressed in terms of radiation length X_0 [13]:

$$\sigma_{BH} = \frac{7}{9}\frac{m}{X_0} \tag{6.13}$$

where m is the atomic mass. This yields $\sigma_{BH} = 0.51$ b in dry air. Our measured averaged cross section is 0.55 ± 0.04 (stat + sys) b (the systematics are added in quadrature) which is in good agreement with the theoretical value.

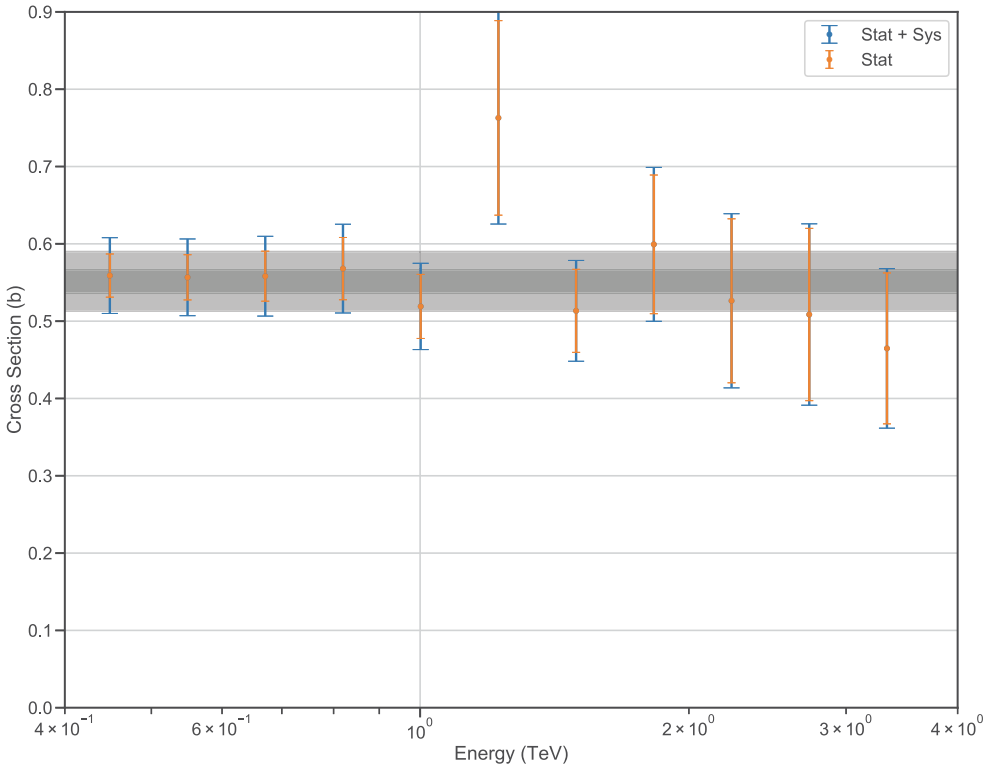

Figure 6–15: Result of the cross section measurement. The shaded region corresponds to the averaged cross section with statistical uncertainty (dark grey) and systematic uncertainty (light grey).

6.4.4 Systematic Uncertainties

There are three main components of systematics we will be discussing: the inaccuracy of modelling the bias and resolution functions, atmospheric fluctuations

Energy Point(TeV)	Cross Section (b) with statistical uncertainties
0.45	0.558 ± 0.028
0.55	0.556 ± 0.029
0.67	0.558 ± 0.032
0.82	0.567 ± 0.040
1.00	0.519 ± 0.041
1.22	0.762 ± 0.126
1.50	0.513 ± 0.053
1.83	0.599 ± 0.089
2.23	0.526 ± 0.106
2.73	0.508 ± 0.111
3.33	0.464 ± 0.097
Average	0.552 ± 0.015 (stat + sys method) ± 0.022 (sys atm) ± 0.028 (sys ze)b

Table 6–2: Summary of measured cross section. The energy point is calculated using the method described in [126].

and the mixing of showers observed at different zenith angles. While our analysis is reliant on the air showers simulation, because we are only concerned with the electromagnetic showers which are well understood, the systematic effects associate with the simulation are expected to be small and may be ignored.

Inaccuracy in Bias and Resolution Function Characterization

In the last section, we described the process of taking into account the resolution and bias of the reconstruction method when fitting the shower max distribution. However, the approximation (namely, that they are Gaussian distributed) is relatively crude and starts to break down for shallow and deep showers (below 200 g/cm^2 and above 500 g/cm^2), which is the reason for restricting fit ranges. So, to characterize the contribution of such inaccuracy to the systematic uncertainty, we apply the fitting procedure to simulated showers (Figure 6–16); the large statistics available from simulations allows for small statistical uncertainty from the fit and the difference between the fitted result and the expected value is dominated by systematic effects.

As can be seen, the point to point fluctuations do not agree statistically with a constant. We use this to estimate the systematic uncertainty; we calculate the

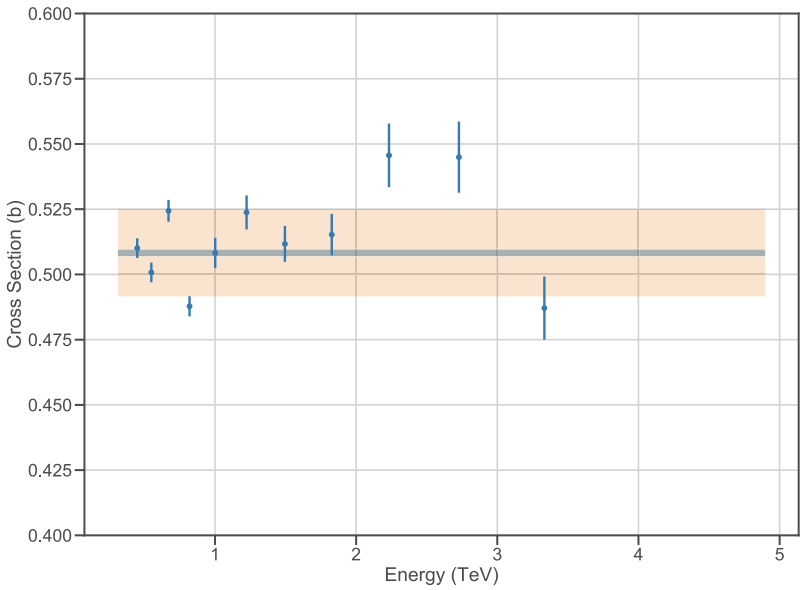

Figure 6–16: Applying instrument response modified GMB to simulated showers. The systematic uncertainty due to model inaccuracy is estimated from the deviation from the mean cross section.

necessary uncertainty level for the points to agree with a constant. An extra 3% uncertainty is required. The differences between the fitted mean cross section and the theoretical value is the systematic bias introduce by this method. The mean cross section is 0.3% above the theoretical value, which is small enough that we ignore it. We also looked at the effect of mischaracterization of the acceptance function. Removing the acceptance function in the fit results in a 3% shift in mean cross section which limits the systematic uncertainty associated with the mischaracterization of the acceptance function.

Atmospheric Model

The conversion from shower height to slant depth is done using the standard winter and summer atmosphere profile; however, there are day-to-day fluctuations of the atmosphere density profile. To estimate the systematic associated with the mismatch of atmosphere profile, we first look at how big the day-to-day

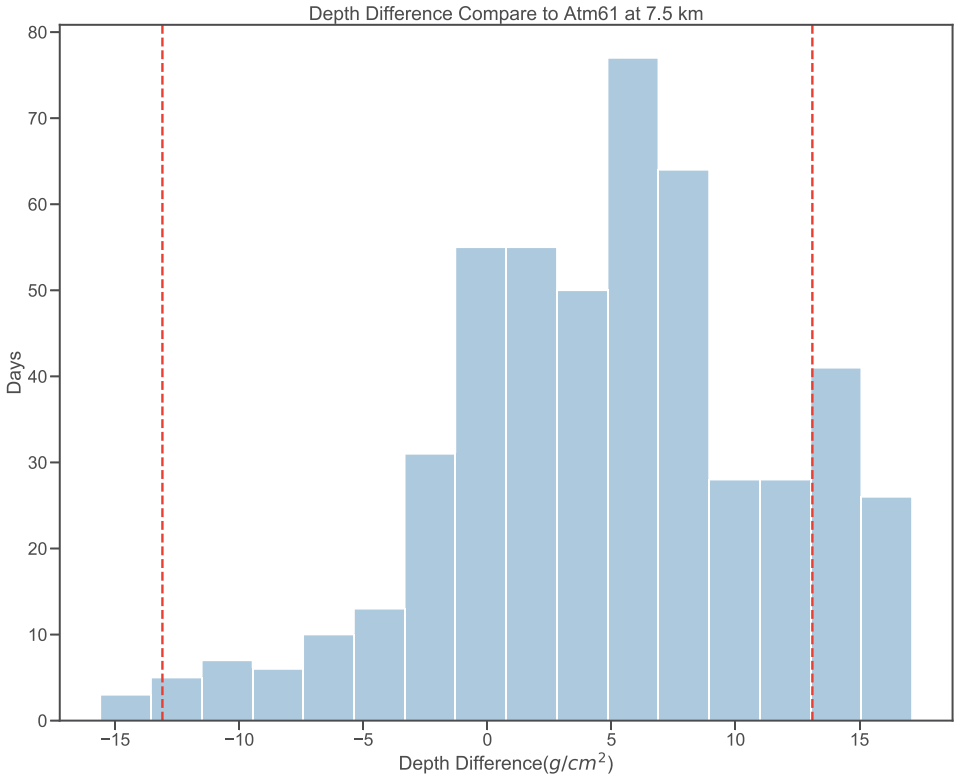

Figure 6–17: Depth difference distribution at 7.5 km. The red dashed lines show the difference in depth at 7.5 km between the winter and summer atmospheres.

fluctuation is. Figure 6–17 shows the slant depth difference at 7.5 km above ground (where the bulk of the shower maximum resides at ~ 300 g/cm^2) converted using the standard winter atmosphere and the daily atmosphere profile measured by radiosonde balloons released daily from Tucson airport. The distribution of the depth differences is well encompassed by the difference between the standard winter and summer atmosphere profiles. So, we can use the difference of cross section results between using winter and summer atmosphere on the entire data set as an estimation of the effect of changing atmosphere profile. Using the summer versus winter atmospheric model yields a difference in mean cross section of 4%.

Zenith Angle Mixing

The optimization of the method is done on fixed zenith angle simulations at 10° intervals. However, our runs are selected to have average telescope zenith angles in the range of 15° to 25°. To look at the effect of using data from a different angle compared to what we optimized on, we separate our data set into three zenith angle bins (the bins are selected so the number of runs in each bin are roughly equal) and calculate the mean cross section (Figure 6–18). The systematic is again estimated by calculating the extra uncertainty required for the three zenith angle bins to be consistent with a constant. This yields a 5% systematic uncertainty.

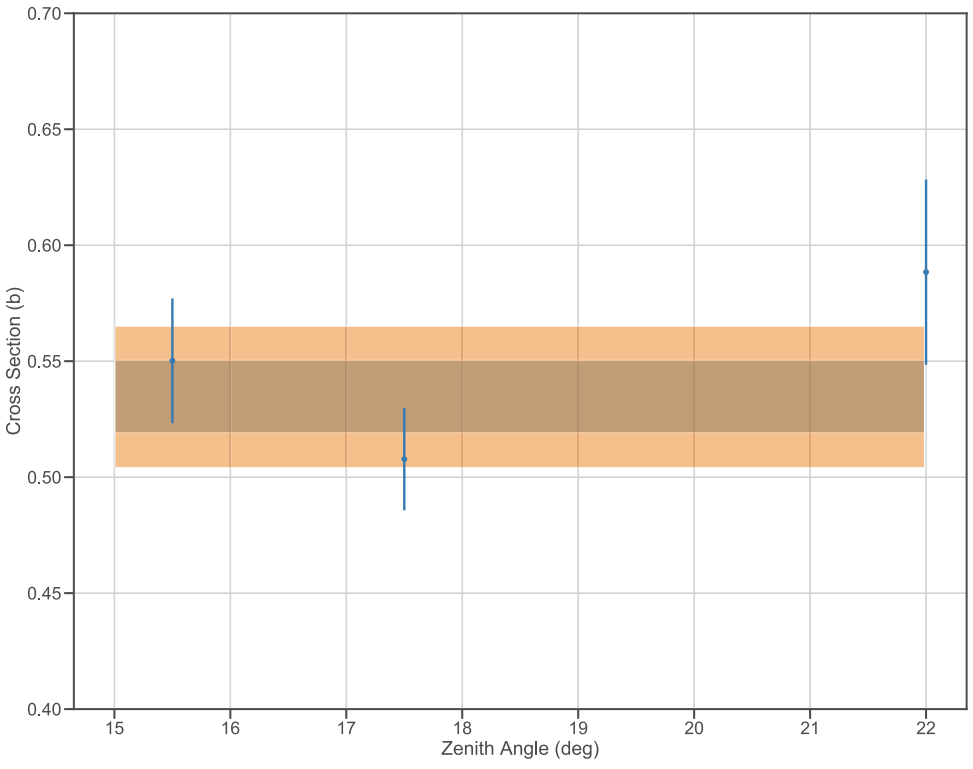

Figure 6–18: Average cross section using data from three zenith angle bins.

In Table 6–3 we list a summary of the main systematics.

Model inaccuracy	$\sim 3\%$
Zenith angle mixing	$\sim 5\%$
Atmosphere Model	$\sim 4\%$
Acceptance	$< 3\%$
Total	7%

Table 6–3: Summary of systematic sources.

7

Constraining LIV Effects from the Bethe-Heitler Cross Section

Now that we have the cross section measurements, we want to constrain the effect of LIV on the Bethe-Heitler cross section. Here we choose to follow the derivation by Vankov and Stanev [90]; the suppression/boosting factor for the interaction cross section can be calculated as:

$$S_n(E) = \frac{1}{1 + \eta_\gamma \frac{E^{2+n}}{4M_{LIV}^n m_e^2}} \tag{7.1}$$

where $\eta_\gamma \in \{-1, 1\}$ signifies whether the breaking of Lorentz symmetry is super-luminal or sub-luminal. The reason to choose the approach of Vankov and Stanev [90] is that it is less model dependent as the LIV effect discussed there stems directly from the modified dispersion relation instead of through specific implementation of extra terms in the Standard Model Lagragian (like [93]). Using the definition in Equation 7.1 we can calculate the suppression/boosting of the cross section at each energy. Figure 7–1 shows the cross section with suppression/boosting at 10^{17} GeV for the linear case and at 10^{10} GeV for the quadratic scenario. A direct comparison of the boosted/suppressed cross section with the measured result up to 3 TeV clearly shows that there is no obvious evidence of breaking of Lorentz variance in this regime.

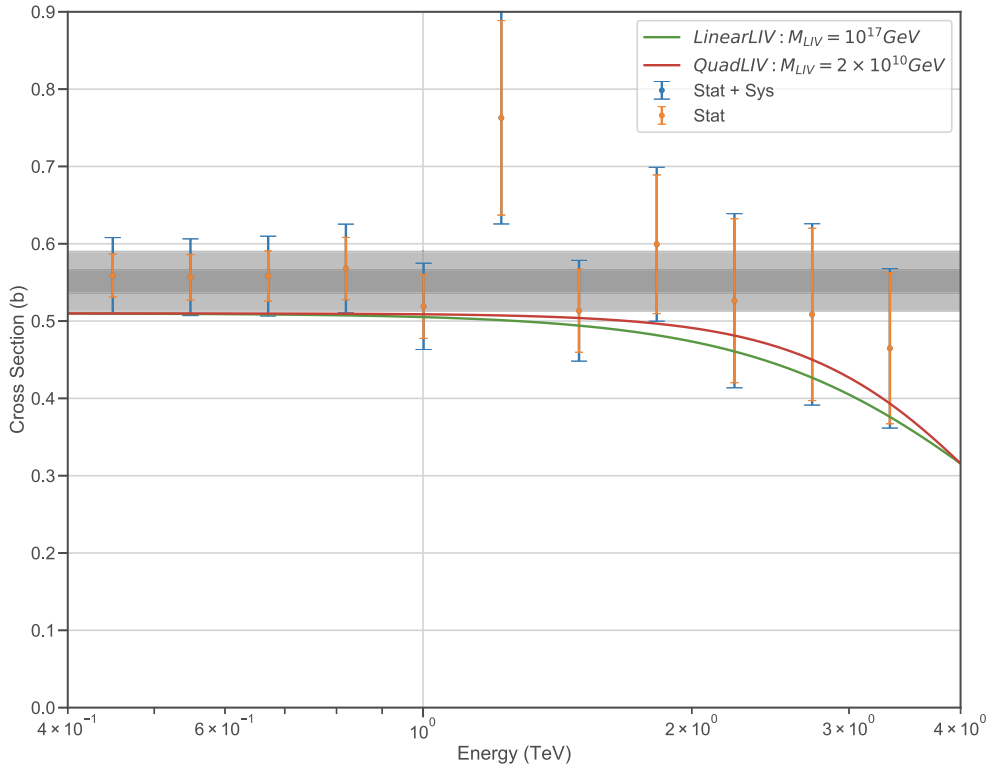

Figure 7–1: Measured cross section with suppressed cross section using Equation 7.1. The shaded region corresponds to the averaged cross section with statistical uncertainty (dark grey) and systematic uncertainty (light grey).

7.1 Extracting Limits on M_{LIV} using a Maximum Likelihood Method

We can set a limit on the quantum energy scale using the maximum likelihood (ML) method [13]. We calculate the likelihood using the χ^2 statistic from data points discussed in the previous Chapter. To include systematic effects in this analysis, we add the 3% systematic effect due to model inaccuracy to each point's uncertainty. For the other two main systematic sources (the atmospheric model and the zenith angle mixing), they affect the mean of the cross section so we will treat them together; they are treated differently from the model inaccuracy systematic effect.

The simplest form of the log likelihood function can be written as:

$$-2\log(L_n(M_{LIV})) = \sum_i \frac{(C(E_i) - (0.51\text{b}) \times S_n(E_i|M_{LIV}))^2}{\sigma(E_i)^2} \tag{7.2}$$

where $L_n(M_{LIV})$ is the likelihood function, $C(E_i)$ is the measured cross section value at energy E_i and $\sigma(E_i)$ is the corresponding uncertainty. $S_n(E_i|M_{LIV})$ is the aforementioned suppression factor due to LIV. Using the maximum likelihood method, the estimation of M_{LIV} is achieved through maximizing the function $L_n(M_{LIV})$. It is conventional (and more practical) to reformulate the maximization as a minimization of the function $-2\log(L_n)$. The boundary of a 1-sided confidence interval with a 95% confidence level (CL) of the parameter M_{LIV} can then be constructed as [13]:

$$-2(\log(L_n(M_{LIV,95\%})) - \log(L_{n,max})) \leq 2.71 \tag{7.3}$$

where $L_{n,max}$ is the maximum of the likelihood function. However, from a closer look at data (Figure 7–1), it is obvious that there is a systematic shift in mean cross section compared to the expected value of 0.51 b. While the mean cross section is in agreement with the theoretical value (0.55 ± 0.04 b versus 0.51 b), we need to take this systematic shift into account when constructing the likelihood function. This can be achieved by adding a nuisance parameter δ to account for the shift:

$$-2\log(L_n(M_{LIV};\delta)) = \left[\sum_i \frac{(C(E_i) - (0.51\text{b}) \times (1+\delta) \times S_n(E_i|M_{LIV}))^2}{\sigma(E_i)^2}\right] + \left(\frac{\delta}{\Gamma_\delta}\right)^2 \tag{7.4}$$

Here we assume the shift parameter δ follows a Gaussian distribution with a width of Γ_δ; this adds the extra term $\left(\frac{\delta}{\Gamma_\delta}\right)^2$ to the log likelihood function. For the value of Γ_δ, we adopt the estimated systematic effects of the atmospheric model and zenith angle mixing (added in quadrature gives a 6% effect).

With the added nuisance parameter, the straight forward condition in Equation 7.3 cannot be applied directly. In such a scenario, the profile likelihood ratio method can be applied. When using the profile likelihood method, the test statistic $D_n(M_{LIV})$ can be constructed as:

$$D_n(M_{LIV}) = -2log\left[\frac{L_n(M_{LIV};\hat{\hat{\delta}}(M_{LIV}))}{L_n(\widehat{M_{LIV}};\hat{\delta})}\right] \tag{7.5}$$

where the single-hatted parameters $\widehat{M_{LIV}}$ and $\hat{\delta}$ maximize the likelihood function globally; the double-hatted variable $\hat{\hat{\delta}}$ is the value of δ that maximizes the likelihood function for a given M_{LIV}. The test statistic $D_n(M_{LIV})$ can be used as a standard log likelihood function [127]. So, we can then construct the one-sided 95% confidence level limit as:

$$D_n(M_{LIV,95\%}) < 2.71 \tag{7.6}$$

Following the definition of Equation 7.4, the profiled nuisance parameter $\hat{\hat{\delta}}$ can be solved analytically:

$$\begin{cases} A(M_{LIV}) = (0.51\text{ b}) \times \sum_i \frac{S(E_i|M_{LIV})\times C(E_i)}{\sigma(E_i)^2} \\ B(M_{LIV}) = (0.51\text{ b}) \times \sum_i \frac{(0.51\text{ b})\times S(E_i|M_{LIV})^2}{\sigma(E_i)^2} \end{cases} \tag{7.7}$$

$$\hat{\hat{\delta}}(M_{LIV}) = \frac{B(M_{LIV}) - A(M_{LIV})}{A(M_{LIV}) + 1/\Gamma_\delta^2} \tag{7.8}$$

The denominator $L_n(\widehat{M_{LIV}};\hat{\delta})$ in Equation 7.5 is solved numerically using the *iminuit* package [128] (a python interface for the MINUIT C++ package [129]), utilizing the *MIGRAD* algorithm.

7.2 Results of the Limit

The result of the analysis is presented in Figure 7–2 and Figure 7–3 for the four scenarios we are interested in: linear and quadratic LIV combined with super-luminal and sub-luminal scenarios. While in the framework of Standard Model

Extension (SME) linear LIV would be disfavoured as it violates CPT symmetry (see the work of [93]), the derivation of Equation 7.1 by [90] does not rely on the SME framework so we will still calculate the limit for the linear case. For the case of sub-luminal LIV, a minimum in the test statistic is found at a finite M_{LIV}. This comes primarily from the drop in the measured cross section in the highest energy bin. However, this minimum is not statistically significant; this is also the reason for a less constraining limit for the sub-luminal scenario compared to the super-luminal one. Overall, no significant suppression of the Bethe-Heitler process has been observed in this regime. We summarize the 95% CL lower limits for the quantum energy scale M_{LIV} in Table 7–1.

	Linear ($n = 1$)	Quadratic ($n = 2$)
Sub-luminal ($\eta = 1$)	0.64×10^{17} GeV	1.4×10^{10} GeV
Super-luminal ($\eta = -1$)	2.4×10^{17} GeV	2.8×10^{10} GeV

Table 7–1: Measured one-sided 95% CL lower limits for the quantum energy scale M_{LIV}, for the four cases of interest.

7.3 Discussion

Our limit is in a comparable range to the time-of-flight limits (see Table 5–1) obtained using IACTs, $\sim 10^{17}$ GeV for the linear case and $\sim 10^{10}$ GeV for the quadratic case. Although these are not the best limits to date, these are the first LIV constraints using VHE gamma rays that are purely based on air shower formation. Unlike many other LIV constraints based on astrophysical sources, this approach has minimal unknown systematics due to astrophysics. The time-of-flight LIV searches are limited by the understanding of the potential intrinsic energy dispersion of the sources [110, 2] which in general is assumed to be negligible (however, it has been shown that it is possible to have strong intrinsic effects that are comparable or stronger than the propagation effect [130]). For the modified EBL absorption method, it is highly reliant on the EBL model used in the analysis [87, 108]. It is worth mentioning that our results are complementary to the limits

obtained through time-of-flight studies and EBL absorption; these searches look for effects of different processes and are a purely kinematic effect. For the dynamic LIV effect, the recent result by the HAWC Collaboration [116] gives the most constraining limit to date for both the linear and quadratic scenarios by searching for evidence of photon decay. However, that limit can only apply to the super-luminal regime where the photon decay process is kinematically allowed. A more direct comparison is to the limits obtained based on searches for the Bethe-Heitler cross section suppression by Rubtsov et al. [93] and Satunin [115], which use the modification of the spectral shape due to suppression of the Bethe-Heitler cross section. While our current limit is not as good as theirs, our method is a more direct measurement of the effect and does not rely on information of the intrinsic spectral shape of the source. The technique of directly measuring the Bethe-Heitler cross section is independent of astrophysical models. With additional data from future telescopes the technique presented here will enable the extraction of much more stringent limits or even the observation of LIV.

There is still a large space for improvement. The current analysis only reaches a highest energy point of 3.3 TeV; to have better constraints on the quantum energy scale a higher energy is preferred. There are several factors limiting our ability to extend the measurement to higher energy. Firstly, the constraint of the field of view of the instrument restricted the highest energy at which we can obtain reliable measurements (see Chapter 6 for the discussion of the image clipping effect). Although this constraint can be somewhat negated by observing the source at a larger zenith angle ($\theta_{ze} > 60°$), there is limited data available in that regime. Also, there is the limit due to the low statistics; although we can extend the current data set (only $\sim$ 25 hours of data used) by using data of different zenith angle bins and using data from V4 and V5 epochs, these data cannot be easily combined directly given the different resolutions and bias responses to the shower

height reconstruction. Also, using the entire data set will only provide a factor of 10 increase in statistics (we have a combined data set of $\sim$ 300 hours), which would only improve the limit by a factor of $\sim \sqrt{10} \approx 3$. So, to get a significant improvement in the limit, either we need to have significantly more observations of the Crab at larger zenith angle using VERITAS or use data from the next generation of instruments such as CTA (see Chapter 2).

Is it possible to extend the limit beyond the Planck energy scale with CTA? To answer this question, we first look at the potential limit that can be obtained with measurements at higher energies. To calculate this, we use a simple assumption that the limit is mainly affected by the highest energy point and that the uncertainty on the highest energy point is $\sim$ 10%. Then the limit that can be achieved with a point at E_{max} can be calculated as:

$$\left(\frac{|S_n(E_{max}, M_{LIV,95\%CL}) - 1.0|}{10\%}\right)^2 = 2.71 \tag{7.9}$$

Figures 7–4 and 7–5 show the potential one-sided 95% limit for a highest energy point at E_{max} for the linear and quadratic cases. In the linear scenario, a measurement of the cross section at 20 TeV with 10% uncertainty can push the limit beyond the Planck scale. Using the projected effective area of CTA (Figure 7–6) compared to VERITAS' effective area (Figure 4–17), we can see that the CTA South array has an effective area 50 times VERITAS' at 20 TeV and 20 deg zenith angle (10 times VERITAS' for the North array). We can use the statistics of our 3 TeV energy bin, which has an uncertainty of $\sim$ 10% with 81 excess events and 24 hours of observation, to estimate the amount of time needed to achieve the same level of uncertainty at 20 TeV:

$$\begin{cases} \frac{81\text{counts}}{(81\text{counts})/(24\text{ hr})\times(20\text{TeV}/3\text{TeV})^{-1.5}\times 10} \approx 41hr, \text{ North} \\ \frac{81\text{counts}}{(81\text{counts})/(24\text{ hr})\times(20\text{TeV}/3\text{TeV})^{-1.5}\times 50} \approx 8hr, \text{ South} \end{cases} \tag{7.10}$$

With the South array, a mere 8 hours of data is enough to achieve the required statistics to obtain a limit at E_p for the linear LIV scenario.

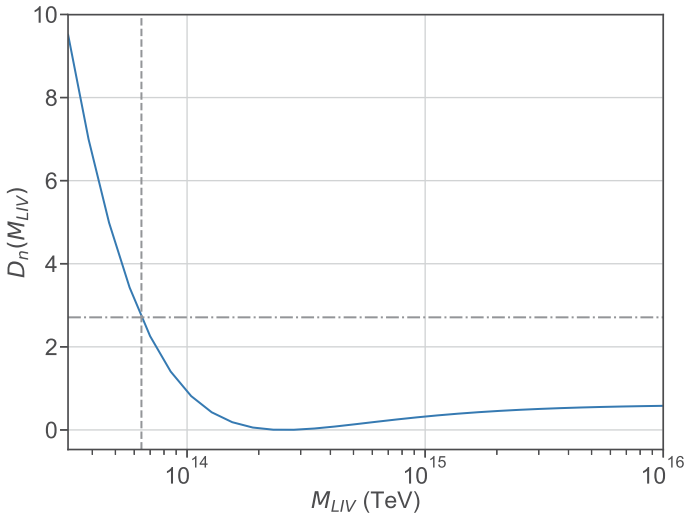

(a) Linear sub-luminal

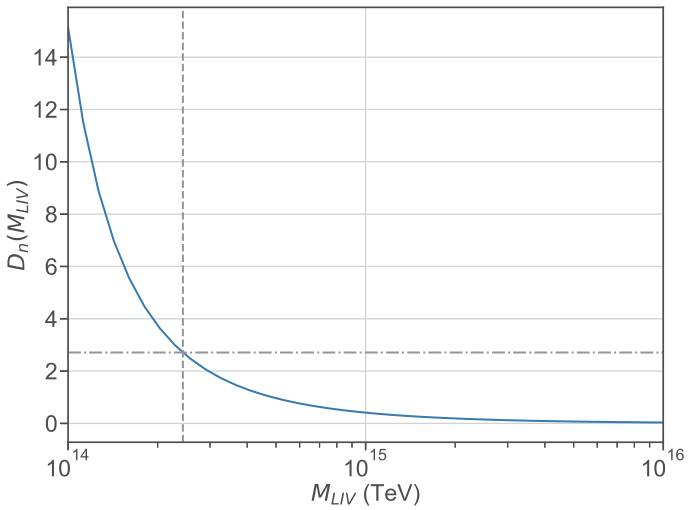

(b) Linear super-luminal

Figure 7–2: Likelihood curves for the linear LIV scenario (n=1); for sub-luminal η_γ=1 (top) and super-luminal η_γ=−1 (bottom) cases. The vertical grey dashed lines show the 95% CL limits ($D_n(M_{LIV})$= 2.71).

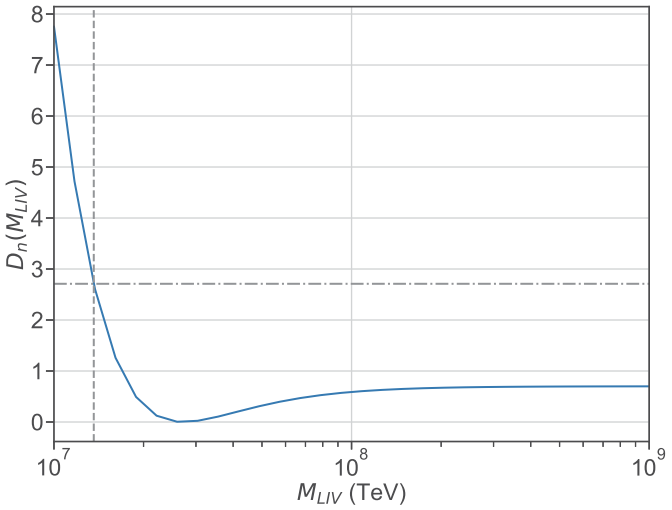

(a) Quadratic sub-luminal

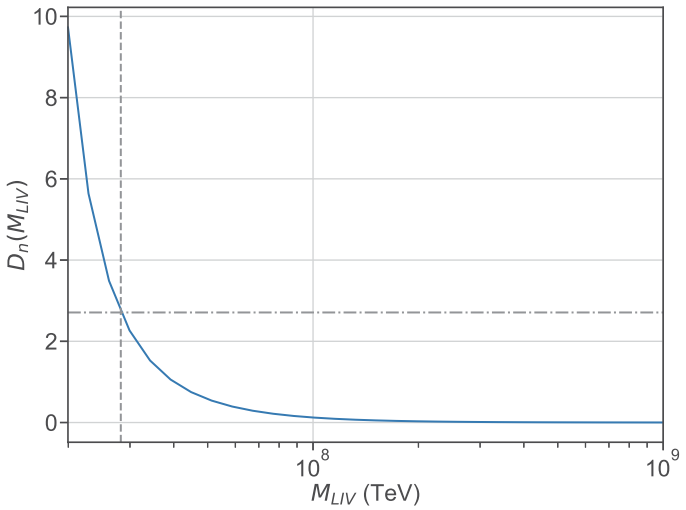

(b) Quadratic super-luminal

Figure 7–3: Likelihood curves for the quadratic LIV scenario (n=2); for sub-luminal η_γ=1 (top) and super-luminal η_γ=−1 (bottom) cases. The vertical grey dashed lines show the 95% CL limits ($D_n(M_{LIV}) = 2.71$).

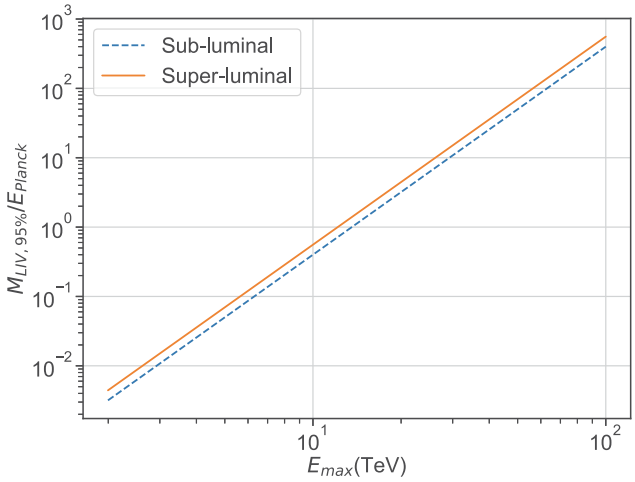

Figure 7–4: Projected limit for the linear LIV scenarios with the highest energy point at E_{max}. An uncertainty of 10% is assumed for the highest energy point.

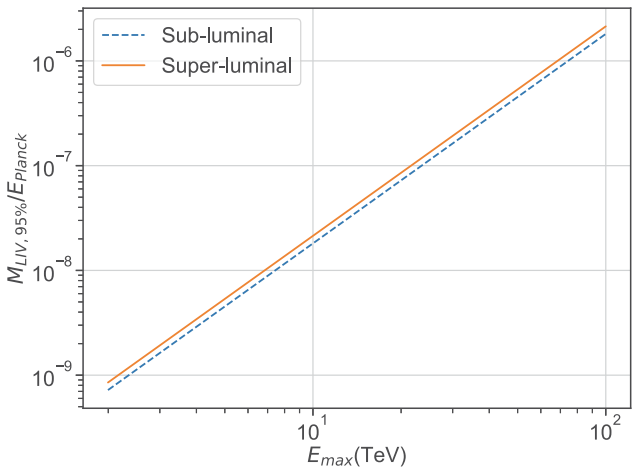

Figure 7–5: Projected limit for the quadratic LIV scenario with highest energy point at E_{max}. An uncertainty of 10% is assumed for the highest energy point.

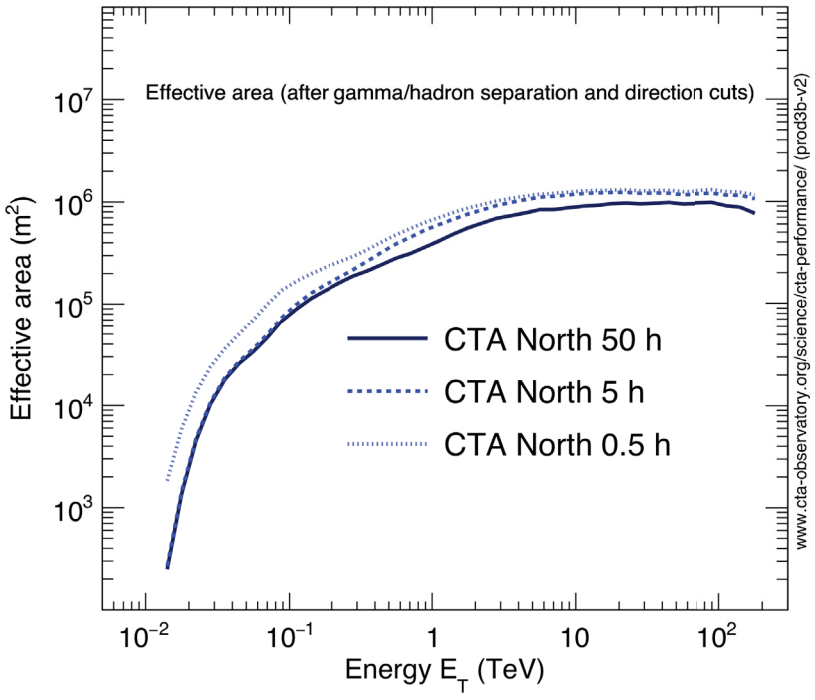

(a) North Array

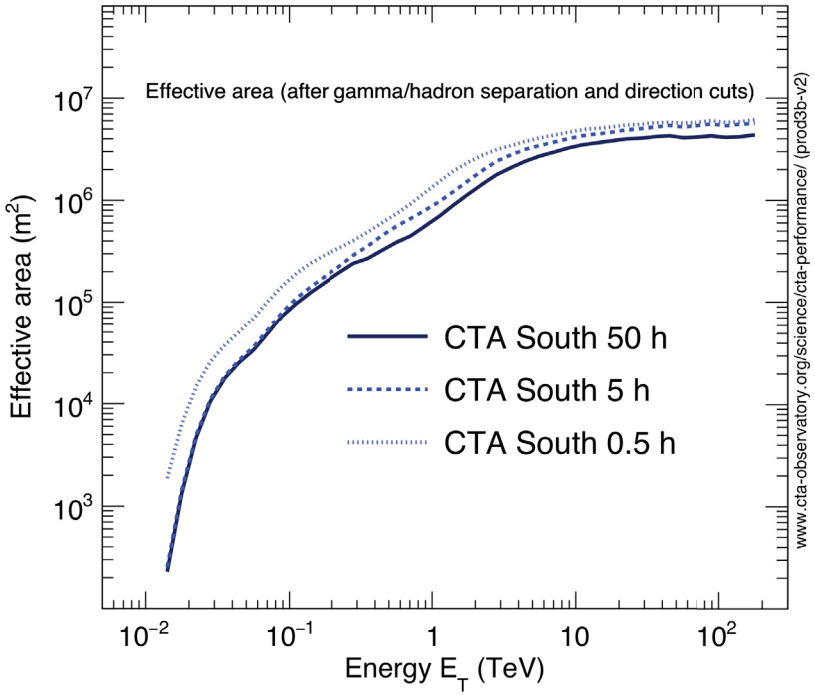

(b) South Array

Figure 7–6: Projected effective areas for the South and North arrays of CTA. The different curves represent effective areas after analysis cuts optimized for 50 hours, 5 hours and 0.5 hours of observations. Image Credit: [30].

8 Conclusions

A new method of measuring the Bethe-Heitler cross section in air has been developed using the distribution of shower maximum X_{max} from gamma-ray initiated showers using IACT data on the Crab Nebula. For this analysis, we have developed a new impact distance correction method to accurately reconstruct the height of the shower maximum X_{max} for the range of 200 g/cm^2 $< X_{max} <$ 500 g/cm^2 with a resolution of $\sim$ 40 g/cm^2.

A total of 24 hours of data observing the Crab Nebula is used and the cross sections are measured from 450 GeV to 3.33 TeV. The averaged cross section across this range is $0.55 \pm 0.02(\text{stat}) \pm 0.04(\text{sys})$ which is in good agreement with the theoretical expectation of 0.51 b. The main source of systematic uncertainties includes the uncertainty on the atmospheric model used in converting height to X_{max}, mixing of data at different zenith angles, and the inaccuracy of modelling of the responses of the height reconstruction. The overall systematic effects add up to $\sim 10\%$.

This is the highest energy measurement known to the author at the time of writing that directly measures the cross section of pair production. Using this measurement, a search for LIV effects is performed by searching for potential modifications to the Bethe-Heitler cross section due to LIV. The 95% CL limits

on the quantum energy scale (using the calculation of [90]) for the linear and quadratic cases are $\sim 10^{17}$ GeV and $\sim 10^{10}$ GeV, respectively.

Although it is not the most constraining limit to date, the limit derived through this measurement is noteworthy because it is purely based on the physical processes occurring in the atmosphere and has minimal dependency on the astrophysical process that produces the gamma rays. While we use a particular model of the LIV effect on the Bethe-Heitler cross section due to Vankov and Stanev [90], our measurement can be used directly for application to other models as well. This thesis has demonstrated a new technique to directly measure the Bethe-Heitler cross section which is independent of astronophysical models. With this, it was possible to put constraints on LIV. While our constraint is less stringent than other current limits, with additional data from future telescopes the presented technique will enable the extraction of much more stringent limits or even the observation of LIV.

A

Fit of Instrument Response Modified GMB to Data

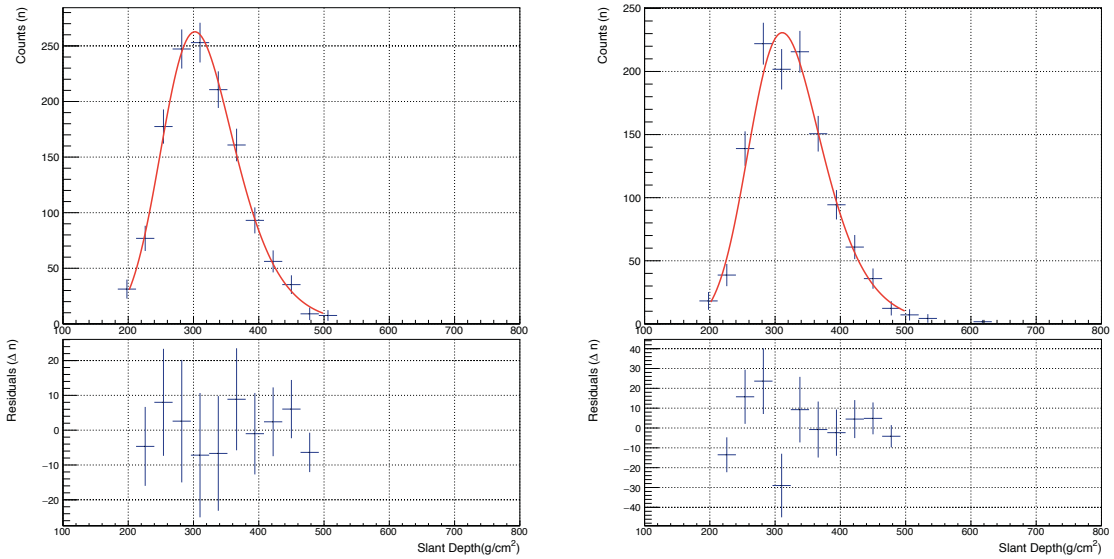

(a) 0.4 TeV $< E <$ 0.5 TeV.

(b) 0.5 TeV $< E <$ 0.6 TeV.

Figure A–1: Energy bin 0. 0.4 TeV $< E <$ 0.6 TeV.

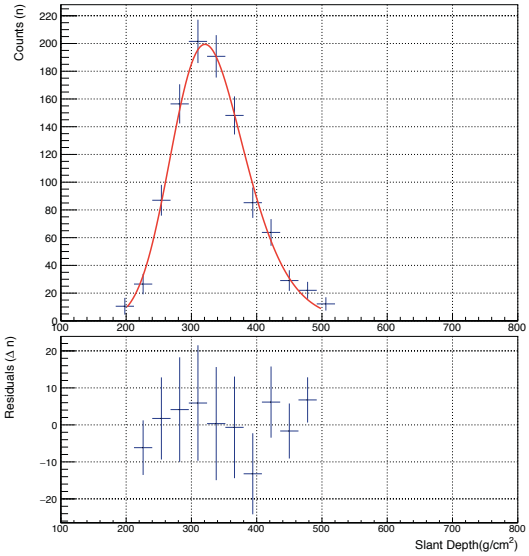

(a) 0.6 TeV $< E <$ 0.7 TeV.

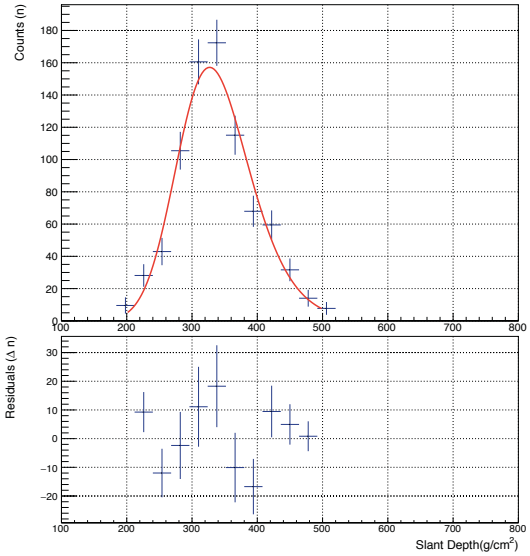

(b) 0.7 TeV $< E <$ 0.9 TeV.

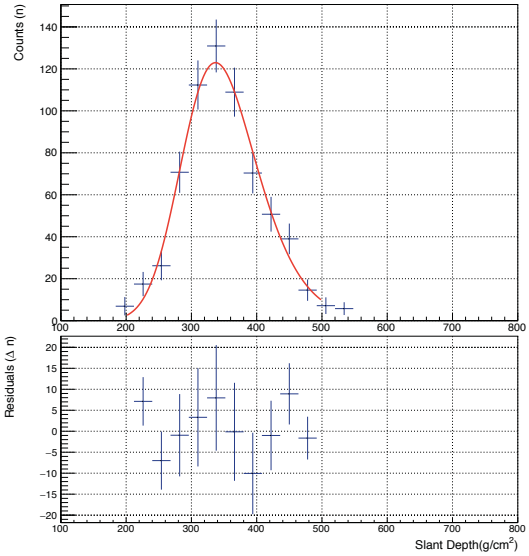

(c) 0.9 TeV $< E <$ 1.1 TeV

Figure A–2: Energy bin 1. 0.6 TeV $< E <$ 1.1 TeV.

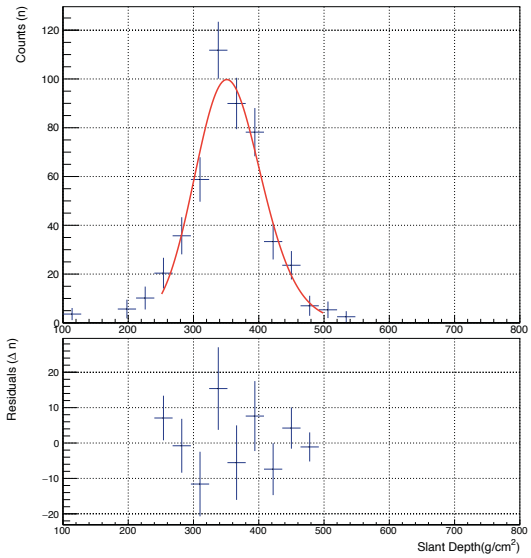

(a) 1.1 TeV $< E <$ 1.4 TeV.

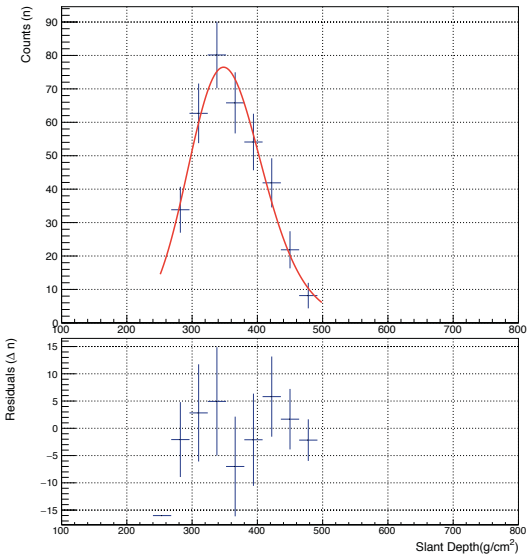

(b) 1.4 TeV $< E <$ 1.7 TeV.

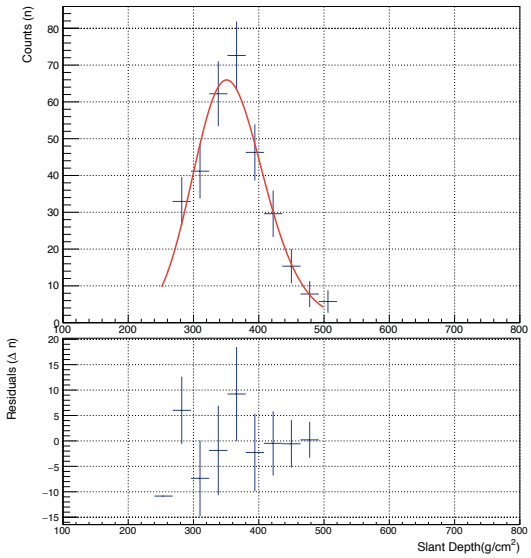

(c) 1.7 TeV $< E <$ 2.0 TeV.

Figure A–3: Energy bin 2. 1.1 TeV $< E <$ 2.0 TeV.

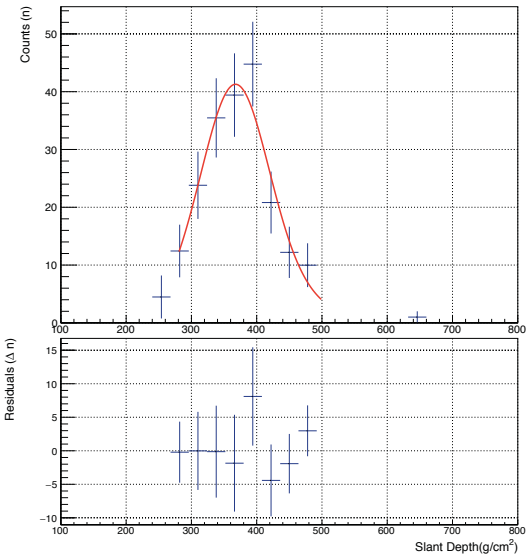

(a) 2.0 TeV $< E <$ 2.5 TeV.

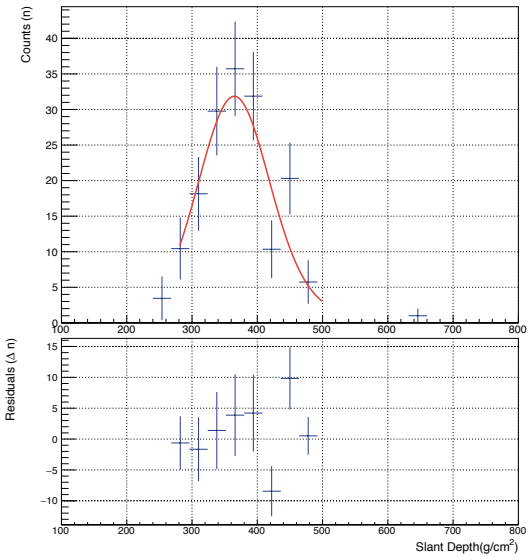

(b) 2.5 TeV $< E <$ 3.0 TeV.

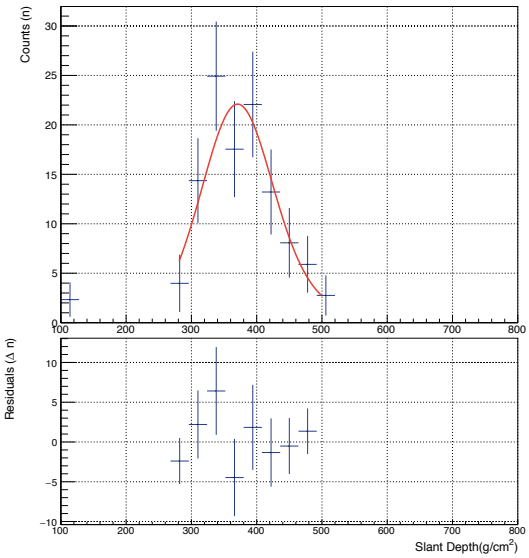

(c) 3.0 TeV $< E <$ 3.7 TeV.

Figure A–4: Energy bin 3. 2.0 TeV $< E <$ 3.7 TeV.

References

[1] C. Nigro, C. Deil, R. Zanin, et al. Towards open and reproducible multi-instrument analysis in gamma-ray astronomy. *Astronomy and Astrophysics*, 625:A10, May 2019. doi: 10.1051/0004-6361/201834938.

[2] L. Nogués, T. T. Y. Lin, C. Perennes, et al. First combined studies on Lorentz Invariance Violation from observations of astrophysical sources. In *35th International Cosmic Ray Conference (ICRC2017)*, volume 301 of *International Cosmic Ray Conference*, page 646, Jan 2017.

[3] T. C. Weekes, M. F. Cawley, D. J. Fegan, et al. Observation of TeV Gamma Rays from the Crab Nebula Using the Atmospheric Cerenkov Imaging Technique. ApJ, 342:379, Jul 1989. doi: 10.1086/167599.

[4] H. Bethe and W. Heitler. On the Stopping of fast particles and on the creation of positive electrons. *Proc. Roy. Soc. Lond.*, A146:83–112, 1934. doi: 10.1098/rspa.1934.0140.

[5] *Very High Energy Gamma-Ray Astronomy*, volume 11 of *Wiley Praxis Series in Astronomy and Astrophysics*, Apr 2003. doi: 10.1201/9781420033199.

[6] Fermi LAT Collaboration. LAT website. https://www-glast.stanford.edu/, .

[7] S Wakely and D. Horan. TeVCat. http://tevcat.uchicago.edu/. Accessed: 2019-12-15.

[8] Enrico Fermi. On the Origin of the Cosmic Radiation. *Physical Review*, 75 (8):1169–1174, Apr 1949. doi: 10.1103/PhysRev.75.1169.

[9] Malcolm S. Longair. *High Energy Astrophysics*. Cambridge University Press, 2011. ISBN 9780521756181.

[10] André Balogh and Rudolf A. Treumann. *Physics of Collisionless Shocks*, volume 12. 2013. doi: 10.1007/978-1-4614-6099-2.

[11] E. Lorenz and R. Wagner. Very-high energy gamma-ray astronomy. A 23-year success story in high-energy astroparticle physics. *European Physical Journal H*, 37(3):459–513, Aug 2012. doi: 10.1140/epjh/e2012-30016-x.

[12] O. Klein and T. Nishina. Über die Streuung von Strahlung durch freie Elektronen nach der neuen relativistischen Quantendynamik von Dirac. *Zeitschrift für Physik*, 52(11-12):853–868, Nov 1929. doi:

10.1007/BF01366453.

[13] M. Tanabashi, K. Hagiwara, K. Hikasa, et al. Review of particle physics. *Phys. Rev. D*, 98:030001, Aug 2018. doi: 10.1103/PhysRevD.98.030001.

[14] P. K.F. Grieder. *Extensive Air Showers*. Springer, 2010.

[15] Yung-Su Tsai. Pair production and Bremsstrahlung of charged leptons. *Rev. Mod. Phys.*, 46:815–851, Oct 1974. doi: 10.1103/RevModPhys.46.815.

[16] W. B. Atwood, A. A. Abdo, M. Ackermann, et al. The Large Area Telescope on the Fermi Gamma-Ray Space Telescope Mission. ApJ, 697(2):1071–1102, Jun 2009. doi: 10.1088/0004-637X/697/2/1071.

[17] W. Heitler. *Quantum theory of radiation*. Oxford University Press, third edition, 1954.

[18] Andrew McCann. *Discovery of Emission above 100 GeV from The Crab Pulsar With VERITAS*. PhD thesis, McGill University, 2011.

[19] T. C. Weekes, M. F. Cawley, D. J. Fegan, et al. Observation of TeV Gamma Rays from the Crab Nebula Using the Atmospheric Cerenkov Imaging Technique. ApJ, 342:379, Jul 1989. doi: 10.1086/167599.

[20] HESS collaboration. H.E.S.S. Website. URL `https://www.mpi-hd.mpg.de/hfm/HESS/`. Accessed: 2019-12-15.

[21] MAGIC collaboration. MAGIC Website. https://magic.mpp.mpg.de. Accessed: 2019-12-15.

[22] J. Aleksić, S. Ansoldi, L. A. Antonelli, et al. The major upgrade of the MAGIC telescopes, Part I: The hardware improvements and the commissioning of the system. *Astroparticle Physics*, 72:61–75, Jan 2016. doi: 10.1016/j.astropartphys.2015.04.004.

[23] J. Aleksić, S. Ansoldi, L. A. Antonelli, et al. The major upgrade of the MAGIC telescopes, Part II: A performance study using observations of the Crab Nebula. *Astroparticle Physics*, 72:76–94, Jan 2016. doi: 10.1016/j.astropartphys.2015.02.005.

[24] VERITAS collaboration. VERITAS website. http://veritas.sao.arizona.edu/. Accessed: 2019-12-15.

[25] FACT collaboration. FACT Website. https://www.isdc.unige.ch/fact/. Accessed: 2019-12-15.

[26] FACT Collaboration, Maximilian Nöthe, Dominik Neise, and Sebastian Achim Mueller. Towards Robotic Operation with the First G-APD Cherenkov Telescope. *arXiv e-prints*, art. arXiv:1806.01542, Jun 2018.

[27] A. U. Abeysekara, A. Albert, R. Alfaro, et al. Observation of the Crab Nebula with the HAWC Gamma-Ray Observatory. ApJ, 843(1):39, Jul 2017. doi: 10.3847/1538-4357/aa7555.

[28] R. Atkins, W. Benbow, D. Berley, et al. Milagrito, a TeV air-shower array. *Nuclear Instruments and Methods in Physics Research Section A: Accelerators, Spectrometers, Detectors and Associated Equipment*, 449(3):478 – 499, 2000. ISSN 0168-9002. doi: https://doi.org/10.1016/S0168-9002(00)00146-7. URL `http://www.sciencedirect.com/science/article/pii/S0168900200001467`.

[29] HAWC collaboration. HAWC Observatory Website. https://www.hawc-observatory.org. Accessed: 2019-12-15.
[30] CTA collaboration. CTA performance webpage. https://www.cta-observatory.org/science/cta-performance/#1472563157332-1ef9e83d-426c.
[31] Fermi LAT Collaboration. Fermi Data Access Website. https://fermi.gsfc.nasa.gov/ssc/data/access/, . Accessed: 2020-02-28.
[32] John M. Davies and Eugene S. Cotton. Design of the Quartermaster solar furnace. *Solar Energy*, 1(2-3):16 – 22, 1957. ISSN 0038-092X. doi: 10.1016/0038-092X(57)90116-0. The Proceedings of the Solar Furnace Symposium.
[33] J. Perkins, K. Harris, J. Finley, et al. Mirror Facets for the VERITAS Telescopes. In *Proceedings, 30th International Cosmic Ray Conference (ICRC 2007): Merida, Yucatan, Mexico, July 3-11, 2007*, volume 3, pages 1397–1400, 2007.
[34] Richard Clinton Fernow. *Introduction to Experimental Particle Physics*. 1989.
[35] S. Griffin for the VERITAS Collaboration. VERITAS Observations under Bright Moonlight. *ArXiv e-prints*, art. arXiv:1508.07186, August 2015.
[36] Benjamin Zitzer and VERITAS Collaboration. The VERITAS Upgraded Telescope-Level Trigger Systems: Technical Details and Performance Characterization. In *International Cosmic Ray Conference*, volume 33 of *International Cosmic Ray Conference*, page 3076, January 2013.
[37] P. Cogan. VEGAS, the VERITAS Gamma-ray Analysis Suite. In *International Cosmic Ray Conference*, volume 3 of *International Cosmic Ray Conference*, pages 1385–1388, Jan 2008.
[38] G. Maier and J. Holder. Eventdisplay: An Analysis and Reconstruction Package for Ground-based Gamma-ray Astronomy. In *35th International Cosmic Ray Conference (ICRC2017)*, volume 301 of *International Cosmic Ray Conference*, page 747, Jan 2017.
[39] E. Aliu, H. Anderhub, L. A. Antonelli, et al. Improving the performance of the single-dish Cherenkov telescope MAGIC through the use of signal timing. *Astroparticle Physics*, 30(6):293–305, Jan 2009. doi: 10.1016/j.astropartphys.2008.10.003.
[40] A. M. Hillas. Cerenkov light images of EAS produced by primary gamma. In F. C. Jones, editor, *International Cosmic Ray Conference*, volume 3 of *International Cosmic Ray Conference*, pages 445–448, August 1985.
[41] S. LeBohec, C. Duke, and P. Jordan. Minimal stereoscopic analysis for imaging atmospheric Cherenkov telescope arrays. *Astroparticle Physics*, 24 (1-2):26–31, Sep 2005. doi: 10.1016/j.astropartphys.2005.02.008.
[42] W. Hofmann, I. Jung, A. Konopelko, et al. Comparison of techniques to reconstruct VHE gamma-ray showers from multiple stereoscopic Cherenkov images. *Astroparticle Physics*, 12(3):135–143, Nov 1999. doi: 10.1016/S0927-6505(99)00084-5.
[43] M. Krause, E. Pueschel, and G. Maier. Boosted decision trees for the gamma-hadron-separation in eventdisplay. Technical report,

2015. URL https://veritas.sao.arizona.edu/wiki/images/2/2e/BDT-GammaHadron-Note.pdf.

[44] Maria Krause, Elisa Pueschel, and Gernot Maier. Improved γ/hadron separation for the detection of faint γ-ray sources using boosted decision trees. *Astroparticle Physics*, 89:1–9, Mar 2017. doi: 10.1016/j.astropartphys.2017.01.004.

[45] D. Berge, S. Funk, and J. Hinton. Background modelling in very-high-energy γ-ray astronomy. A&A, 466(3):1219–1229, May 2007. doi: 10.1051/0004-6361:20066674.

[46] T. P. Li and Y. Q. Ma. Analysis methods for results in gamma-ray astronomy. ApJ, 272:317–324, Sep 1983. doi: 10.1086/161295.

[47] M. Peresano, R. Mirzoyan, I. Vovk, et al. The Crab Nebula Spectrum at 100 TeV Measured With MAGIC Under Very Large Zenith Angles. In *36th International Cosmic Ray Conference (ICRC2019)*, volume 36 of *International Cosmic Ray Conference*, page 759, Jul 2019.

[48] J. Wochele. KASCADE website. https://web.ikp.kit.edu/KASCADE/. Accessed: 2019-12-15.

[49] D. Heck, J. Knapp, J. N. Capdevielle, G. Schatz, and T. Thouw. *CORSIKA: a Monte Carlo code to simulate extensive air showers.* 1998.

[50] GrOptics git repository. http://gtlib.gatech.edu/pub/IACT/GrOptics.git.

[51] N. Otte. CARE website. http://otte.gatech.edu/care/. Accessed: 2019-12-15.

[52] Rene Brun and Fons Rademakers. ROOT — An object oriented data analysis framework. *Nuclear Instruments and Methods in Physics Research A*, 389(1):81–86, Feb 1997. doi: 10.1016/S0168-9002(97)00048-X.

[53] J. L. Contreras, K. Satalecka, K. Bernlör, et al. Data model issues in the Cherenkov Telescope Array project. In *34th International Cosmic Ray Conference (ICRC2015)*, volume 34 of *International Cosmic Ray Conference*, page 960, Jul 2015.

[54] Tao Han and Scott Willenbrock. Scale of quantum gravity. *Physics Letters B*, 616(3-4):215–220, June 2005. doi: 10.1016/j.physletb.2005.04.040.

[55] Giovanni Amelino-Camelia. Quantum-spacetime phenomenology. *Living Reviews in Relativity*, 16(1):5, Jun 2013. ISSN 1433-8351. doi: 10.12942/lrr-2013-5.

[56] Albert Einstein. Erklärung der Perihelbewegung des Merkur aus der allgemeinen Relativitätstheorie. *Sitzungsberichte der Königlich Preußischen Akademie der Wissenschaften (Berlin)*, pages 831–839, Jan 1915.

[57] Albert Einstein. Die Feldgleichungen der Gravitation. *Sitzungsberichte der Königlich Preußischen Akademie der Wissenschaften (Berlin)*, pages 844–847, Jan 1915.

[58] F. W. Dyson, A. S. Eddington, and C. Davidson. A Determination of the Deflection of Light by the Sun's Gravitational Field, from Observations Made at the Total Eclipse of May 29, 1919. *Philosophical Transactions of the Royal Society of London Series A*, 220:291–333, Jan 1920. doi: 10.1098/rsta.1920.0009.

[59] R. A. Hulse and J. H. Taylor. A High-Sensitivity Pulsar Survey. ApJ, 191: L59, Jul 1974. doi: 10.1086/181548.

[60] R. A. Hulse and J. H. Taylor. Discovery of a pulsar in a binary system. ApJ, 195:L51–L53, Jan 1975. doi: 10.1086/181708.

[61] J. H. Taylor, L. A. Fowler, and P. M. McCulloch. Measurements of general relativistic effects in the binary pulsar PSR1913 + 16. Nature, 277(5696): 437–440, Feb 1979. doi: 10.1038/277437a0.

[62] LIGO Scientific Collaboration and Virgo Collaboration. Observation of gravitational waves from a binary black hole merger. *Phys. Rev. Lett.*, 116: 061102, Feb 2016. doi: 10.1103/PhysRevLett.116.061102.

[63] J. M. Weisberg and J. H. Taylor. The Relativistic Binary Pulsar B1913+16: Thirty Years of Observations and Analysis. In Fred A. Rasio and Ingrid H. Stairs, editors, *Binary Radio Pulsars*, volume 328 of *Astronomical Society of the Pacific Conference Series*, page 25, Jul 2005.

[64] Stephen Hawking. Gravitationally collapsed objects of very low mass. MNRAS, 152:75, Jan 1971. doi: 10.1093/mnras/152.1.75.

[65] G. Arnison, A. Astbury, B. Aubert, et al. Experimental observation of isolated large transverse energy electrons with associated missing energy at s=540 GeV. *Physics Letters B*, 122(1):103 – 116, 1983. ISSN 0370-2693. doi: https://doi.org/10.1016/0370-2693(83)91177-2.

[66] G. Arnison, A. Astbury, B. Aubert, et al. Experimental observation of lepton pairs of invariant mass around 95 gev/c2 at the cern sps collider. *Physics Letters B*, 126(5):398 – 410, 1983. ISSN 0370-2693. doi: https://doi.org/10.1016/0370-2693(83)90188-0.

[67] Atlas Collaboration. Observation of a new particle in the search for the Standard Model Higgs boson with the ATLAS detector at the LHC. *Physics Letters B*, 716(1):1–29, Sep 2012. doi: 10.1016/j.physletb.2012.08.020.

[68] CMS Collaboration. Observation of a new boson at a mass of 125 GeV with the CMS experiment at the LHC. *Physics Letters B*, 716(1):30–61, Sep 2012. doi: 10.1016/j.physletb.2012.08.021.

[69] Peter W. Higgs. Broken symmetries and the masses of gauge bosons. *Phys. Rev. Lett.*, 13:508–509, Oct 1964. doi: 10.1103/PhysRevLett.13.508.

[70] F. Englert and R. Brout. Broken symmetry and the mass of gauge vector mesons. *Phys. Rev. Lett.*, 13:321–323, Aug 1964. doi: 10.1103/PhysRevLett.13.321.

[71] Bruce T. Cleveland, Timothy Daily, Jr. Davis, Raymond, et al. Measurement of the Solar Electron Neutrino Flux with the Homestake Chlorine Detector. ApJ, 496(1):505–526, Mar 1998. doi: 10.1086/305343.

[72] Y. Fukuda, T. Hayakawa, E. Ichihara, et al. Evidence for Oscillation of Atmospheric Neutrinos. Phys. Rev. Lett., 81(8):1562–1567, Aug 1998. doi: 10.1103/PhysRevLett.81.1562.

[73] Q. R. Ahmad, R. C. Allen, T. C. Andersen, et al. Measurement of the Rate of ν_e + d –> p + p + e^- Interactions Produced by ^{8}B Solar Neutrinos at the Sudbury Neutrino Observatory. Phys. Rev. Lett., 87(7):071301, August 2001. doi: 10.1103/PhysRevLett.87.071301.

[74] B. Pontecorvo. Neutrino Experiments and the Problem of Conservation of Leptonic Charge. *Soviet Journal of Experimental and Theoretical Physics*, 26:984, May 1968.

[75] F. R. Klinkhamer. Neutrino mass and the Standard Model. *arXiv e-prints*, art. arXiv:1112.2669, December 2011.

[76] D. I. Kazakov. The Higgs boson is found: what is next? *Physics Uspekhi*, 57 (9):930-942, Sep 2014. doi: 10.3367/UFNe.0184.201409j.1004.

[77] Rodolfo Gambini and Jorge Pullin. *A first course in loop quantum gravity*. Oxford University Press, 2011. doi: 10.1093/acprof:oso/9780199590759.001.0001.

[78] B. Zwiebach. *A first course in string theory*. Cambridge University Press, 2006. ISBN 0521831431, 9780521831437, 9780511207570.

[79] D. Colladay and V. Alan Kostelecký. Lorentz-violating extension of the Standard Model. Phys. Rev. D, 58(11):116002, Dec 1998. doi: 10.1103/PhysRevD.58.116002.

[80] A. Abramowski, F. Acero, F. Aharonian, et al. Search for Lorentz Invariance breaking with a likelihood fit of the PKS 2155-304 flare data taken on MJD 53944. *Astroparticle Physics*, 34(9):738–747, Apr 2011. doi: 10.1016/j.astropartphys.2011.01.007.

[81] G. Amelino-Camelia, John Ellis, N. E. Mavromatos, D. V. Nanopoulos, and Subir Sarkar. Tests of quantum gravity from observations of γ-ray bursts. Nature, 393(6687):763–765, June 1998. doi: 10.1038/31647.

[82] Rodolfo Gambini and Jorge Pullin. Nonstandard optics from quantum space-time. Phys. Rev. D, 59(12):124021, Jun 1999. doi: 10.1103/PhysRevD.59.124021.

[83] Igor G. Mitrofanov. Astrophysics (communication arising): A constraint on canonical quantum gravity? Nature, 426(6963):139, Nov 2003. doi: 10.1038/426139a.

[84] G. Amelino-Camelia, John Ellis, N. E. Mavromatos, and D. V. Nanopoulos. Distance Measurement and Wave Dispersion in a Liouville-String Approach to Quantum Gravity. *International Journal of Modern Physics A*, 12(3):607–623, Jan 1997. doi: 10.1142/S0217751X97000566.

[85] Uri Jacob and Tsvi Piran. Lorentz-violation-induced arrival delays of cosmological particles. J. Cosmology Astropart. Phys., 2008(1):031, Jan 2008. doi: 10.1088/1475-7516/2008/01/031.

[86] Planck Collaboration, P. A. R. Ade, N. Aghanim, et al. Planck 2015 results. XIII. Cosmological parameters. A&A, 594:A13, Sep 2016. doi: 10.1051/0004-6361/201525830.

[87] J. Biteau and D. A. Williams. The Extragalactic Background Light, the Hubble Constant, and Anomalies: Conclusions from 20 Years of TeV Gamma-ray Observations. ApJ, 812(1):60, Oct 2015. doi: 10.1088/0004-637X/812/1/60.

[88] Rudy C. Gilmore, Rachel S. Somerville, Joel R. Primack, and Alberto Domínguez. Semi-analytic modelling of the extragalactic background light and consequences for extragalactic gamma-ray spectra. MNRAS, 422(4):

3189–3207, Jun 2012. doi: 10.1111/j.1365-2966.2012.20841.x.

[89] H. Martínez-Huerta and A. Pérez-Lorenzana. Restrictions from Lorentz invariance violation on cosmic ray propagation. Phys. Rev. D, 95(6):063001, Mar 2017. doi: 10.1103/PhysRevD.95.063001.

[90] H. Vankov and T. Stanev. Lorentz invariance violation and the QED formation length. *Physics Letters B*, 538(3-4):251–256, Jul 2002. doi: 10.1016/S0370-2693(02)02005-1.

[91] ML Ter-Mikaelian. The interference emission of high-energy electrons. *Zh. Eksp. Teor. Fiz*, 25:296, 1953.

[92] Spencer Klein. Suppression of bremsstrahlung and pair production due to environmental factors. *Rev. Mod. Phys.*, 71:1501–1538, Oct 1999. doi: 10.1103/RevModPhys.71.1501.

[93] Grigory Rubtsov, Petr Satunin, and Sergey Sibiryakov. Constraints on violation of lorentz invariance from atmospheric showers initiated by multi-TeV photons. *Journal of Cosmology and Astroparticle Physics*, 2017(05): 049–049, may 2017. doi: 10.1088/1475-7516/2017/05/049.

[94] Ray W. Klebesadel, Ian B. Strong, and Roy A. Olson. Observations of Gamma-Ray Bursts of Cosmic Origin. ApJ, 182:L85, Jun 1973. doi: 10.1086/181225.

[95] C. A. Meegan, G. J. Fishman, R. B. Wilson, et al. Spatial distribution of γ-ray bursts observed by BATSE. Nature, 355(6356):143–145, Jan 1992. doi: 10.1038/355143a0.

[96] V. A. Acciari, S. Ansoldi, L. A. Antonelli, et al. Teraelectronvolt emission from the γ-ray burst GRB 190114C. Nature, 575(7783):455–458, 2019. doi: 10.1038/s41586-019-1750-x.

[97] M. de Naurois. GRB190829A: Detection of VHE gamma-ray emission with H.E.S.S. *The Astronomer's Telegram*, 13052:1, Aug 2019.

[98] H. Abdalla, R. Adam, F. Aharonian, et al. A very-high-energy component deep in the γ-ray burst afterglow. Nature, 575(7783):464–467, 2019. doi: 10.1038/s41586-019-1743-9.

[99] M. Ackermann, K. Asano, W. B. Atwood, et al. FERMI observations of GRB 090510: A short-hard gamma-ray burst with an additional, hard power-law component from 10 keV to GeV energies. *The Astrophysical Journal*, 716 (2):1178–1190, May 2010. doi: 10.1088/0004-637x/716/2/1178.

[100] Robert Antonucci. Unified models for active galactic nuclei and quasars. ARA&A, 31:473–521, Jan 1993. doi: 10.1146/annurev.aa.31.090193.002353.

[101] C. Megan Urry and Paolo Padovani. Unified Schemes for Radio-Loud Active Galactic Nuclei. PASP, 107:803, Sep 1995. doi: 10.1086/133630.

[102] V. Beckmann and C. Shrader. The AGN phenomenon: open issues. In *Proceedings of "An INTEGRAL view of the high-energy sky (the first 10 years)" - 9th INTEGRAL Workshop and celebration of the 10th anniversary of the launch (INTEGRAL 2012). 15-19 October 2012. Bibliotheque Nationale de France*, page 69, Jan 2012.

[103] A. Hewish, S. J. Bell, J. D. H. Pilkington, P. F. Scott, and R. A. Collins. Observation of a rapidly pulsating radio source. Nature, 217(5130):709–713,

1968. doi: 10.1038/217709a0.

[104] VERITAS Collaboration, E. Aliu, T. Arlen, et al. Detection of Pulsed Gamma Rays Above 100 GeV from the Crab Pulsar. *Science*, 334(6052):69, Oct 2011. doi: 10.1126/science.1208192.

[105] Nathan Smith. The Crab nebula and the class of Type IIn-P supernovae caused by sub-energetic electron-capture explosions. MNRAS, 434(1): 102–113, September 2013. doi: 10.1093/mnras/stt1004.

[106] A. U. Abeysekara, A. Albert, R. Alfaro, et al. Measurement of the Crab Nebula Spectrum Past 100 TeV with HAWC. ApJ, 881(2):134, Aug 2019. doi: 10.3847/1538-4357/ab2f7d.

[107] H. Abdalla, F. Aharonian, F. Ait Benkhali, et al. The 2014 TeV γ-Ray Flare of Mrk 501 Seen with H.E.S.S.: Temporal and Spectral Constraints on Lorentz Invariance Violation. ApJ, 870(2):93, Jan 2019. doi: 10.3847/1538-4357/aaf1c4.

[108] Rodrigo Guedes Lang, Humberto Martínez-Huerta, and Vitor de Souza. Improved limits on Lorentz invariance violation from astrophysical gamma-ray sources. Phys. Rev. D, 99(4):043015, Feb 2019. doi: 10.1103/PhysRevD.99.043015.

[109] V. Vasileiou, A. Jacholkowska, F. Piron, et al. Constraints on Lorentz invariance violation from Fermi-Large Area Telescope observations of gamma-ray bursts. Phys. Rev. D, 87(12):122001, Jun 2013. doi: 10.1103/PhysRevD.87.122001.

[110] Manel Martínez and Manel Errando. A new approach to study energy-dependent arrival delays on photons from astrophysical sources. *Astroparticle Physics*, 31(3):226–232, Apr 2009. doi: 10.1016/j.astropartphys.2009.01.005.

[111] A. Abramowski, F. Aharonian, F. Ait Benkhali, et al. The 2012 Flare of PG 1553+113 Seen with H.E.S.S. and Fermi-LAT. ApJ, 802(1):65, Mar 2015. doi: 10.1088/0004-637X/802/1/65.

[112] M. L. Ahnen, S. Ansoldi, L. A. Antonelli, et al. Constraining Lorentz Invariance Violation Using the Crab Pulsar Emission Observed up to TeV Energies by MAGIC. ApJS, 232(1):9, Sep 2017. doi: 10.3847/1538-4365/aa8404.

[113] B. Zitzer and VERITAS Collaboration. Lorentz Invariance Violation Limits from the Crab Pulsar using VERITAS. *arXiv e-prints*, art. arXiv:1307.8382, Jul 2013.

[114] M. Chrétien. *Detection of Pulsed Gamma Rays Above 100 GeV from the Crab Pulsar*. PhD thesis, Université Pierre et Marie Curie, 2015.

[115] Petr Satunin. New constraints on Lorentz Invariance violation from Crab Nebula spectrum beyond 100 TeV. *arXiv e-prints*, art. arXiv:1906.08221, Jun 2019.

[116] HAWC Collaboration, A. Albert, R. Alfaro, et al. Constraints on Lorentz invariance violation from HAWC observations of gamma rays above 100 TeV. *arXiv e-prints*, art. arXiv:1911.08070, Nov 2019.

[117] A. Aab, P. Abreu, M. Aglietta, et al. Depth of maximum of air-shower profiles at the pierre auger observatory. i. measurements at energies above

$10^{17.8}$ eV. *Phys. Rev. D*, 90:122005, Dec 2014. doi: 10.1103/PhysRevD.90.122005.

[118] R. U. Abbasi, M. Abe, T. Abu-Zayyad, et al. Measurement of the proton-air cross section with telescope array's middle drum detector and surface array in hybrid mode. *Phys. Rev. D*, 92:032007, Aug 2015. doi: 10.1103/PhysRevD.92.032007.

[119] Luan B. Arbeletche and Vitor de Souza. On the parametrization of the distributions of depth of shower maximum of ultra-high energy extensive air showers. *Astroparticle Physics*, 116:102389, 2020. ISSN 0927-6505. doi: https://doi.org/10.1016/j.astropartphys.2019.102389.

[120] Eric Bertin. Global fluctuations and gumbel statistics. *Phys. Rev. Lett.*, 95: 170601, Oct 2005. doi: 10.1103/PhysRevLett.95.170601.

[121] Manlio De Domenico, Mariangela Settimo, Simone Riggi, and Eric Bertin. Reinterpreting the development of extensive air showers initiated by nuclei and photons. *Journal of Cosmology and Astroparticle Physics*, 2013(07): 050–050, Jul 2013. doi: 10.1088/1475-7516/2013/07/050.

[122] T. Antal, M. Droz, G. Györgyi, and Z. Rácz. $1/f$ noise and extreme value statistics. *Phys. Rev. Lett.*, 87:240601, Nov 2001. doi: 10.1103/PhysRevLett.87.240601.

[123] A M Hillas. The sensitivity of Cerenkov radiation pulses to the longitudinal development of cosmic-ray showers. *Journal of Physics G: Nuclear Physics*, 8 (10):1475–1492, oct 1982. doi: 10.1088/0305-4616/8/10/017.

[124] T. K. Gaisser and A. M. Hillas. Reliability of the Method of Constant Intensity Cuts for Reconstructing the Average Development of Vertical Showers. *International Cosmic Ray Conference*, 8:353, Jan 1977.

[125] W.R. Nelson, H. Hirayama, and D.W.O. Rogers. Egs4 code system. Technical report, Stanford Linear Accelerator Center, 12 1985. URL `https://www.osti.gov/biblio/6137659-egs4-code-system`.

[126] G. D. Lafferty and T. R. Wyatt. Where to stick your data points: The treatment of measurements within wide bins. *Nuclear Instruments and Methods in Physics Research A*, 355(2):541–547, Feb 1995. doi: 10.1016/0168-9002(94)01112-5.

[127] S. A. Murphy and A. W. Van Der Vaart. On profile likelihood. *Journal of the American Statistical Association*, 95(450):449–465, 2000. doi: 10.1080/01621459.2000.10474219.

[128] iminuit team. iminuit – a python interface to minuit. `https://github.com/scikit-hep/iminuit`. Accessed: 2019-11-19.

[129] F. James and M. Roos. Minuit – a system for function minimization and analysis of the parameter errors and correlations. *Computer Physics Communications*, 10:343–367, December 1975. doi: 10.1016/0010-4655(75)90039-9.

[130] Perennes Cédric, Sol Hélène, and Bolmont Julien. Modeling spectral lags in active galactic nucleus flares in the context of Lorentz invariance violation searches. *arXiv e-prints*, art. arXiv:1911.10377, Nov 2019.

Acronyms

AGN Active Galactic Nuclei. 6

BDT Boosted Decision Tree. 55

CFD Constant Fraction Discriminators. 30
CMB Cosmic Microwave Background. 7
CTA Cherenkov Telescope Array. 17

DC Davies-Cotton. 25

EA Effective Area. 63
EBL Extra -galactic Background Light. 92
EFT Effective Field Theory. 86
EMG Exponentially Modified Gaussian. 113

FADC Flash Analog-to-Digital-Converter. 29
FIR Far Infrared Radiometers. 33
FoV Field of View. 60, 61

GMB Generalized Gumbel Distribution. 114
GRB Gamma-Ray Burst. 100

H.E.S.S High Energy Stereoscopic System. 17
HAWC High Altitude Water Cherenkov Experiment. 13, 20

IACT Imaging Air Cherenkov Telescope. 4, 15

LAT Large Area Telescope. 4, 10
LIV Lorentz Invariance Violation. 1, 81, 151
LQG Loop Quantum Gravity. 87
LUT Look Up Table. 63

MAGIC Major Atmospheric Gamma Imaging Cherenkov Telescopes. 18

MSCL Mean Reduced Scaled Length. 54
MSCW Mean Reduced Scaled Width. 54
MSL Mean Scaled Length. 54
MSW Mean Scaled Width. 54

NSB Night Sky Background. 30

OSS Optical Support Structure. 25

PMT Photo Multiplier Tube. 28

QED Quantum Electrodynamics. 94
QFT Quantum Field Theory. 84
QG Quantum Gravity. 81

SME Standard Model Extension. 88
SNO Sudbury Neutrino Observatory. 85
SSC Synchrotron Self-Compton. 8
ST String Theory. 87

UHECR Ultra High Energy Cosmic Ray. 113

VERITAS Very Energetic Radiation Imaging Telescope Array System. 24
VHE Very High Energy. 4